Hyperspectral confocal imaging of whispering-gallery-mode microlasers for bio- and ecophotonic applications [Redacted version]

Vera Marie Titze

A thesis submitted for the degree of PhD
at the
University of St Andrews

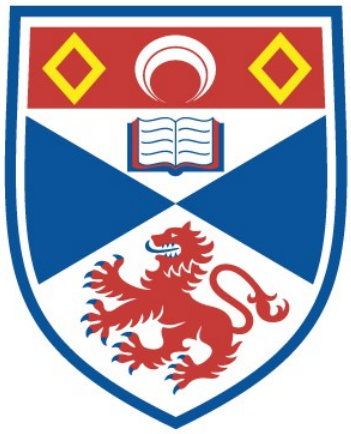

2024

Abstract

Microscopic lasers are an emerging platform for biophotonic applications. These lasers are free-standing particles with diameters of hundreds of nanometres to a few micrometres. They generate coherent emission characterised by bright and narrow lasing peaks at unique spectral positions. Particularly in the field of cell biology, such microlasers are an attractive tool for a range of applications, owing to their straightforward integration into living cells. Intracellular microlasers are optically excited and their distinct lasing spectra are recorded using custom spectral imaging systems. These spectra can serve as barcodes for tracking applications, and they can be used as intracellular sensors due to the dependence of the lasing spectra on the optical properties of their immediate environment.

Here, a custom imaging system for high-throughput microlaser readout was developed to allow capitalising on the great potential of microlasers for high-throughput measurements with single-cell specificity. This hyperspectral confocal microscope allows automated high-speed 3D-scanning of large volumes, recording a high-resolution spectrum at each voxel. The setup is predominantly used to record spectra from polystyrene microbead lasers and semiconductor nanodisk lasers. The semiconductor materials forming the nanodisk lasers were also improved for integration with the high-throughput microscope and for deep-tissue applications.

Following these advances, applications of bio-integrated microlasers were extended to larger and more complex systems, including 3D cell culture models and small animals. Due to the high-speed and high-resolution readout, this has allowed dynamic sensing with multiple microlasers in parallel, which was used for contractility sensing in a cardiac cell culture model. The spectral shifts of the measured lasing peaks were used for quantitative measurements of the local refractive index by developing and employing appropriate mathematical models. Further, the tracking capabilities were demonstrated in a 3D epidermis model, where the cellular migration was followed, and in small marine animals.

Candidate's declaration

I, Vera Marie Titze, do hereby certify that this thesis, submitted for the degree of PhD, which is approximately 33,000 words in length, has been written by me, and that it is the record of work carried out by me, or principally by myself in collaboration with others as acknowledged, and that it has not been submitted in any previous application for any degree. I confirm that any appendices included in my thesis contain only material permitted by the 'Assessment of Postgraduate Research Students' policy.

I was admitted as a research student at the University of St Andrews in August 2019.

I received funding from an organisation or institution and have acknowledged the funder(s) in the full text of my thesis.

03.05.2024
Date Signature of candidate

Supervisor's declaration

I hereby certify that the candidate has fulfilled the conditions of the Resolution and Regulations appropriate for the degree of PhD in the University of St Andrews and that the candidate is qualified to submit this thesis in application for that degree. I confirm that any appendices included in the thesis contain only material permitted by the 'Assessment of Postgraduate Research Students' policy.

03.05.2024
Date Signature of supervisor

Permission for publication

In submitting this thesis to the University of St Andrews we understand that we are giving permission for it to be made available for use in accordance with the regulations of the University Library for the time being in force, subject to any copyright vested in the work not being affected thereby. We also understand, unless exempt by an award of an embargo as requested below, that the title and the abstract will be published, and that a copy of the work may be made and supplied to any bona fide library or research worker, that this thesis will be electronically accessible for personal or research use and that the library has the right to migrate this thesis into new electronic forms as required to ensure continued access to the thesis.

I, Vera Marie Titze, confirm that my thesis does not contain any third-party material that requires copyright clearance.

The following is an agreed request by candidate and supervisor regarding the publication of this thesis:

Printed copy

No embargo on print copy.

Electronic copy

Embargo on part (Chapter 5 (High-Throughput applications of bio-integrated microlasers) and any parts in the Abstract, Chapter 1 (Introduction) and Chapter 6 (Outlook) that refer to content presented in Chapter 5 in detail.) of electronic copy for a period of 2 years on the following ground(s):

- Publication would preclude future publication

Supporting statement for electronic embargo request

Two projects presented in Chapter 5 are ongoing projects in our group, and the results presented in the thesis will not be published in the near future. This partial embargo was discussed with my supervisors.

Title and Abstract

- I require an embargo on the abstract only.

03.05.2024
Date Signature of candidate

03.05.2024
Date Signature of supervisor

Underpinning Research Data or Digital Outputs

Candidate's declaration

I, Vera Marie Titze, understand that by declaring that I have original research data or digital outputs, I should make every effort in meeting the University's and research funders' requirements on the deposit and sharing of research data or research digital outputs.

03.05.2024
Date Signature of candidate

Permission for publication of underpinning research data or digital outputs

We understand that for any original research data or digital outputs which are deposited, we are giving permission for them to be made available for use in accordance with the requirements of the University and research funders, for the time being in force.

We also understand that the title and the description will be published, and that the underpinning research data or digital outputs will be electronically accessible for use in accordance with the license specified at the point of deposit, unless exempt by award of an embargo as requested below.

The following is an agreed request by candidate and supervisor regarding the publication of underpinning research data or digital outputs:

Embargo on all of electronic files for a period of 2 years on the following ground(s):

- Publication would preclude future publication

Supporting statement for embargo request

The data sets used for the thesis will be used in upcoming publications in our group and we therefore would like to ask for an embargo.

03.05.2024
Date Signature of candidate

03.05.2024
Date Signature of supervisor

Acknowledgements

General Acknowledgements

I first would like to thank my supervisors for their help and support over the years. Malte, you did not only trust in me and my abilities, but also reminded me to trust myself and know the worth of my work. You often encouraged me to keep my goals and aspirations high, and helped me to get there, not only by your diligent feedback that always improved the quality of my work (including the present one). Marcel, I would like to thank you for your warm and empathetic style of supervising me, for your patience and persistence during our scientific discussions, and also for helping me to find resources or solutions I might have otherwise overlooked. I am very grateful to both of my supervisors for giving me freedom and flexibility to shape the project and the opportunity to develop my own ideas. I would also like to thank Soraya for being a colleague, mentor, and friend to me. I learned so much from you, ranging from how to make nanolasers to how to navigate academia as a young woman. Thank you for all the time you made for me, and for your drive to not be satisfied before you answered the question.

I am also very grateful to my family and friends – without you, the past four years would have been much less fun. Mama, thank you for your love and support, which I knew I could count on no matter what. No one knows me like you do, and talking to you always cheers me up and helps to put things into perspective. I also want to thank my dad. Your willingness to stand up for what you believe in even when it is uncomfortable or difficult is an inspiration for me. I am also very grateful for my best friends Sabi, Toni, and Nina. You guys never fail to make me laugh, even about things that are not funny at all, and since 2015, you are the reason I take at least one nice summer holiday per year.

I would like to thank our collaborators on various projects: Thanks to Matthias for introducing me to keratinocytes, to Jessi for all your help with everything that lives under water, and thanks to Michael, Swathi, and Cesar for their input on preliminary experiments.

Lastly, of course a huge thank you to all the other colleagues and friends I had the pleasure to work with during my PhD: Ross (who I would like to acknowledge for coining the term ‘spectrolley’), Matthias and Nachiket (who were part of some of the most interesting

biological experiments of my PhD), Elena, Alasdair, Sabina, Joe, Andrew Mo, Franciso, Andreas, Jon, Seonil, Nils K, Yali, Andrew Me, San, Chang-Ki, Julian, Florian, David, Melisa, Julia, Yingyu, Anna, Franzi, Nils S, Cat, Andi, Dziugas, Vicky, Manuel, Zahra (also for all your help with the aquaculture!) and many others both at the University of St Andrews and at the Humboldt Centre for Nano- and Biophotonics.

Funding

This work was supported by the Leverhulme Trust [RPG-2017-231].

Research Data/Digital Outputs access statement

Research data underpinning this thesis is available at doi.org/10.17630/d616d824-d195-4a36-bf62-3be19cc26352.

Publications

Peer reviewed journal publications

[1] Titze, V. M., Caixeiro, S., Di Falco, A., Schubert, M. & Gather, M. C. Red-Shifted Excitation and Two-Photon Pumping of Biointegrated GaInP/AlGaInP Quantum Well Microlasers. *ACS Photonics* **9**, 952–960 (2022).

[2] Titze, V. M. et al. Hyperspectral Confocal Imaging for High-Throughput Readout and Analysis of Bio-Integrated Microlasers. *Nature Protocols* **19**, 928–959 (2024).

Software

[3] Titze, V. M., Caixeiro, S., Schubert, M. & Gather, M. C. GatherLab/sphyncs 2023

Contents

List of Figures

1 Introduction

Micro- and nanolasers are free standing microscopic particles that can be optically pumped to emit coherent light. One of the areas of application of these lasers is in the field of biophotonics. These approaches are based on demonstrations of integrating microlasers into living cells[4–6]. The bright and narrow emission peaks, which their spectra are characterised by, contain a high information density, which makes them attractive for various applications. This includes tracking very large numbers of cells in parallel[4, 7, 8], using the unique lasing spectra as optical barcodes, and intracellular sensing[9–11], owing to the sensitivity of the lasing modes to the local refractive index around the microlaser[12, 13]. Examples include the tracking of cellular migration in a tumour spheroid[7], and the sensing of contractility in cardiomyocytes[9]. These applications further benefit from the high signal-to-noise ratio of the bright lasing emission, improved photostability compared to e.g. fluorescent labels, and the invariance of the spectral label to absorption and scattering in tissue. With this, microlasers are ideally suited for deep-tissue applications.

A fundamental understanding of the properties of the lasing emission is crucial for most applications, which is therefore discussed in Chapter 2.1. Here, the three main constituents of microscopic lasers are introduced: The gain material, the cavity for optical feedback, and the optical pumping. The two gain materials used in this work are fluorescent dyes and semiconductor quantum wells, which are discussed in more detail. These gain materials are contained in a Whispering-Gallery-Mode (WGM) microcavity, where light is confined along the resonator surface by total internal reflection, constructively interfering at discrete resonance frequencies following a circular path. WGM resonators can have spherical geometry, like microbeads[5, 9, 14] and droplets[15, 16], or cylindrical symmetry, like disks[7, 17, 18], toroids[13], or polygons[19, 20]. Other types of cavities used for micro- and nanolasers include Fabry-Perot resonators[8, 21–24] and spherical Bragg cavities[25, 26]. The position of the resonances of the microcavities, which is of fundamental importance for all applications, can be described by mathematical and numerical models that are explained here for the case of WGM resonators. Lastly, microscopic lasers are then optically pumped by pulsed laser light, and their emission is collected using a high-resolution spectrometer. This often relies on custom imaging setups; and the development and optimisation of such a system is a substantial part of the present work. To provide

the relevant background, fundamentals of microscopy and spectroscopy are discussed in Chapter 2.2, with particular emphasis on hyperspectral confocal microscopy[2, 7], where a 3D volume is raster-scanned and at each voxel, a high-resolution spectrum is recorded. Due to the interest in biological applications, implications and challenges of imaging in tissue are mentioned, where a closer look at the optical properties of tissue provides context of how nanolasers can be used and optimised to overcome these challenges[1]. The last section of the theory chapter then pertains to the specific case of imaging micro- and nanolasers, which includes the effect of their nonlinear emission characteristics on the imaging performance[27], and reviews existing methods of imaging microlasers.

Chapter 3 summarises the application-oriented optimisation of the semiconductor material of nanodisk lasers[1]. For deep-tissue, high-throughput biological applications, two aspects of the optical properties of the nanolasers were sought to be improved, whilst ensuring biocompatibility by using non-toxic alloys. Firstly, both excitation and emission of nanolasers in the so-called therapeutic windows of tissue transparency could be realised, allowing full operation of nanolasers in wavelength windows with less absorption and scattering. Secondly, compatibility with available high-repetition rate pump lasers was ensured for convenient integration of nanodisk lasers with high-speed hyperspectral imaging. This was achieved through strategic adjustments to the composition of the AlGaInP quantum well layers, which compromise the gain region of the disk lasers (Chapter 3.1), and through the demonstration of two-photon excitation of nanodisk lasers (Chapter 3.2), paving the way for deep tissue applications and integration with commercial multi-photon microscopes.

The development of imaging modalities for micro- and nanolaser readout is the focus of Chapter 4. Following a brief introduction of the motivation for high-throughput readout of microscopic lasers, the implementation of hyperspectral confocal microscopy (CHSI) for microlaser readout is discussed. In CHSI, the readout of high-resolution spectra on a high-speed line-scan camera is synchronised to confocal raster scanning[27]. This method was chosen as the most straightforward and reliable option for high-throughput spectral readout, but previous demonstrations of CHSI were limited in speed to an acquisition rate of 10 kHz/spectrum, which refers to the rate of dwelling on a confocal voxel while acquiring a single high-resolution spectrum. This corresponded to 47 min for a single $z-$stack[7], which limits the applicability of this technology to dynamically changing systems. Here, the custom-built CHSI setup achieves 58 s per volume by using flexible free-space optics and by improving the spectral acquisition speed to 125 kHz (Chapter 4.1, [2]). CHSI was also integrated with a commercial confocal microscope and with a commercial multi-

photon microscope, following the demonstration of multi-photon excitation in Chapter 3, thereby enabling convenient multi-modal acquisition of regular confocal fluorescence images and hyperspectral scans (Chapter 4.2).

Following the technological advances outlined in Chapters 3 and 4, applications of increasing complexity and previously unattainable scales were demonstrated. It was first shown that refractive index measurements can be significantly scaled up to allow 3D high-speed sensing with 115 microlasers in parallel. Here, refractive index changes induced by the diffusion of glucose solution through a volume of PS microbead lasers embedded in agarose were monitored (Chapter 5.1). The high-speed sensing capabilities then were used for 2D sensing of cardiac contractility (Chapter redacted). Finally, two applications of tagging and tracking were realised. In one experiment, individual keratinocytes were labelled with nanolasers and their migration was tracked for three days during the formation of a 3D epidermis model (Chapter 5.3). The second study is redacted in the present version.

In summary, optimisations of nanolaser materials, and the development of a custom CHSI readout setup, have enabled to capitalise on the potential of micro- and nanolasers in applications requiring large-scale labelling capabilities or parallelisation of high-resolution refractive index sensing. This is of particular interest in larger and more complex biological systems such as 3D cell culture models and small animals, where the resilience of the microlaser signal to absorption and scattering losses and the penetration depth of multi-photon excitation prove highly advantageous for these deep-tissue applications.

2 Theory

2.1 Laser physics

Owing to the central role of micro- and nanolasers in this work, the fundamental physics of lasers will first be reviewed here. Lasers are devices emitting light that is characterised by monochromaticity, coherence, and directionality, and consequently, high brightness. These properties have led to the wide use of lasers in fields ranging from biomedicine to micromachining. A laser generally consists of three elements: i) An active material, or gain material, ii) a resonator providing optical feedback, and iii) a pump source adding energy to the system. The function and mechanism of each of these three components will be discussed in the following sections, both in general, and specifically for the microscopic lasers used in this work. The theoretical aspects governing the optical properties of these micro- and nanolasers also provide the foundation for their use in practical applications. Lastly, the characteristics of the lasing process and of the resulting emission will be revisited, and it will be discussed how these properties affect microscopic imaging of micro- and nanolasers.

2.1.1 Light-matter interaction in gain materials

Lasing is a result of stimulated emission, a process by which an atom decays radiatively from a higher to a lower energy level after being stimulated by an incoming photon. A consequence of this process is that the two photons have the same phase, direction, and energy, which gives laser light its characteristic properties. Therefore, this amplifies the incoming photon, given that the energy levels of the laser's material can provide the necessary gain. To understand what requirements this imposes on the gain material, it is a good starting point to look at the possible transitions between two energy levels E_1 and E_2, with corresponding populations N_1 and N_2[28]. An atom can be raised from E_1 to E_2 through an absorption process, and it can either decay non-radiatively, or radiatively through spontaneous or stimulated emission. For now, the discussion will be limited to how the processes of absorption and stimulated emission will affect the population of the

two energy levels. The change in population N1 through absorption is described as

$$\frac{dN_1}{dt} = -\sigma_{12} F N_1, \tag{2.1}$$

where σ_{12} is the absorption cross section and F the photon flux. Similarly, the population N_2 changes through stimulated emission as

$$\frac{dN_2}{dt} = -\sigma_{21} F N_2 \tag{2.2}$$

with the stimulated emission cross section σ_{21}. To understand whether a material is amplifying light, i.e. emitting more photons than it absorbs, we can look at how the photon flux changes along elemental length dz of the material with cross-section S. The total change of photon flux in this cross section, SdF, has contributions from both absorption and emission and can therefore be computed by combining equations 2.1 and 2.2:

$$SdF = (\sigma_{21} F N_2 - \sigma_{12} F N_1) dz = \sigma_{21} F (N_2 - \frac{g_2}{g_1} N_1) dz, \tag{2.3}$$

where in the second step, Equation 2.4 was substituted, which describes Einstein's relation of stimulated emission and absorption cross section for the two energy levels of degeneracies g_1 and g_2:

$$g_2 \sigma_{21} = g_1 \sigma_{12}. \tag{2.4}$$

We achieve amplification when $dF > 0$, which follows from Equation 2.3:

$$N_2 > \frac{g_2}{g_1} N_1. \tag{2.5}$$

Equation 2.5 postulates the fundamental requirement for the lasing process widely referred to as *population inversion*, meaning that the population in the higher energy level exceeds that of the lower energy level. In such a material, the emission process dominates and it is therefore termed active material, or gain material, with the gain defined as the change of power in the material per unit length[29]

$$g = \frac{\Delta P}{P \Delta x}. \tag{2.6}$$

The gain coefficient g, expressed in units of $length^{-1}$ is therefore an important measure to explore the potential of a material for light amplification, and is a function of wavelength indicating the range over which a material is capable of amplifying photons.

In the above discussion, the role of spontaneous emission has been neglected. The population of the higher energy level N_2 changes due to spontaneous emission as

$$\frac{dN_2}{dt} = -\frac{N_2}{\tau_{sp}}. \tag{2.7}$$

The rate of spontaneous emission therefore depends on the lifetime of spontaneous emission τ_{sp}. A more complete description of the population can be obtained by combining equations 2.1, 2.2, and 2.7

$$\frac{dN_2}{dt} = -\sigma_{21} F N_2 - \frac{N_2}{\tau_{sp}} + \sigma_{12} F N_1. \tag{2.8}$$

The steady state solution for this system with total population N_0 can be derived from Equation 2.8 [29]

$$\Delta N = \frac{N_0}{1 + 2\sigma_{21} F \tau_{sp}}, \tag{2.9}$$

where $\Delta N = N_1 - N_2$. For two energy levels of the same degeneracy, the population inversion condition (Equation 2.5) simplifies to $\Delta N < 0$. At low photon fluxes, the population difference will be equal to the total population N_0, corresponding to the entire population being in the lower energy level, but even at higher photon fluxes, $\Delta N \geq 0$. Consequently, the simple two-level system above shows that, in practice, in such a system population inversion cannot be achieved when using an optical pump to raise the population to the higher energy level. This concept, referred to as two-level saturation, has led to the development of three-level and four-level lasers (Figure 2.1). In a three-level laser system, an additional energy level (upper lasing level or ULL) close to the

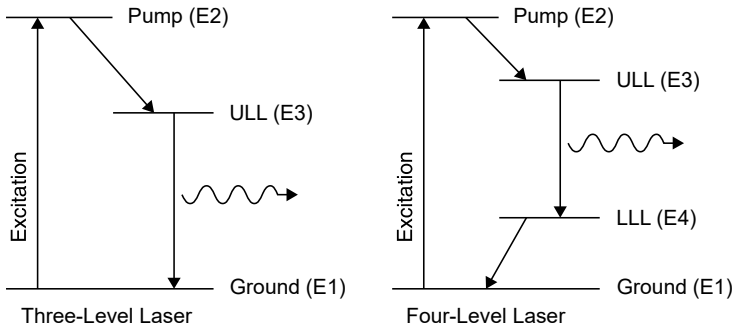

Fig. 2.1. Energy levels in three- and four-level laser systems, adapted from [29].

higher energy level is added such that a fast non-radiative transition from E_2 to this new level can populate the ULL level while avoiding saturation. The population inversion and consequently the lasing process occur between this additional ULL and the ground level

E_1. In a four-level system, an additional energy level (lower lasing level LLL) is added with slightly higher energy than the ground state such that photons again quickly decay from LLL to the ground state. This additional level is, due to its higher energy, much emptier than the ground state, therefore population inversion can be reached with a much smaller population in the ULL, such that lasing from the ULL to the LLL is much more readily achieved than in a three-level system. Consequently, the more efficient active materials are four-level systems, as well as quasi-three level lasers, where the ground state is split into suitable sub-levels such that the system effectively behaves like a four-level laser. Note that in the above discussion and in Figure 2.1, the numbering convention of labelling the energy levels (E_1-E_4) was chosen for consistency with the introductory discussion of the two-level system in this chapter, but in other literature, the energy levels are also commonly numbered in order of increasing energy. An analysis of the populations of the respective energy levels with so-called *rate equations*, analogous to those derived for the simple two-level laser discussed here, is an important mathematical tool for the description of such systems.

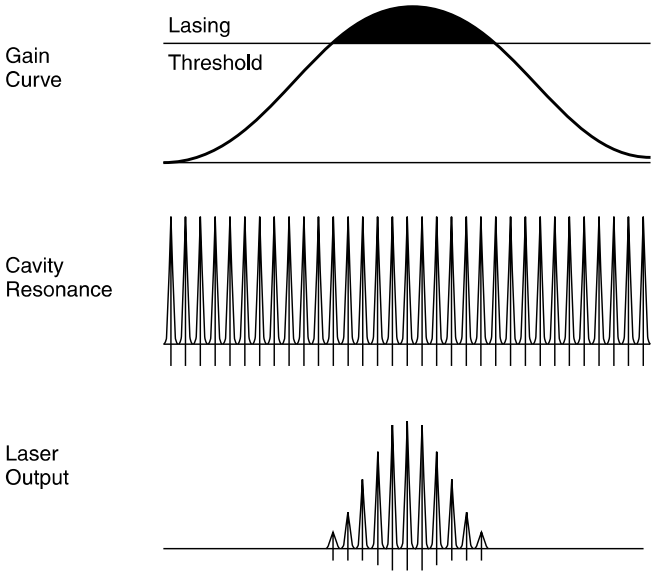

Fig. 2.2. Material gain (top) and cavity resonances (middle), that combine to produce the laser output (bottom). Reproduced from [29].

Mathematical analysis of the system also highlights that for stimulated emission the photon flux needs to be high, which is most commonly achieved by the optical feedback structure that contains the photons inside the laser cavity. Consequently, laser output is observed at discrete resonances of the cavity that lie within the gain spectrum of the material (Figure 2.2), given that the gain can compensate the losses of the system which are lowest at the resonances. The requirement of the gain overcoming the losses can be

expressed mathematically, here for the example of a simple resonator consisting of two parallel mirrors of reflectivities R_1 and R_2, forming a cavity of length L[30]:

$$E_0\sqrt{R_1R_2}e^{(g-\alpha)L}e^{\frac{i4\pi nL}{\lambda_0}} = E_0. \tag{2.10}$$

The first part of Equation 2.10 shows that, following one round trip around the cavity, the gain needs to overcome losses due to reflections and due to absorption with absorption coefficient α, while the imaginary exponential term signifies the need for the lasing wavelength λ_0 to constructively interfere following a round trip. The point at which Equation 2.10 is satisfied is defined as the onset of lasing, which is also termed *(lasing) threshold*. The threshold is an important concept in characterising lasers and will be revisited in Chapter 2.1.4. A discussion of optical feedback structures, particularly the resonators used in the present work, will be provided in Chapter 2.1.2, following a more detailed analysis of active materials. A wide range of materials with appropriate energy levels has found their application as gain materials, and the physical state of the gain medium is a straightforward description conventionally used to group lasers into three main groups, i.e., gas lasers, liquid lasers, and solid-state lasers[28]. In the following two sections, the two solid-state material platforms used in this work as active materials will be introduced, which are organic dyes and semiconductors, in particular semiconductor quantum wells.

Molecules and organic dyes

Organic dyes are typically π-conjugated molecules that can be dissolved in a liquid solvent or doped into a rigid matrix. Common classes of dyes emitting in the visible are Coumarin and Xanthene dyes, such as Rhodamine6G[28]. They act as quasi-four level systems, using both electronic and vibrational energy levels of the molecule. The molecules are excited from the ground state (Figure 2.3, Level 1) into a higher electronic and vibrational level (Level 2), and subsequently show a very fast (<1 ps) decay to the vibrational ground state (Level 3)[31]. Population inversion can therefore build up, and emission can take place from many of the vibrational levels of the electronic excited state to one of many vibrational levels of the electronic ground state (Level 4), before again decaying quickly to the vibrational ground state. Due to the range of available transitions, whose probability is given by the Franck-Condon principle, the emission spectrum is typically broad and shows a large Stokes shift, i.e. a large spectral separation between the maxima of the excitation and emission spectrum. Further, dye molecules have a large transition dipole moment μ, and both absorption and stimulated emission cross section, which scale with

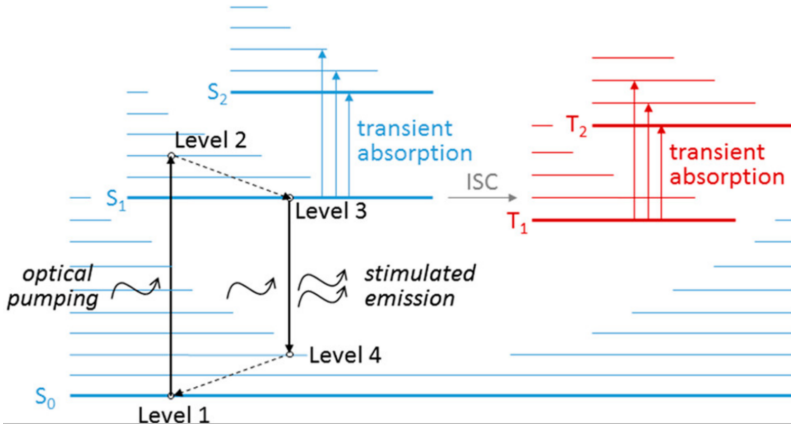

Fig. 2.3. Jablonski diagram of an organic luminophore, showing electronic and vibrational energy levels that are involved in lasing, as well as routes for parasitic losses. Reproduced from [31].

μ^2, are therefore large[28]. The above transitions conserve spin and involve exclusively singlet states, but triplet states can be generated through intersystem crossing (ISC) and constitute an important source of loss. Due to the large Stokes shift, however, absorption losses are low at the lasing wavelength[28, 31]. The losses from self-quenching, i.e. the reduction of emission intensity due to interactions between the fluorophores, are addressed by dissolving the dye molecules in a transparent dielectric matrix, e.g. a polymer. A high-index polymer like polystyrene is advantageous for producing rigid microcavity dye lasers, where the matrix material simultaneously forms the optical feedback structure. Spherical cavities, which are attractive optical micro-resonators as will be discussed in Section 2.1.2, readily form due to surface tension during solution processing. Therefore, this approach lends itself well to produce dye-doped microdroplet and microbead lasers[16, 31].

Semiconductors and quantum wells

Many inorganic semiconductor materials are crystals with highly delocalised electron systems, whose energy levels are described as bands due to the interactions between a large number of atoms. Direct band gap semiconductors, such as III-V materials, can provide gain for lasing which involves transitions between the valance and conduction bands. A semiconductor can act as a three-level laser system, when the lifetime of intraband transitions is much shorter than that of interband transitions, such that upon raising a given population to the higher level, i.e. the conduction band, the valence and conduction bands can both be filled to their respective quasi-Fermi levels E_{F_C} and E_{V_C} and population inversion can be established. Such a material can provide gain over a range of energies

given by the Bernard-Duraffourg condition

$$E_g \leq h\nu \leq E_{F_C} - E_{F_V}, \tag{2.11}$$

which says that the energy of the emitted photon needs to lie between the band gap energy E_g and the separation of the two quasi-Fermi levels. This gain spectrum of the bulk semiconductor can be adjusted by strategic alloying of different materials, which allows to shift the respective energy levels. Such an approach has for example been used for producing nanodisk lasers with emission over an extended spectral range by mixing lasers produced from alloys with different compositions (Figure 2.4)[32].

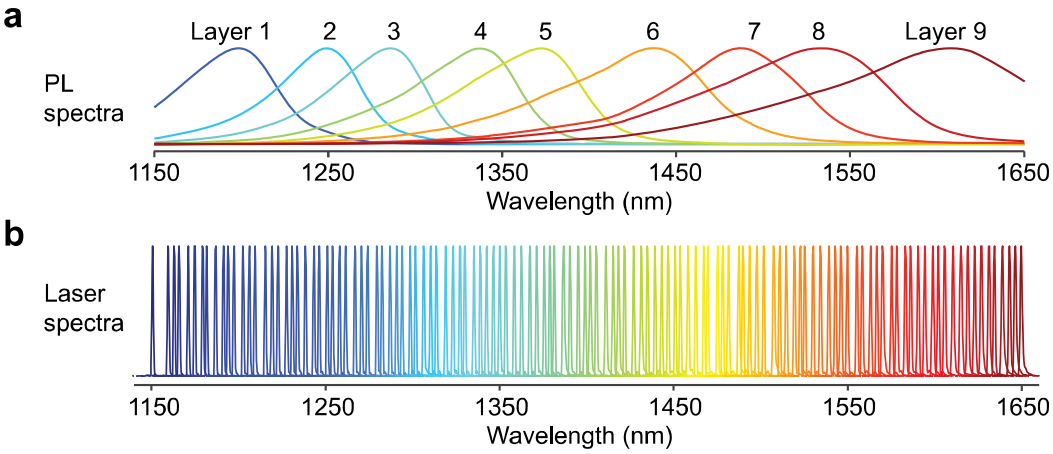

Fig. 2.4. Producing semiconductor nanodisk lasers with emission spanning a large spectral window. a, Emission spectra from 9 different materials that were used for nanodisk laser fabrication. **b,** Corresponding lasing spectra of 126 devices fabricated from the different materials. Adapted from [32].

Although bulk semiconductors are already very attractive laser materials due to their photostability and high quantum efficiency, further advantages are offered by quantum-confined structures such as semiconductor quantum wells. Semiconductor quantum well (QW) structures contain various layers of semiconductors with different band gaps. The width of each layer is comparable to the de Broglie wavelength of the electrons, which typically corresponds to a few tens of nanometres. Consequently, the energy band structure of the QW is a function of position, which is one-dimensional in the case of a layered material[33]. Typically, such a structure contains alternating layers of materials with a lower band gap (well) and a larger band gap (barrier). The electrons, which are confined in this one-dimensional finite potential well, have quantised energies that follow solutions

of Schrödinger's equation, where

$$E = \frac{\hbar^2 k_{xy}^2}{2m} + n^2 \frac{\hbar^2 \pi^2}{2mL_z^2}. \tag{2.12}$$

This expression is valid for both valance and conduction bands by using their respective electron masses m. The corresponding density of states is a step-wise function with steps representing individual subbands of quantum number n, and the state energy is now, as opposed to the bulk semiconductor, also affected by the thickness of the well L_z[28, 33]. Analogous to the bulk semiconductor, a quasi-Fermi level is established in the valence and conduction bands, with the additional requirement in the QW for transitions to occur between subbands of the same n. Owing to the different density of states in QWs, the differential gain compared to the bulk is substantially larger. Another consequence of Equation 2.12 is that the optical properties are now tuneable by adjusting both composition and thickness of the layers, giving further options for engineering the band gap of the structure. Expected emission wavelengths of GaInP QWs, the material platform used in the present work, are shown in Figure 2.5[34], where it can also be seen that at increasingly large well widths, further changes in width have smaller effects on the energy landscape due to the properties gradually approaching that of the bulk material.

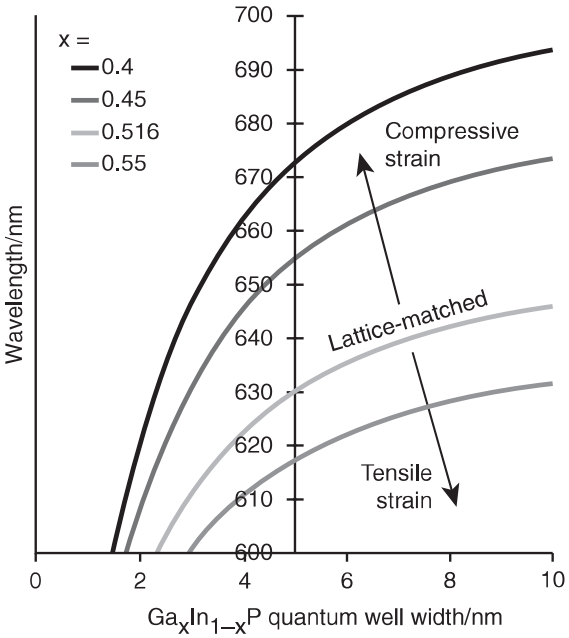

Fig. 2.5. Emission wavelength of GaInP QW structures, depending on their composition and the QW width. Reproduced from [34].

An important consequence of changing the material composition stems from the resulting change in lattice constant of the cubic (for III-V semiconductors) structure. Due to a mismatch of lattice constant, either tensile or compressive strain is induced, which breaks the cubic symmetry and affects both electron mass and band gap[28]. In compressively strained quantum wells, the electron transparency density is reduced and the differential gain is increased, leading to greater efficiency and lower lasing thresholds. However, increasing the strain beyond a certain point also increases the risk of forming dislocations[35], e.g. in AlGaInP/GaInP QWs, successful devices have been shown up to a compressive strain of 1.1%[1, 36].

Lastly, due to selection rules for electronic transitions in QW structures, transitions corresponding to an electric field vector parallel to the layer structure (TE polarisation) are favoured, leading to a higher gain for TE than for TM modes[37–39].

Microlasers from semiconductors and semiconductor QWs can be produced by well-established semiconductor fabrication techniques such as lithography and dry or wet chemical etching[17, 39]. The fabrication protocol used in this work is summarised in Appendix A.1. Nanodisk geometries are not only popular due to the ease of fabrication, but also provide strong confinement of the mode within the gain region[40].

Continuous Wave and Pulsed Operation

An important distinction pertains to the mode of operation of lasers, which can be either continuous wave (CW) or pulsed. Generally, pulsed operation is more readily obtainable in many materials, whereas various challenges must be overcome to realise CW lasing. In dye molecules, the lifetime of triplet states is typically much greater than the luminescent lifetime, therefore population inversion can be much more easily obtained by short and intense pulses of excitation[31, 41]. Semiconductor lasers often have more favourable lifetimes for CW operation and many large laser diodes can be operated in the CW regime. The dominant effect preventing CW lasing in semiconductor microlasers is heating because the lasing threshold drastically increases with temperature[42] and particularly in free-standing microscopic lasers with a minimal device size, it is difficult to implement any heat sinking. The microlasers used in the present work are exclusively operated in the pulsed regime, which is readily achieved by optical excitation with short ($< 1\,\mathrm{ns}$) pulses.

2.1.2 Optical feedback and cavities

The role of the optical feedback structure is to confine photons inside the laser cavity to increase the photon flux and thereby the rate of stimulated emission, and to ensure coherence of the emitted photons. Equation 2.10 has already shown two key aspects of the role of the optical feedback structure: It needs to support resonances of constructive interference within the material gain spectrum, and its losses should be minimised.

There are many suitable geometries for such resonators spanning a vast range of sizes down to miniaturised devices of dimensions comparable to the laser wavelength. The miniaturisation of lasers is limited by two aspects[30]: i) in conventional dielectric cavities, the diffraction limit poses a limit on the minimal device size, and ii) in microscopic cavities, it becomes a greater challenge for the gain to overcome the losses (as can also be seen by Equation 2.10). These challenges can be addressed by the use of high-index, high-gain materials such as semiconductors, and by confining light in metallic nanostructures[43, 44]. The first approach also is widely used in the field of bio-integrated microlasers, where a small device footprint is particularly relevant for any intracellular applications[4, 7, 17, 24]. One cavity type frequently used for intracellular lasing are whispering-gallery-mode resonators, which can be realised e.g. as spherical or cylindrical lasers with cavity diameters of a few hundreds of nanometres[7, 17] to a few micrometres[4, 5, 9].

Whispering-gallery-mode resonators

WGM resonators are circular resonators first mathematically described by Lord Rayleigh in the context of acoustic resonances originating from reflections of a concave wall in St. Paul's cathedral[45]. Analogous to these acoustic resonances, optical resonances can form in a concave resonator where the light is confined through total internal reflection from the surface of the resonator (Figure 2.6).

The general mathematical description of waves confined in a circular resonator is based on a formalism of Maxwell's equations in polar coordinates and was applied to describe light scattering from spherical colloidal particles by Mie[46] and Debye[47]. A resonance size parameter

$$x = \frac{2\pi n_h r}{\lambda} \tag{2.13}$$

is introduced, with n_h as the refractive index of the host medium and r the radius of the resonator. Selecting boundary conditions that require the continuity of the tangential

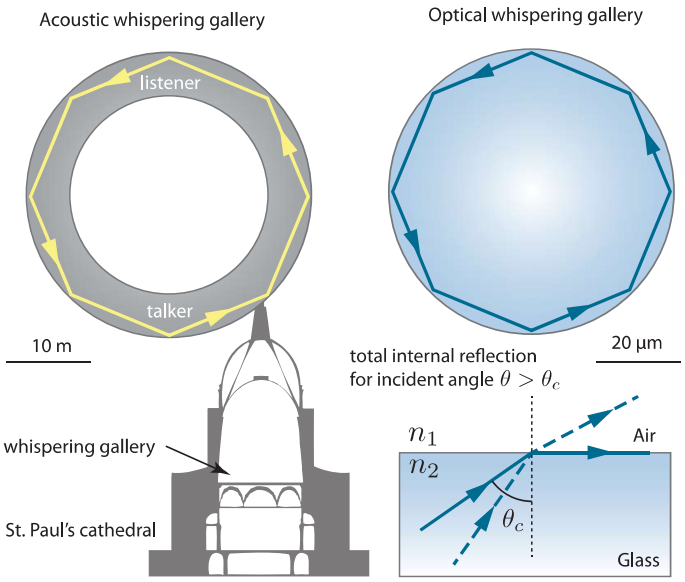

Fig. 2.6. Left: Acoustic WGM found in St. Paul's cathedral. Right: Optical WGM confined in a glass bead by total internal reflection from the glass-air interface. Reproduced from [12].

components of the magnetic and electric field at the resonator-host interface[47] allows to express the solutions in form of a transcendental equation, here expressed with nomenclature mainly consistent with [12]:

$$\frac{[n_h x y_m(n_h x)]'}{y_m(n_h x)} = N \frac{[n_r x j_m(n_r x)]'}{j_m(n_r x)}. \tag{2.14}$$

Equation 2.14 describes the eigenfrequencies of the spherical resonators, and is based on the Bessel functions $j_m(x)$ and $y_m(x)$. n_r is the refractive index of the resonator, and the prime symbol ($'$) denotes the first derivative with respect to x, which in return is a function of the radial position r. Equation 2.14 treats the two cases of i) the electric field parallel to the resonator surface (TE) and ii) the magnetic field parallel to the resonator surface (TM) which have different expressions for N, namely

$$N = 1 \tag{2.15}$$

for TE resonances, and

$$N = \frac{n_h^2}{n_r^2} \tag{2.16}$$

for TM modes. The respective solutions can be further grouped according to three mode

numbers: The radial mode number n, the azimuthal mode number l, and the polar or angular (momentum) mode number m. It is generally assumed that the wavelength of the WGMs observed in the resonators used here have very low radial mode numbers, usually $n = 1$[48], which corresponds to a mode located close to the surface of the resonator (Figure 2.7c).

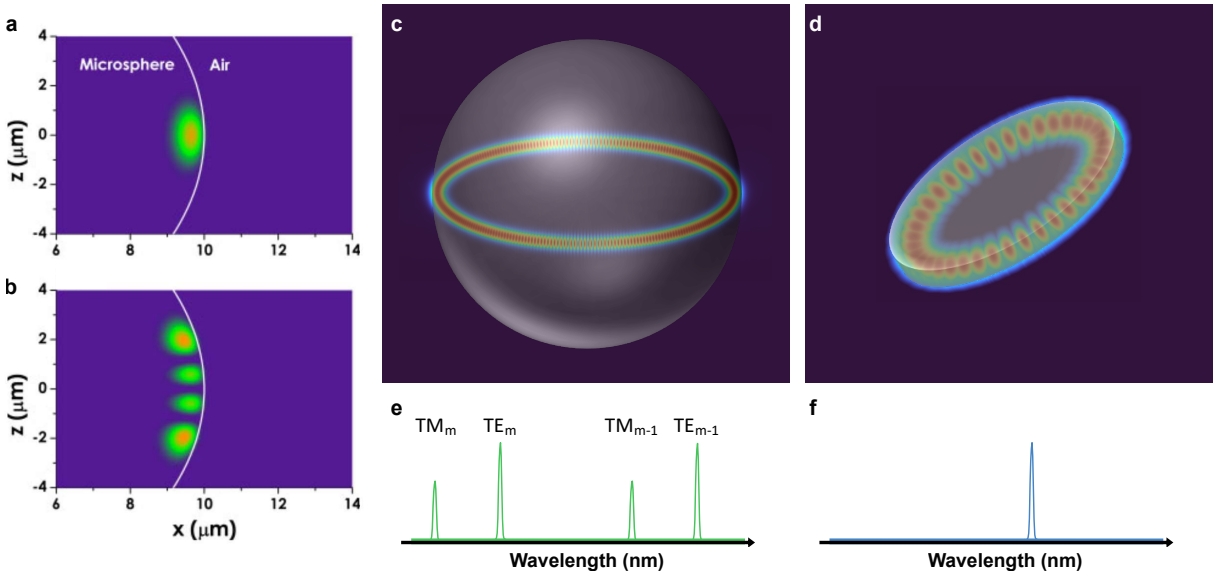

Fig. 2.7. Cross-sectional view of the Poynting vector of two WGMs in spherical resonators, both of fundamental radial mode number and of **a,** fundamental azimuthal mode number and **b,** higher order azimuthal mode number. Reproduced from [48]. **c,** 3D illustration of the electric field intensity distribution of a fundamental ($n = 1$, $|l| = m$) mode in a spherical resonator; m=138, d=12 µm. **d,** Fundamental ($n = 1$, $|l| = m$) mode in a nanodisk resonator; m=19, d=1.7 µm. **e,** Illustration of a multi-mode lasing spectrum with modes described by the polarisation (TE/TM) and the angular mode number m. **f,** Single-mode lasing spectrum, which is commonly observed in small cylindrical resonators.

The azimuthal mode number pertains to maxima in the plane perpendicular to the plane of the circular path (Figure 2.7a,b), and modes of different azimuthal mode numbers are degenerate in spherical resonators. In thin cylindrical resonators such as the nanodisk resonators used in this work, the higher-order azimuthal modes (here corresponding to the z-direction of the cylinder) are typically not supported[49](Figure 2.7d), and for disks of thickness $\frac{\lambda}{4n}$, TM modes are also not supported[40]. The analytical solutions presented here pertain to the case of homogeneous and isotropic n_h and n_r, while more complex scenarios are typically solved numerically (Section 2.1.5).

In summary, it follows that the wavelength of the modes can usually be sufficiently described by specifying the polarisation (TE or TM) and the angular mode number m in

addition to knowledge of the physical parameters of the system, i.e. the size of the resonator r and the refractive indices of the resonator, n_r and its environment, n_h (Figure 2.7e). Physically, m represents the number of maxima along the circular path. In practice, depending on the geometry of the resonator, its refractive index, and the available gain, either a single mode (Figure 2.7f) or multiple modes are simultaneously observed. The corresponding spectra in these two scenarios are referred to as single-mode or multi-mode spectrum, respectively.

2.1.3 Optical pumping

Following the introduction of the active material and the resonator, the following section provides a discussion of the third constituent of lasers: The pump source, which excites high-energy states to achieve the population inversion. The two main methods of this process are electrical and optical pumping. In electrical pumping, charge carriers are injected into the active area, e.g. by current flowing through a semiconductor diode[28]. In the process of optical pumping, excited states are a result of the absorption of a photon, which is the mechanism involved in the rate equation introduced in Section 2.1.1, and the prominent method of exciting WGM microcavity lasers. Optical pumping can be achieved using an incoherent light source like a strong lamp, but is more efficiently obtained with laser pumping, e.g. using an electrically driven diode laser as a pump. A pump source of power P will excite higher-energy states in a volume of cross section A and length l at a rate of R_p according to

$$R_p = \eta_p \frac{P}{Alh\nu_{mp}}, \tag{2.17}$$

where ν_{mp} is the frequency difference between the ground state and the excited state. The total pump efficiency η_p is a combination of various contributions:

$$\eta_p = \eta_r \eta_t \eta_a \eta_{pq}, \tag{2.18}$$

where the four terms represent the radiative efficiency, transfer efficiency, absorption efficiency, and power quantum efficiency, respectively. These efficiency terms depend on the spectrum of the pump and the absorption coefficient of the medium[28], but also on geometrical aspects like position, orientation, and polarisation of the pump[18, 50]. The transfer and absorption terms are improved by efficient incoupling to the resonator, and further, molecules whose dipole moment is well-aligned with the pump are excited more efficiently[51, 52]. Therefore, certain pump geometries can lead to preferential excitation

of specific planes or mode families in WGMs [53, 54] and other types of lasers such as solid-state Fabry-Perot cavities[55, 56] and random lasers[57], an observation which is also experimentally confirmed in this work (Section 4.3.2).

2.1.4 Lasing in microcavities

Following the introduction of the main constituents of lasers, particularly of WGM microcavity lasers, their emission properties can now be explained through a more detailed discussion of the system properties and the lasing process. The qualities of lasers, i.e. directionality, monochromaticity, and coherence, as well as their threshold energy, result from physical properties and concepts that will be explained here with particular emphasis on WGM microcavities.

Q-factor and linewidth

The emission spectrum of a perfectly monochromatic laser would be characterised by an infinitely narrow linewidth, which is not representative of real lasers. For devices based on materials with very broad gain spectra, the linewidth is determined by the losses of the cavity (*lifetime broadening*)[28, 29, 58]. A lossier cavity will have a shorter lifetime τ_c and show a Lorentzian line shape with width

$$\Delta\omega = \frac{1}{\tau_c}. \tag{2.19}$$

The cavity quality factor, or Q-factor, is introduced as a measure of the loss of cavities. The implications of the cavity quality for the device characteristics will be discussed below, following a description of the Q-factor of WGM lasers. The Q-factor is defined as

$$Q = \frac{\omega}{\Delta\omega} = \tau_c\omega. \tag{2.20}$$

A large Q-factor represents a cavity with low losses. Various sources of loss contribute to the total Q-factor and are added reciprocally[48]:

$$\frac{1}{Q} = \frac{1}{Q_{rad}} + \frac{1}{Q_{mat}} + \frac{1}{Q_{s.s.}} + \frac{1}{Q_{cont}}. \tag{2.21}$$

Q_{rad} represents the curvature losses, corresponding to less perfect total internal reflection with increasing curvature. Q_{rad} scales with angular mode number m; therefore, resonators

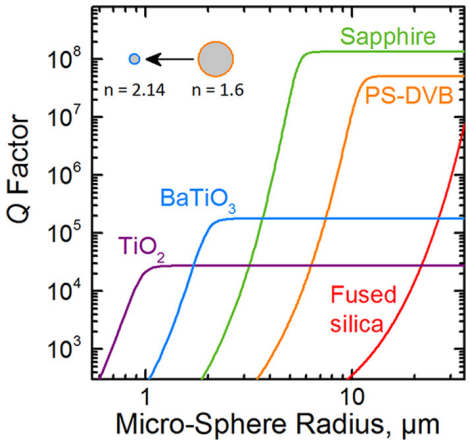

Fig. 2.8. Dependence of the total Q-factor on the radius of microspheres made from materials with different refractive indices. Reproduced from [4].

of large refractive index and large size have low curvature losses. Q_{mat} corresponds to Rayleigh scattering and absorption in the bulk material and generally is approximately inversely correlated with λ. The surface scattering term $Q_{s.s.}$ depends on size and correlation length of surface inhomogeneities, highlighting the benefit of smooth cavity walls. Lastly, Q_{cont} takes possible contamination of the resonator surface into account. As shown by Equation 2.21, the greatest source of loss will dominate the total Q-factor, which is typically limited by curvature losses for small resonators and by material absorption for larger resonators (Figure 2.8)[4]. Consequently, a lower size limit is imposed below which the losses become challenging to overcome.

Purcell factor

The presence of a resonator also affects the radiative properties of the emitters, i.e. the excited states in the systems discussed above. This effect was first discovered by Purcell[59], who found that the rate of spontaneous emission of an emitter inside a resonator is increased by the factor

$$f = \frac{3Q\lambda^3}{4\pi^2 V} \tag{2.22}$$

that depends on the wavelength, the cavity Q-factor, as well as the volume V of the resonator. This enhancement is attributed to an increased photon density of states for a transition resonant with the cavity mode[58], and notably, reaches larger values for smaller cavity volumes. The consequence of a high Purcell effect is a larger share of the spontaneous emission into the lasing mode, which helps to reduce the lasing threshold[43, 60]. The fraction of spontaneous emission into the lasing vs non-lasing modes is described

by the β-factor, where $\beta = 1$ corresponds to all photons emitted into the lasing mode even below the lasing threshold, therefore called a *thresholdless laser*.

Lasing threshold

While it is intuitive that a higher photon number in the lasing mode reduces the lasing threshold, this assumption can also be confirmed mathematically. To show this, an expression for the threshold of a given system can be derived, starting again from the rate equations describing the populations of the energy levels of the system and accounting for all possible transitions between the levels. For the case of a semiconductor laser with cavity decay rate T, the steady-state solution for the photon number n achieved by a pump rate P could be derived from the rate equations for a four-level system[60]:

$$n = \frac{1}{2T\beta}\left[-(T-\beta P) + \sqrt{(T-\beta P)^2 + 4T\beta^2 P}\right]. \tag{2.23}$$

Plotting the resulting input-output curve for different values of β shows that with decreasing β, the curves show a more steep transition which is found at higher pump rates (Figure 2.9).

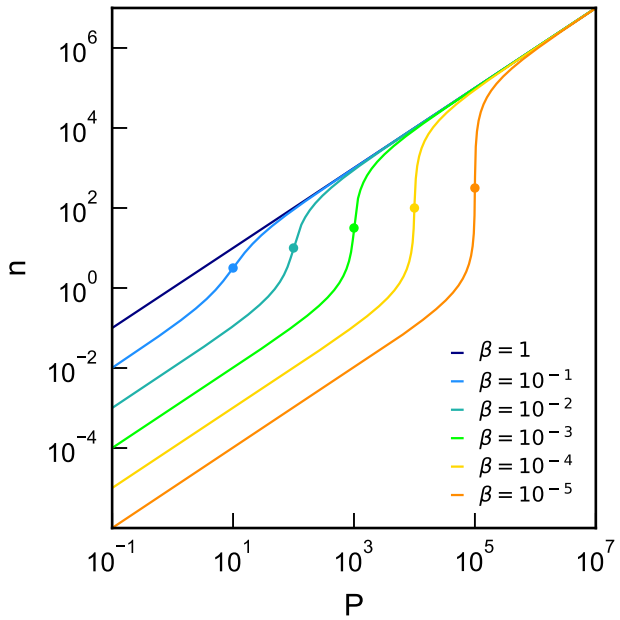

Fig. 2.9. Input-output curves for semiconductor microlasers (solid lines) with different β-factors. The lasing thresholds of each curve are indicated by the symbols.

An expression for the lasing threshold power P_{th}, which is located at the inflection point,

can be derived from the rate equation model:

$$P_{th} = \frac{T}{\beta}. \tag{2.24}$$

Here, we indeed recover the expected inverse correlation of β-factor and threshold. Additionally, a higher lasing threshold is associated with a faster cavity decay rate, or shorter cavity lifetime, therefore high-Q cavities are expected to lower the lasing threshold.

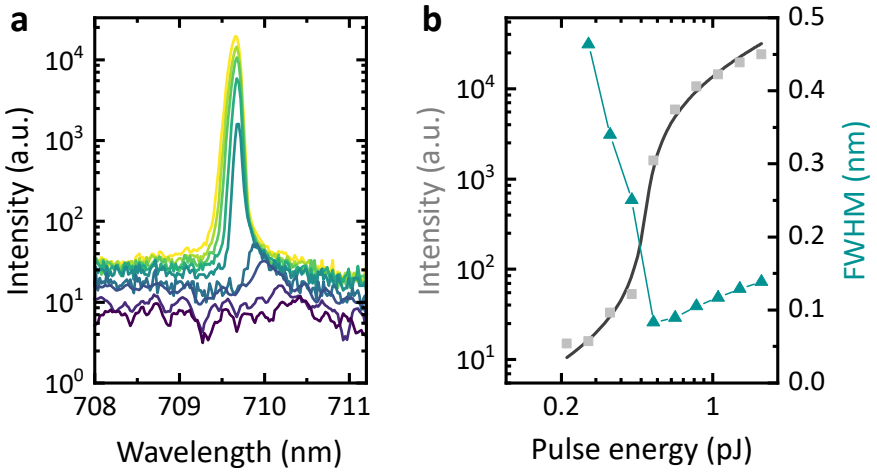

Fig. 2.10. **a**, Spectra emitted by a semiconductor nanodisk laser under increasing pump power. **b**, Corresponding input-output curve (grey) and linewidth (cyan), showing an increase in emission and narrowing of the linewidth at threshold. Adapted from [1].

Consequently, the lasing threshold of semiconductor microlasers can be calculated from fitting experimental data of the lasing output with increasing pump powers (Figure 2.10 a) to Equation 2.23 (Figure 2.10 b). The linewidth of the cavity mode also typically narrows when transitioning into the lasing regime because the Q-factor of the microcavity depends on the ratio of stimulated emission to losses, leading to a greater linewidth of the cold cavity, i.e. below threshold[61]. The emergence of a sharp and narrow peak around the lasing threshold (Figure 2.10 b) therefore is one of the hallmarks of a laser[41].

Directionality of lasing emission

Generally, laser light is thought of as highly directional. Due to the large degree of coherence, laser light can be collimated and maintain a narrow beam upon propagation[29]. However, the laser light can be highly divergent at its origin, which is typically the case for

microcavity lasers. The divergence of the emission is Fourier-related to the spatial distribution of the mode inside the cavity, which, for a miniaturisation in all spatial dimensions, leads to a more even aspect ratio and therefore a larger solid angle of emission[58].

This relationship between spatial distribution and angular emission also holds for WGM cavities, which, due to their rotational symmetry, emit isotropically in the plane of propagation[62]. Spherical microcavities can, due to their symmetry, support WGMs in any plane, and therefore show omnidirectional lasing emission. In cylindrical geometries, such as nanodisk lasers, a larger share of the emission is aligned with the plane of the resonator (Figure 2.11a)[18, 63]. This emission profile can be engineered by introducing smooth,

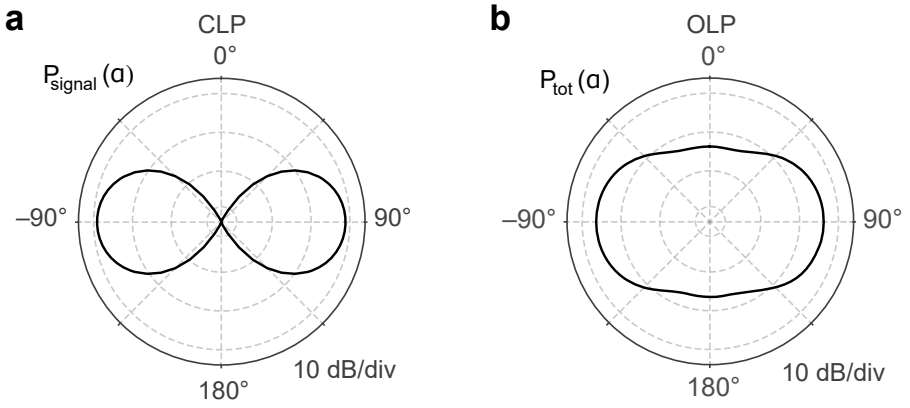

Fig. 2.11. Directionality of the emission from a nanodisk laser, with 0^o corresponding to the cylindrical z-axis. **a,** Emission from a conventional nanodisk (CLP) and **b,** from an optimised laser particle (OLP). Reproduced from [18].

symmetric deformations, which can be optimised for directional emission in the axial direction, i.e. 0^o in Figure 2.11[63, 64]. Strategically placed scatterers on the other hand can lead to more omnidirectional emission (Figure 2.11b)[18].

Depending on their geometry, nanowires can support both Fabry-Perot and Whispering-gallery-mode resonances, and due to their even more anisotropic aspect ratio, their emission is predominantly directed out of their tips[24, 27].

In summary, the directionality of the microlaser emission is a consequence of the spatial distribution of the cavity mode and therefore of the cavity geometry, which can be tuned to achieve the angular emission profile most beneficial for a given application.

2.1.5 Theoretical considerations for applications of microlasers

For most applications of WGMs, it is desirable to analyse the experimentally measured spectra by assigning correct mode numbers to each peak in the spectra. However, the transcendental Equation 2.14 cannot be solved exactly, which poses a challenge for the processing of lasing spectra. An alternative is offered by analytical approximations that express the solutions in terms of asymptotic expansions, such as the model by Schiller[65]

$$x_m^{(l)} = \frac{\nu}{n} - \frac{\zeta_l}{n}\left(\frac{\nu}{2}\right)^{\frac{1}{3}} + \sum_{k=0}^{k_{max}} \frac{d_k(n,\zeta_l)}{\nu^{\frac{k}{3}}(n^2-1)^{\frac{k+1}{2}}}. \tag{2.25}$$

where n is the relative refractive index $n = \frac{n_r}{n_h}$, ν scales with the angular mode number as $\nu = m + \frac{1}{2}$, ζ_l is the l^{th} zero of the Airy function, and d_k are polarisation-dependent coefficients provided in reference[65] up to $k = 8$. Dropping all higher order terms in Equation 2.25, and substituting according to Equation 2.13 allows to derive a much simpler expression:

$$2\pi r n_r \approx m\lambda_m, \tag{2.26}$$

which is frequently used as an intuitive description of the WGM mode positions. However, in this approach, the dependency of the mode position on the external refractive index is lost. Therefore, n_r in Equation 2.26 is replaced by an effective refractive index n_{eff}, which is introduced as a pragmatic expression capable of indicating the dependence of the mode positions on both n_r and n_h:

$$2\pi r n_{eff} = m\lambda_m. \tag{2.27}$$

It is immediately apparent that Equation 2.27 lacks the necessary accuracy to solve the problem of mode assignment, but it is useful for a qualitative discussion of the properties of WGMs that enable their applications. Firstly, we note that the observed mode positions scale with the size of the resonator, and changes of just a few nanometres to the size of the resonator result in a change of mode position by tens to hundreds of picometres, depending on the type of the resonator and the mode number. These spectral changes are easily resolved through high-resolution spectroscopy. Consequently, WGM lasers of slightly different sizes posses unique and distinguishable spectra, which has led to their use as optical barcodes. It is estimated that thousands or even millions of unique barcodes can be created in such a way, depending on the type and number of resonators used[66]. The dependence of the lasing mode on n_{eff} poses a challenge for the reliability of this tracking mechanism and can either be overcome by stabilising the wavelength through

encapsulation[67] or by inferring the size of the laser from its spectrum and using this as the barcode (applicable to multi-mode resonators only). For the second approach, the free spectral range (FSR) can be a useful label for barcoding and tracking[4], as it is directly related to the size of the resonators. The FSR describes the spacing between adjacent modes of the same polarisation in multi-mode spectra, which can be derived from Equation 2.27 to be[12]

$$FSR = \frac{c}{2\pi n r}. \tag{2.28}$$

However, a more accurate determination of the size, and therefore greater reliability in labelling, is achieved by implementing Equation 2.25 to fit experimental spectra[9].

The introduction of n_{eff} is particularly important when introducing the use of WGMs as refractive index sensors. In a general sense, using WGMs as sensors allows to detect often minuscule changes in the immediate environment of the resonator through an observed change in its spectrum. These spectral changes can be shifting, broadening, or splitting of the lasing modes[68]. They can be induced by a deformation of the resonator, allowing to sense forces when using elastic resonators[5, 69], or by changes in the optical or chemical environment around the resonator[11]. These could stem from the presence of scatterers or even active materials which can become a source of gain for the lasing mode when they are close enough such that energy can be efficiently transferred from the active material inside the cavity to the analyte near the resonator surface[70–72]. However, the

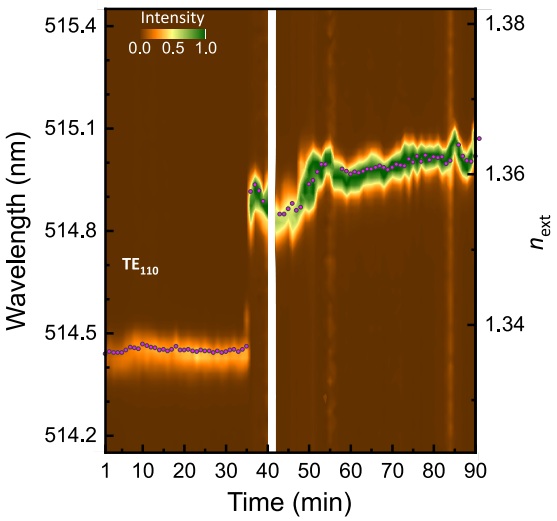

Fig. 2.12. Monitoring the position of the TE_{110} lasing peak (brown-green colourmap) and extracting the absolute refractive index around a microlaser (pink) during two consecutive measurements, showing a distinct shift in mode position and refractive index at the time of cellular uptake. Reproduced from [2].

sensing mechanism relevant for the present work can sufficiently be explained by Equation 2.25[9]: Dynamic changes in the refractive index leading to a change of the average n_h are reflected in a shift in the resonant mode position. In the context of cellular integration, this mechanism has enabled to monitor the uptake of resonators by living cells (Figure 2.12)[2, 10, 17] and the contractility of beating cardiomyocytes[9]. Dynamic sensing of the cell refractive index could find further applications in monitoring cellular processes like growth or disease progression[73]. Comparing the measured spectra to an analytical model based on Equation 2.25 allows to obtain absolute values for n_h; however, this model assumes an isotropic homogeneous external refractive index, and further methods like numerical modelling are needed when examining the effect of asymmetric refractive index perturbations.

Numerical modelling of optical resonances

Various methods for numerical solutions to electromagnetic problems exist and are attractive alternatives to analytical solutions, particularly in more complex geometries. The two most commonly applied techniques are finite element modelling (FEM) and finite-difference time-domain (FDTD)[12], the latter of which is used in the present work and will therefore be discussed here in greater detail. The FDTD approach is a numerical method of solving the time-dependent Maxwell's curl equations first demonstrated by Yee[74], who proposed discretising the $\vec{E}$- and $\vec{H}$-fields by introducing a spatial grid such that the electromagnetic problem could be expressed by a set of finite difference equations. Each so-called Yee cell in the spatial grid is of size $\Delta x \times \Delta y \times \Delta z$ and has well-defined permittivity and permeability, and well-defined fields placed strategically at

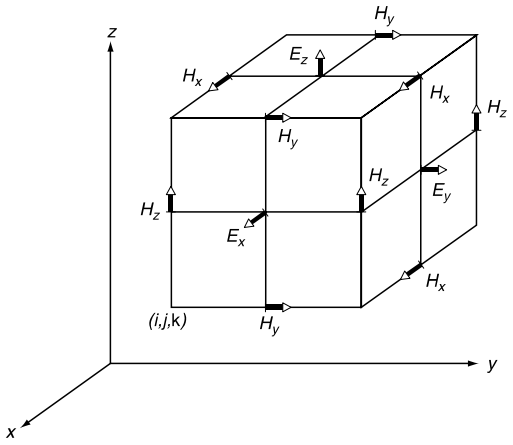

Fig. 2.13. Positions of $\vec{E}$ and $\vec{H}$ field components in the Yee cell. Reproduced from [75].

different positions of the cell (Figure 2.13), thereby naturally enforcing boundary conditions between adjacent cells, assuming the boundary is parallel to the edge of the cell[75]. For this approximation to be valid, the dimensions of the Yee cells should be substantially smaller than the wavelength. The fields are then evolved incrementally in the time domain applying the finite difference equations with a discretised time step of Δt following a leapfrog arrangement, meaning that the current $\vec{E}$-field is computed based on the $\vec{H}$-field of the previous time step, vice versa, in an iterative manner. In addition to the aforementioned requirement on the cell size, Yee introduced another stability condition defining the relationship between the spatial and temporal increments:

$$\sqrt{(\Delta x)^2 + (\Delta y)^2 + (\Delta z)^2} \geq c\Delta t. \tag{2.29}$$

Another challenge to the stability of FDTD simulations is the termination of the simulation domain without inducing reflection artefacts at the edges[76], corresponding to boundary conditions that absorb the incoming waves with as little reflection as possible. To address this, the perfectly matched layer (PML) has been proposed as an efficient solu-

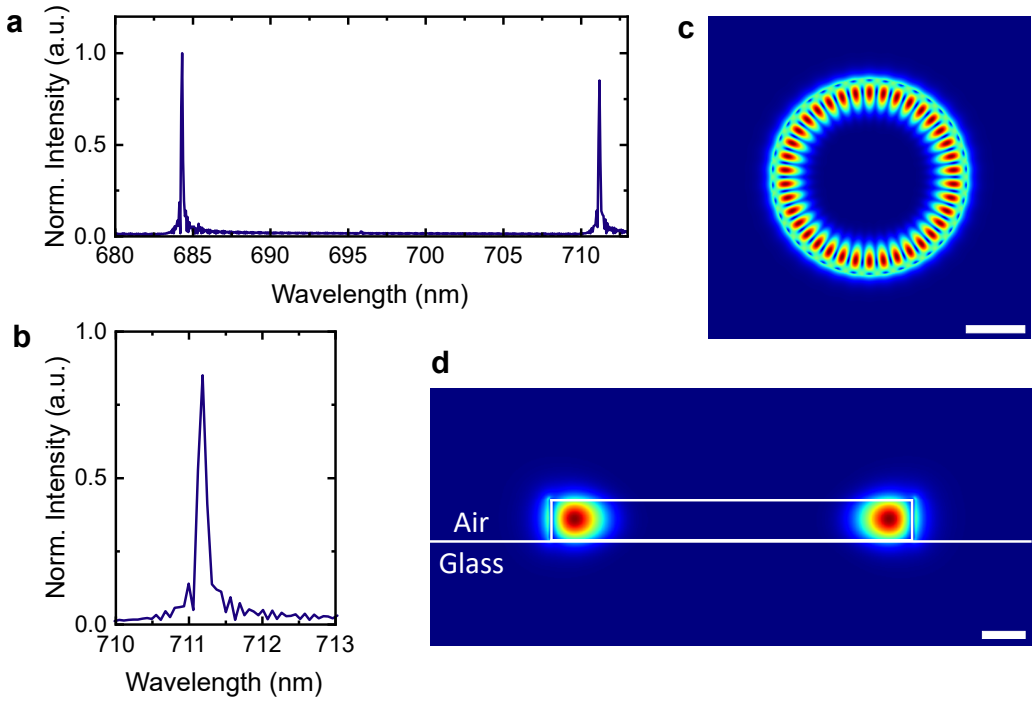

Fig. 2.14. **a,** Modelled lasing spectrum of a cylindrical WGM resonator, obtained through Fourier analysis of the time-domain simulation results, showing the TE_{19} and TE_{20} modes. **b,** Lasing spectrum from **a**, re-scaled to show the peak of the TE_{19} mode. **c,** $x - y$ cross section of the electric field intensity distribution of the TE_{19} mode. Scale bar, 500 nm. **d,** x-z cross section with the geometry of the simulation superimposed. Scale bar, 200 nm. Reproduced from [1].

tion of absorbing oncoming waves irrespective of their wavelength and angle[77], which is currently widely implemented in the form of the stretched coordinate PML[78]. Generally, FDTD is considered a robust method of directly obtaining a solution for the electromagnetic field in time and space[75], where spectral information is readily obtained through Fourier analysis[76]. Typical results of modelling WGM resonances with FDTD therefore allow obtaining spectra describing the expected peak positions (Figure 2.14 a,b) and then filtering the spatial distribution for a certain wavelength of interest to recover the expected electric field distribution of a given WGM (Figure 2.14 c,d). Here, an asymmetric environment of a resonator resting on a glass surface was readily implemented. In a similar fashion, FDTD simulations can be used to analyse the spectral response of a WGM laser to asymmetric refractive index perturbations, which will be revisited (Chapter redacted).

2.2 Fundamentals of microscopy

Collecting and analysing the signal of micro- and nanolasers requires both microscopic imaging with high spatial resolution, and spectroscopy with high spectral resolution. Semiconductor nanodisk lasers for example can have diameters of $<1\,\mu m$ and linewidths of $< 100\,pm$, which highlights the need for high-resolution measurements. Various approaches can provide suitable solutions, which will be reviewed at the end of this chapter. Among these is confocal hyperspectral imaging (CHSI), an approach originally developed for biomedical imaging applications[79] and later adapted for nanolaser readout[7], which has been implemented and further developed in the present work[2]. The goals and results of this imaging setup development will be discussed in Chapter 4, for which the theoretical groundwork will be laid in the following sections. Following an introduction of fundamental concepts of microscopy and spectroscopy, the two main technologies that are employed in CHSI, i.e. confocal microscopy and hyperspectral imaging, will be explained. The second half of this chapter covers aspects relevant for the particular case of imaging bio-integrated lasers, and therefore discusses how the optical properties of biological tissue and of micro- and nanolasers affect imaging performance and optical engineering choices, before finishing with a summary of existing solutions for imaging microscopic lasers.

2.2.1 Introduction of optical microscopy

Optical microscopy is a technique dating back to the 16th century, which has been under continuous development to find new contrast mechanisms and methods for image formation. The first and most simple microscopes fall into the category of Widefield microscopes, where a combination of lenses relays a magnified image of the whole sample onto the eyepieces or a camera. These Brightfield images can simply show light transmitted through the sample, or employ techniques like Phase Contrast, and Differential Interference Contrast. The latter two methods are widely used for unstained biological samples. An alternative is fluorescent microscopy, which typically relies on prior labelling of the samples. It can provide greater contrast, given that the stokes-shifted fluorescent emission can easily be separated from the illumination spectrally, and great specificity owing to the capabilities of fluorescent labelling[80].

There is great interest in extending fluorescent microscopy to the imaging of three spatial dimensions, which has been realised with point-scanning methods like confocal or multi-photon microscopy[81] and, more recently, light-sheet microscopy[82]. Given that, from an imaging perspective, there are some similarities between collecting fluorescence and lasing emission (i.e., the substantial spectral separation between excitation and emission), some elements of these techniques also lend themselves well to the imaging of micro - and nanolasers.

Lastly, imaging can be combined with simultaneous measurement of other information from the specimen, such as spectral information in hyperspectral imaging (HSI) or lifetime of the fluorophores of the sample in fluorescent lifetime imaging (FLIM). The first approaches, of course, is highly relevant to imaging microscopic lasers, given that both spatial and spectral information is of interest.

2.2.2 Confocal and multi-photon microscopy

Confocal microscopy was invented by Marvin Minsky in 1957 who, during his research on neural networks, struggled to obtain clear fluorescent images of a 3-dimensional sample of stained brain tissue[83]. His initial proposal to substantially reduce blurring from light scattering was to illuminate only a single point on the sample and use another symmetric objective to collect light from the same point. Two pinholes (one each in the illumination and detection path) were added to reject out-of-focus light. An even simpler alternative is to use the same objective lens for collection and split the signal from the excitation

with a dichroic mirror (the epi-illuminated confocal microscope, Figure 2.15). However, the imaging of only a single point at a time required to move the sample on translation stages to reconstruct images (i.e., point-scanning). Such a system collecting from a single

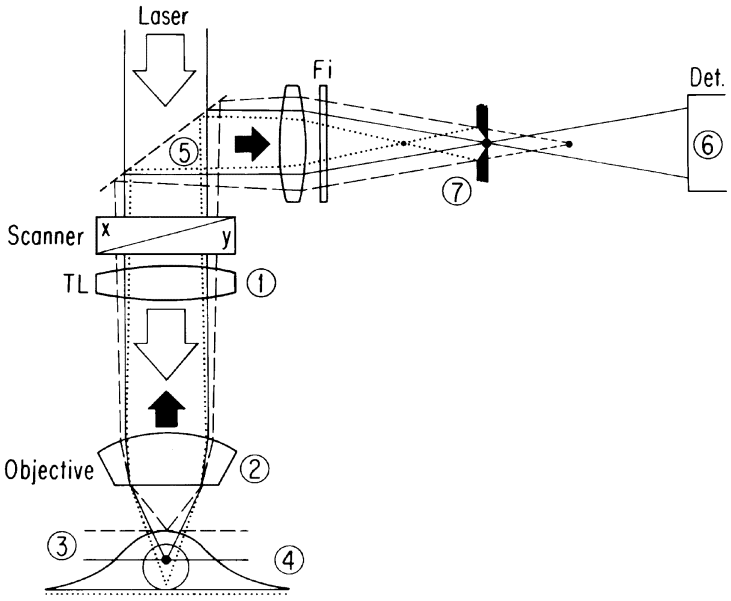

Fig. 2.15. Key components and optical path of a confocal microscope. The collected signal is separated from the excitation with a dichroic mirror (5). Only in-focus light rays (solid line) can pass through the confocal pinhole (7). Reproduced from [81].

point, which is focused in both the excitation and collection path, has some important implications including its capability of resolving objects in the axial direction, i.e., *optical sectioning*. In conventional microscopy, the resolution is defined as the minimum spot size to which the light of wavelength λ can be focused by an objective lens with a given numerical aperture (NA). From this 3-dimensional function known as the airy disk follow solutions for lateral and for axial resolution[84]:

$$d_{lat} = \frac{0.61\lambda}{NA}, \tag{2.30}$$

$$d_{ax} = \frac{2n\lambda}{NA^2}. \tag{2.31}$$

The confocal pinhole, which effectively adds a power of 2 to the intensity dependence of the airy disk, can substantially increase both lateral and axial resolution, provided that the pinhole size is small enough. The pinhole size is most meaningful when measured in relation to the size of the airy disk (1 AU representing a pinhole of the same size as the

airy disk diameter). Best resolution is achieved with a pinhole of size < 0.25 AU:

$$d_{lat} = \frac{0.37\lambda}{NA}, \tag{2.32}$$

$$d_{ax} = \frac{1.28n\lambda}{NA^2}. \tag{2.33}$$

Of course, a pinhole significantly smaller than the airy disk of the signal also rejects a substantial fraction of the light, leading to a trade-off between spatial resolution and signal brightness. Therefore, finding the optimum pinhole size is an important choice in building and operating confocal microscopes.

Confocal microscopy, which has since become a widely employed technique in biological imaging, has been subject to further research and optimisation[81]. Some important developments include $z-$scanning for 3-dimensional imaging, and the use of laser illumination, which also benefits from the high brightness and coherence of laser light. Lastly, scanning the excitation laser across the sample (as opposed to moving the sample) was implemented by adding mechanical devices such as scanning mirrors in the optical path, which is more easily achieved in an epi-illumination configuration. After these developments, the confocal laser scanning microscope (CLSM) was commercialised by various optics companies. Owing to their great 3-dimensional resolution, CLSMs are essential tools for obtaining structural images of biological samples. The resulting stacks are then often displayed as 2D-images projected along an axis of choice, which is referred to as

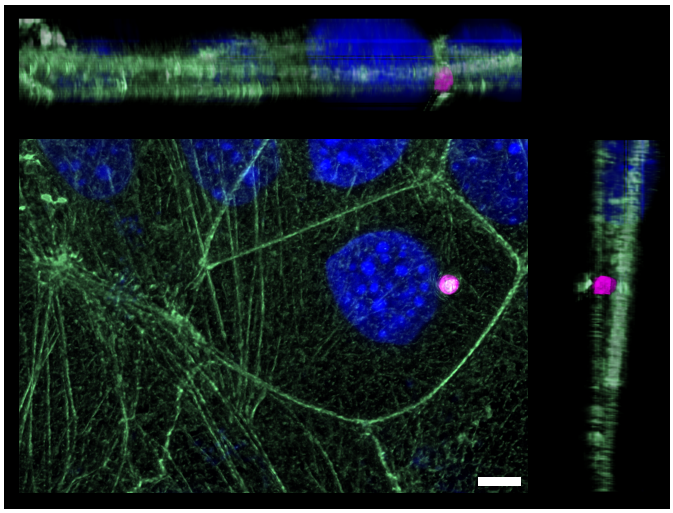

Fig. 2.16. Confocal image of stained keratinocytes with internalised nanolaser, taken on Leica Stellaris commercial confocal microscope. $x-z-$ (top), $x-y-$ (bottom), and $y-z-$ (right) MIPs, showing the signal from nuclei (blue), actin (green), and the nanolaser (magenta). Scale bar, 5 µm.

maximum-intensity-projection (MIP). An example can be seen in Figure 2.16, where confocal microscopy was used to confirm the internalisation of nanolasers by living cells and to examine the positioning of the nanolaser within the cell.

Multi-photon microscopy[85] is a technique that provides better depth penetration and intrinsic optical sectioning without the confocal pinhole. It is based on the discovery of two-photon absorption by Maria Göppert-Mayer, who described theoretically that the absorption of two simultaneous photons can excite a molecule if the sum of the frequencies of the two photons equals the frequency of the single-photon transition[86]. She also showed that this transition depends quadratically on the photon density of the excitation, so that the experimental observation of this process requires high intensity excitation and could only be achieved following the development of lasers[87]. High intensity can be achieved by focusing a pulsed laser beam with repetition rate f_p in a microscope, where the number of absorbed photons n_a per pulse is described by the following relationship[85]:

$$n_a = \frac{p_0^2 \delta}{\tau_p f_p^2} \left(\frac{NA^2}{2\hbar c \lambda} \right)^2 . \tag{2.34}$$

δ is the two-photon absorption cross section, which is a wavelength-dependent molecular property that can be found experimentally[88]. In addition to the quadratic dependence on the average pump power p_0, a higher photon density can be achieved by using pulses of shorter duration τ_p. Therefore, Equation 2.34 highlights the need for high-intensity and tightly focused excitation of ultra-short pulses (typically $\tau_p \sim 100\,\mathrm{fs}$)[85, 89]. An important consequence of the non-linear power dependency on the excitation is that the two-photon absorption rapidly decreases with increasing distance from the focus. When using two-photon excitation as a pump source in microscopy, this concept provides intrinsic optical sectioning, thereby removing the necessity of a confocal pinhole, and also limits photobleaching to the focal plane. Therefore, two-photon microscopy has allowed long-term imaging of cell cultures[85] and 3-dimensional biological samples such as embryos[90].

2.2.3 Hyperspectral Imaging

Hyperspectral imaging (HSI) is understood as the simultaneous acquisition of spatial and spectral data, leading to a 3-dimensional data set referred to as *hypercube* with two spatial and one spectral dimension [91, 92]. The low-spectral-resolution equivalent to HSI is multi-spectral imaging with a spectral resolution of $> 10\,\text{nm}$. Although originally implemented for astronomy, HSI was adapted for microscopic analysis of biological samples[92], where it has found wide applications of distinguishing fluorescent labels with higher accuracy, as well as label-free measurements of autofluorescence and reflection and absorption spectra of tissue[91].

A HSI setup consists of a light source, a detector, and a dispersive element responsible for wavelength separation. This can be further grouped into four main approaches, depending on the strategy used to reconstruct the hypercube (Figure 2.17): It can either be acquired simultaneously, i.e. snapshot HSI, or sequentially by point-scanning, wavelength-scanning and pushbroom (or line-scanning) HSI[93]. The various implementations of snapshot HSI can generally offer higher throughput at the cost of resolution, as compared to the scanning approaches. In wavelength-scanning, 2D images of the sample are required sequentially at different wavelengths, using a tuneable filter which can be mounted either in the illumination path (excitation-side) or the detection path (emission-side). Spatial scanning

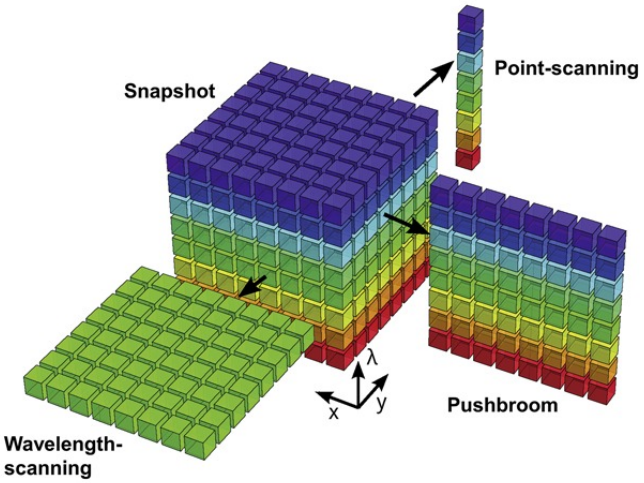

Fig. 2.17. Schematic showing various approaches of hyperspectral imaging. Adapted from [93].

methods often use a monochromator such as a grating-based spectrometer as dispersive element, which typically leads to higher spectral resolution than optical filters[91]. In pushbroom HSI, an area detector is used to scan a 2D image containing a spatial line

with spectral information $(x - \lambda)$, which is then scanned in the second dimension, i.e. y. Lastly, point-scanning performs $x - y-$scanning combined with spectral readout of a full spectrum at each voxel. Hyperspectral confocal microscopy (CHSI) is the combination of confocal scanning with spectral readout, and one of the most popular methods of point-scanning HSI. It was first implemented for fluorescent imaging of a larger number of fluorophores with more precise unmixing, where spectra of a 300 nm bandwidth and 3 nm spectral resolution were read out on a CCD camera with a spectral acquisition rate of up to 8.3 kHz[79]. CHSI can, in addition to high spectral resolution, offer the best optical sectioning, thereby allowing the acquisition of 4D $(x - y - z - \lambda)$ datasets. However, it has the lowest throughput of the methods discussed above due to only acquiring a single spectrum at a time, which can lead to comparably slow scan times.

HSI for micro- and nanolaser readout has been implemented with point-scanning using CHSI[7], pushbroom[10], as well as snapshot[94] approaches, which will be reviewed in more detail in Section 2.2.5. Wavelength-scanning methods presumably lack the necessary resolution to resolve the lasing peaks, which are spectrally much narrower than for example the emission spectrum of fluorescent labels.

2.2.4 Imaging in biological tissue

The depth of imaging, or the extent of a 3D confocal stack, is further limited by the attenuation of optical signals in tissue. The two main sources of signal loss in biological samples stem from absorption and scattering. Scattering originates from particles with substantial refractive index contrast with their environment such as cellular organelles[91] and can be approximated by Rayleigh and Mie scattering theory, assuming a collection of spherical particles of different sizes[95]. The description of the reduced scattering coefficient $\mu_s^{'}$

$$\mu_s^{'} = a^{'} \left(f_{Ray} \left(\frac{\lambda}{500\,\mathrm{nm}} \right)^{-4} + (1 - f_{Ray}) \left(\frac{\lambda}{500\,\mathrm{nm}} \right)^{-b_{Mie}} \right) \tag{2.35}$$

depends on three coefficients specific to the type of biological tissue: $a^{'}$ is a scaling factor calibrated for $\lambda = 500\,\mathrm{nm}$, f_{Ray} is the fraction of Rayleigh to Mie scattering, and b_{Mie} is called the scattering power. Given that b_{Mie} has a positive value for all types of tissue, the scattering dependency on wavelength follows a negative power law, showing that longer wavelengths experience significantly less scattering losses. The absorption coefficient μ_a highly depends on the constituents of the tissue, where major contributions come from

water with broad absorption peaks at 970 nm and 1400 nm and fat, which mainly absorbs around 930 nm, as well as melanin, yellow pigments, and haemoglobin[95, 96]. Figure 2.18 shows the total attenuation coefficients of skin and oxygenated blood[97]. At shorter

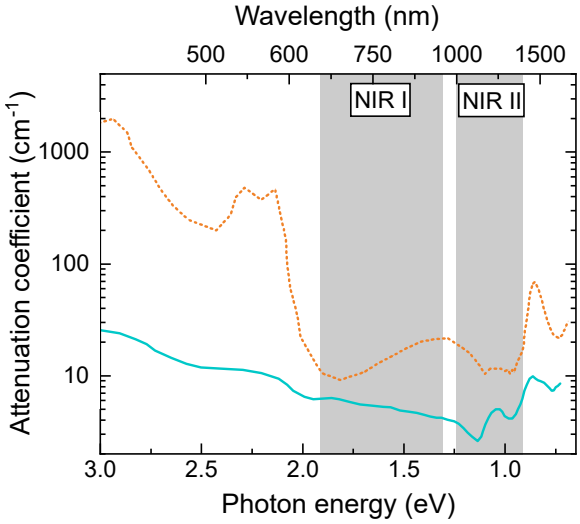

Fig. 2.18. Attenuation coefficient for light in blood (dashed orange line) and in skin (cyan line) as a function of its wavelength (data from [97]). The grey boxes show the NIR I and NIR II therapeutic windows of optimum tissue transparency.

wavelengths, the losses originate predominantly from scattering. The attenuation in blood shows strong absorption from haemoglobin (at 415 nm) in addition to the noticeable water absorption peaks at longer wavelengths[98] which are also dominating the long-wavelength losses in skin[99]. The so-called *therapeutic windows* are wavelength ranges of optimum tissue transparency, which offer most efficient optical interrogation of biological samples due to avoiding the lossiest spectral bands, whilst being compatible with popular imaging techniques and available technology. These two windows are the NIR I[96] (650 nm − 900 nm) and the NIR II[97] (1000 nm − 1350 nm), which are separated by a small gap corresponding to the strong absorption losses from water and fat.

2.2.5 Imaging microlaser emission

Some of the challenges of imaging in biological tissue can be overcome by using micro- and nanolasers as probes. The main advantage is that here the mode position in the spectral domain is used as a label whose value is unaltered by the two main sources of loss in tissue discussed above, i.e. elastic scattering and absorption. While these processes lead to an overall decrease in intensity, the peak position, which contains the relevant information for most applications, remains unaffected. The decrease in intensity

in deep-tissue applications poses a challenge to any method of optical microscopy, but the signal from micro- and nanolasers intrinsically is characterised by high brightness and an excellent signal-to-noise ratio, and can therefore still successfully be measured from greater depths in biological tissue than for example fluorescent images[9, 10].

An additional advantage of integrating nanolasers with microscopy can be an improvement of spatial resolution when operating small nanolasers with pulse energies close to the lasing

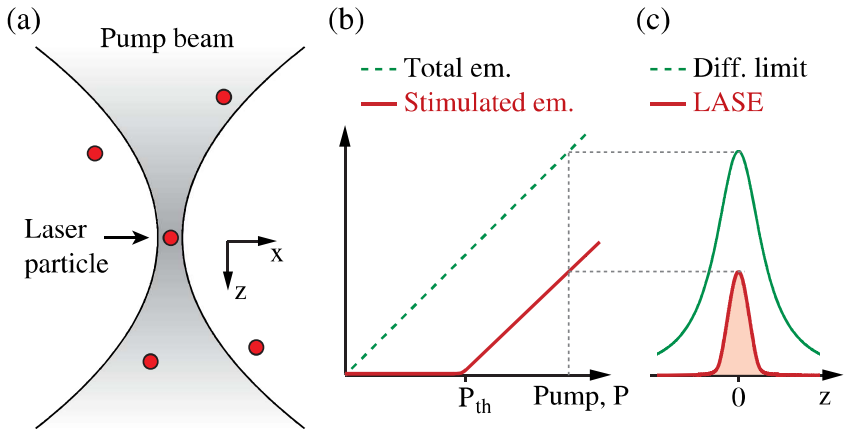

Fig. 2.19. Conceptual visualisation of the resolution enhancement achieved when imaging nanolasers. a, Schematic of nanolasers excited by the pump beam. **b,** Comparison of the pump power dependence of fluorescence and lasing emission and **c,** its effects on the optical sectioning. Reproduced from [27].

threshold. Here, a small nanolaser is understood as having dimensions smaller than the excitation wavelength. Due to the non-linearity of the lasing process, the number of emitted photons declines more rapidly with a decrease in pump power as compared to linear processes like fluorescence (Figure 2.19). This conceptually has some similarities to multi-photon microscopy, but the improvement in resolution here shows a dependence on the dynamics of the lasing process. An improvement factor $\frac{\Delta_{LASE}}{\Delta_0}$ for the resolution enhancement due to the lasing process can be derived starting from Equation 2.23, whose solution takes the approximate form[27]:

$$\frac{\Delta_{LASE}}{\Delta_0} \approx \sqrt{1 - \frac{2}{p+1}\left(1 - \sqrt{\beta}\right)} \qquad (p > 1). \tag{2.36}$$

The quantity $p = \frac{P}{P_{th}}$ is the ratio of pump power to threshold power. Equation 2.36 shows that this resolution enhancement is maximised just above threshold, as well as for nanolasers with a smaller β-factor. At threshold, Equation 2.36 evaluates to $\frac{\Delta_{LASE}}{\Delta_0} \approx \beta^{0.25}$, which corresponds to an enhancement factor of 2-4 for the nanolasers typically

used in this work[1]. The general trends of this enhancement are very intuitive when considering the typical threshold behaviour (Figure 2.9), where one might also expect the greatest enhancement close to the lasing threshold, and in the curves with the steepest inflection. Similar effects are also observed in other non-linear probes such as photon avalanche nanoparticles[100].

Many of the properties of micro - and nanolasers, such as the high brightness and non-linear emission characteristics, therefore prove advantageous for imaging applications. The directionality of the emission from these lasers, however, also poses a challenge for imaging applications. As discussed in Section 2.1.4, depending on the geometry of the laser cavity, the emission often is anisotropic. However, omnidirectional emission is highly advantageous for any integration of microlasers with microscopy such that the emission can be collected efficiently irrespective of the orientation of the microlaser. Consequently, recent works have sought to engineer the cavity geometry of nanodisk lasers to achieve more isotropic emission (see Section 2.1.4). Where more isotropic emission cannot be achieved, it is helpful to increase the solid angle of collection by using a high-NA objective such that a significant fraction of the laser emission can be collected.

2.2.6 Overview of spectroscopic techniques for microlaser readout

As mentioned before, imaging micro- and nanolasers and their spectra brings a unique set of requirements, which often implies that custom-built laser characterisation setups are required to capitalise on the potential of integrating these lasers with practical applications including their use in biological samples. The fundamental approach to this is to use a pump laser, that can either be stationary or scanned, to excite individual microlasers and collect their signal on a sensitive camera such as a CCD camera connected to a high-resolution spectrograph[4, 101]. Different variations of this approach, as well as integrations with other imaging modalities, have been developed to solve the challenge of simultaneously locating microlasers and reading their spectra. In a multi-modal configuration, OCT and fluorescence microscopy were used to localise nanolasers, such that the spectra of the identified nanolasers could then be read on the CCD camera[8, 102]. This approach has proven successful for efficient characterisation of 13 microlasers, however, the throughput of the measurement is limited by the slow readout type of typical CCD cameras, therefore using a faster camera such as a CMOS line-scan camera is preferable for applications analysing a large number of microlasers[2, 7, 103]. Here, the increase in acquisition speed of the individual spectra allows obtaining spectral information of entire

volumes through hyperspectral confocal microscopy. As discussed in Section 2.2.3, CHSI shows excellent spatial and spectral resolution, but can be limited in speed. This was seen in the first demonstration of CHSI for the characterisation of bio-integrated nanolasers, where 731 lasers where characterised, albeit at a scan time of 47 minutes per $z-$stack[7]. The present work addresses this speed limitation by implementing faster spectral detection as well as free-space optics offering greater flexibility[2].

Other efforts for faster imaging of micro- and nanolasers are based on implementing the aforementioned higher-throughput methods of hyperspectral imaging. One of these demonstrations uses pushbroom HSI for microlaser readout, an approach called Diffuse Spectral Localisation Imaging (DSLI)[10]. The main drawback of this method is the missing sectioning capability, which imposes the need for spatially and spectrally deconvolving the measured spectra. This deconvolution, which relies on well-understood scattering properties of the sample, was only achieved for 5 microlasers so far. More recently, snapshot hyperspectral imaging of microlasers was demonstrated in the form of integral field mapping, which entails using a microlens array to map the features of interest onto an area-scan detector with spectral and spatial encoding[94]. While this approach offers excellent throughput for 3-dimensional imaging, the trade-off between spectral and spatial resolution quickly became limiting, and further work is required to address imaging artefacts that pose a challenge for the reliability of this approach.

Lastly, high-speed characterisation of microlasers has been realised in microfluidics[103, 104], which can be an attractive high-throughput approach for applications where spatial information is not needed, particularly when using high-speed cameras.

3 Application-oriented optimisation of III-IV semiconductor materials

Results discussed in this chapter were published as part of the following publication: Titze, V. M., Caixeiro, S., Di Falco, A., Schubert, M. & Gather, M. C. Red-Shifted Excitation and Two-Photon Pumping of Biointegrated GaInP/AlGaInP Quantum Well Microlasers. *ACS Photonics* **9**, 952–960 (2022)[1]. The content of the following sections therefore contains data and results also presented in the aforementioned publication.

Integrating micro- and nanolasers with high-throughput biological applications imposes a range of requirements on the optical properties of such lasers. Semiconductor nanodisk lasers are attractive due to their high photostability and small device footprint[17], but the QW structure used in the aforementioned work was further optimised here with two main goals: i) Allowing straightforward integration with high-throughput laser characterisation measurements, particularly with CHSI, and ii) realising full operation of nanolasers in the therapeutic windows to pave the way for more extensive samples through better depth penetration and more efficient imaging.

One approach to achieve this is band gap engineering, reducing the band gap of the GaInP/AlGaInP QW structure, which (in its original composition) provides emission in the red part of the visible spectrum[105], to allow far-red emission and red excitation (Section 3.1). As it can be seen in Figure 2.18, the attenuation of light in tissue rapidly drops off around 600 nm, therefore excitation with longer wavelengths is preferable. While the absorption wavelength could in principle be tuned on a continuous scale, the actual implementation of longer-wavelength excitation also largely depends on the availability of suitable laser diodes for pumping. Ideally, micro- and nanolasers are excited with short ((sub-)ns) pulses at a high repetition rate, allowing to collect spectra with good contrast despite short pixel dwell times in CHSI. The availability of cost-efficient high-repetition rate laser diodes of course depends on the availability of suitable gain materials, and between blue nitride-based and red phosphide-based laser diodes lies the *green gap*, a spectral window from ca. 520 nm to 620 nm, in which it remains challenging to find materials with suitable emission[106, 107]. Consequently, the goal of the material optimisation here was to allow optical pumping of nanolasers with wavelengths $\geq$ 642 nm to

ensure compatibility with commercially available red laser diodes, particularly the device present in our lab, and to realise excitation in the first therapeutic window.

Additionally, two-photon excitation of nanolasers was investigated (Section 3.2), which is attractive for two reasons: Firstly, this allows the nanolaser measurements to benefit from similar advantages as multi-photon microscopy, i.e. improved tissue transparency due to excitation in the NIR II window, intrinsic optical sectioning, and low out-of-plane photodamage (compare Sections 2.2.2 and 2.2.4). Secondly, two-photon excitation of nanolasers is a promising technique for integrating nanolaser measurements with commercial imaging technology, given that commercial multi-photon microscopes typically include powerful pulsed lasers that are needed for achieving population inversion in nanolasers. The last section of this chapter discusses the suitability of devices from the optimised materials for integration with biological samples, particularly cell culture models (Section 3.3). This includes confirming that the devices do not compromise the viability of the biological samples, but also investigating the performance of the nanolasers under realistic experimental conditions.

3.1 Band gap engineering of quantum well layers

The material used in this work for nanolaser fabrication consists of a ca. 50 nm wide multi-quantum well structure (active layers, Figure 3.1) that is symmetrically surrounded by a 58 nm wide cladding and a 10 nm wide buffer layer on each side. All layers are AlGaInP alloys, albeit of different compositions. As discussed in Section 2.1.1, the optical properties can be tuned by adjusting the material composition and width of the active layers[34]. Specifically, the desired decrease in band gap and corresponding increase in the emission wavelength can be achieved by increasing the width of the QW layers and by reducing the fraction of Gallium in the GaInP alloy (compare calculations shown in Figure 2.5). Therefore, new material compositions were chosen to test the effect of varying width and composition of the QW layers on the device performance.

Three quantities were varied during this optimisation: i) the width of the quantum well L_z, ii) the molar fraction x_1 of Gallium in the $Ga_{x_1}In_{1-x_1}P$ quantum wells, and iii) the molar fraction x_2 of Aluminium in the $Al_{x_2}Ga_{0.51-x_2}In_{0.49}P$ barriers. As a starting point, the material used in previous work[17], here called *Wafer A*, was used, and three new materials were designed (*Wafers B-D*). A summary of the specifications of all four wafer materials can be found in Table 3.1. Although a separate investigation of all parameters

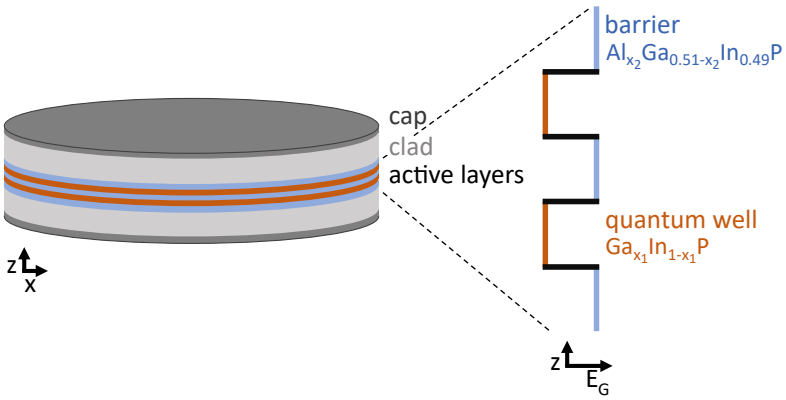

Fig. 3.1. Schematic showing the layers of the structure of the nanolaser material. The active layers consist of two GaInP QW layers (orange) and three AlGaInP barriers (blue), whose molar fractions x_1 and x_2 are varied in this study. On the right side, a sketch of the 1D band structure of active layers is shown. The active layers are surrounded by cladding (light grey, clad) and buffer (dark grey, cap) layers.

would have benefited from comparing wafers with all possible combinations of these parameters, this was not feasible given that the wafers were epitaxially grown at the EPSRC National Epitaxy Facility, University of Sheffield, which required careful optimisation of the growth parameters for each new composition. Therefore, the three most promising materials for stable red emission were chosen. A decrease in Gallium concentration leads to a higher strain ϵ due to the greater mismatch with the lattice constant of the GaAs substrate on which the structure is grown. Due to the risk of forming dislocations with greater strain[35], the Gallium concentration could not be reduced arbitrarily. Rather, the furthest-red emitting wafer (Wafer D) was based on the lowest Gallium concentration ($x_1 = 0.37$) demonstrated successfully so far[36], and the two other wafers (B, C) were chosen to have an intermediate QW Gallium concentration between Wafers A and D. An increase in well width was considered as a comparably reliable option for reducing the band gap, and was adjusted from 7 nm to 10 nm for all new structures. In addition to the modifications to the QW layers, the concentration of Aluminium in the barrier was reduced in Wafer C to lower the band gap of the barrier[108, 109] and increase long-wavelength absorption.

	A	B	C	D
L_z (nm)	7	10	10	10
x_1	0.41	0.39	0.39	0.37
x_2	0.255	0.255	0.204	0.255
ϵ (%)	0.77	0.92	0.92	1.1

Table 3.1. Wafer parameters varied during this study.

First, the general decrease in band gap resulting from the material adjustments was verified by comparing photoluminescence (PL) spectra of the structures prior to fabricating nanolasers from the wafers (Figure 3.2). Fitting the Gaussian-like part of each spectrum centred around each peak to a Gaussian function allowed to extract the maximum PL wavelength, which was 664 nm (A), 691 nm (B), 692 nm (C), and 697 nm (D). The expected trend of red-shift with decreasing Gallium concentration and increasing well width could therefore be confirmed. Further, Wafers B and C, having identical QW specifications, show very similar PL spectra despite the different barrier compositions, which is expected given that the emission is primarily governed by the QW[34].

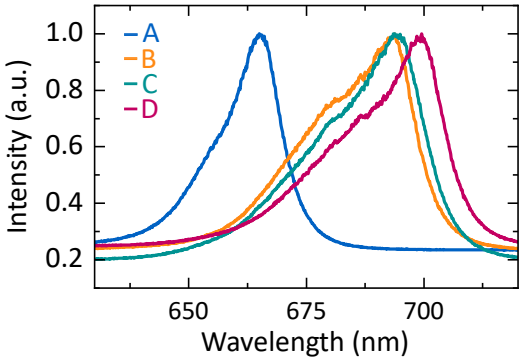

Fig. 3.2. PL spectra of all four wafers investigated, confirming the expected red-shift of the newly designed wafers B-D.

Next, the emission properties of the fabricated nanolasers were investigated by imaging batches of devices with CHSI. A 532 nm pump laser, that is expected to efficiently excite all structures, was used for high-throughput collection of spectra from approximately 150 nanolasers from each wafer (Figure 3.3). The devices were $1.6 - 1.8\,\mu m$ in diameter and showed predominantly single-mode emission. Per Equation 2.10, the lasing peak is found at a position where a cavity mode coincides with large material gain. The position of the cavity mode of the disk-shaped resonators, which depends on the disk diameter and the internal and external refractive indices (Equation 2.27), will be found at a different positions for each resonator in a batch due to natural variation in size resulting from the fabrication process. Additionally, although in the size range used for this measurement, the FSR is smaller than the width of the gain spectrum, only one mode was typically observed in the lasing spectrum due to gain competition. Consequently, a histogram of a large number of lasing peaks should have an envelope function representing the gain spectrum. Despite the experimentally measured histograms still showing some fluctuation, presumably due to too low sample statistics, the central wavelengths of the distributions were approximated as the mean of a Gaussian distribution. It can already be seen in Figure

3.3 that the gain spectrum is shifted along with the PL spectrum and consistently peaks on the long-wavelength shoulder of the PL spectrum, presumably due to reabsorption losses at shorter wavelengths. The difference between the peaks of the PL and the gain spectra is lowest for Wafer B (9 nm) and greatest for Wafer C (14 nm), and the shifts of Wafers A and D are 12 nm. Interestingly, with the exemption of Wafer D, the magnitude of this difference scales inversely with the depth of the QW, i.e. the difference in band gap between QW and barrier layers. This could be due to reduced electron confinement, meaning that in shallower wells high-energy electrons are less well confined to the QW, and due to re-absorption, in which case long-wavelength absorption is enabled by the lower band gap of the barrier.

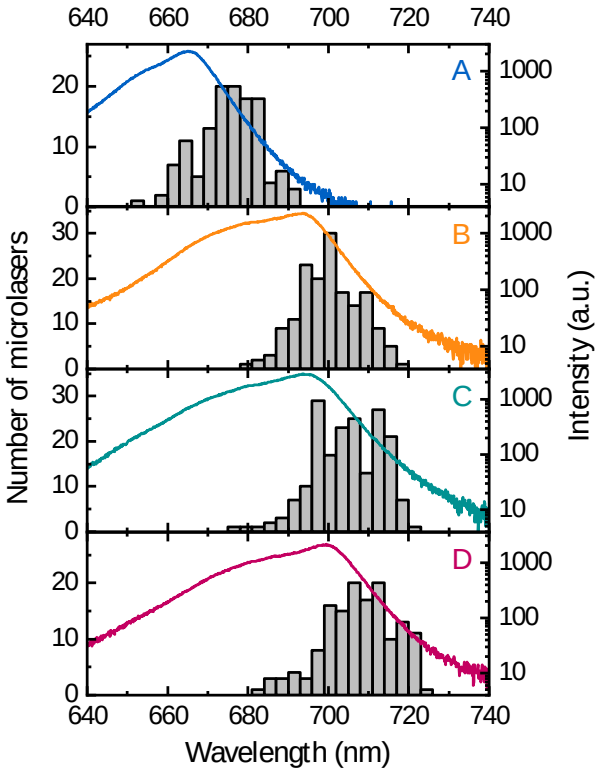

Fig. 3.3. Material-dependent distribution of lasing peaks. Histograms representing the distribution of lasing peaks for devices from each wafer (grey, left axis) with superimposed PL spectra (right axis), colour-coded as in Figure 3.2.

To gain a complete understanding of the spectral dependence of the lasing process, the effectiveness of pumping at different wavelengths was studied next. For this, $n \geq 2$ microlasers from each wafer were subject to pumping with a tuneable OPO set to different wavelengths between 480 nm and 660 nm, recording threshold curves at each wavelength. To avoid damage to the devices, which would have reduced the comparability between

subsequent measurements, each measurement was stopped before reaching the saturation regime, therefore the classic S-shaped threshold curves (compare Section 2.1.4) were not obtained here, and the experimental data was therefore fitted with two linear functions whose intersection was taken as the lasing threshold (Figure A.1). These measurements were performed over a broad range of wavelengths in steps of 20 nm, and at each point, the value of the threshold was extracted (Figure 3.4a). To investigate relative rather than absolute trends in the absorption, the curves in Figure 3.4a were normalised with respect to the average threshold of each wafer taken over the range 480 nm to 620 nm, i.e. the range where all structures could be excited efficiently. In this range, the four materials

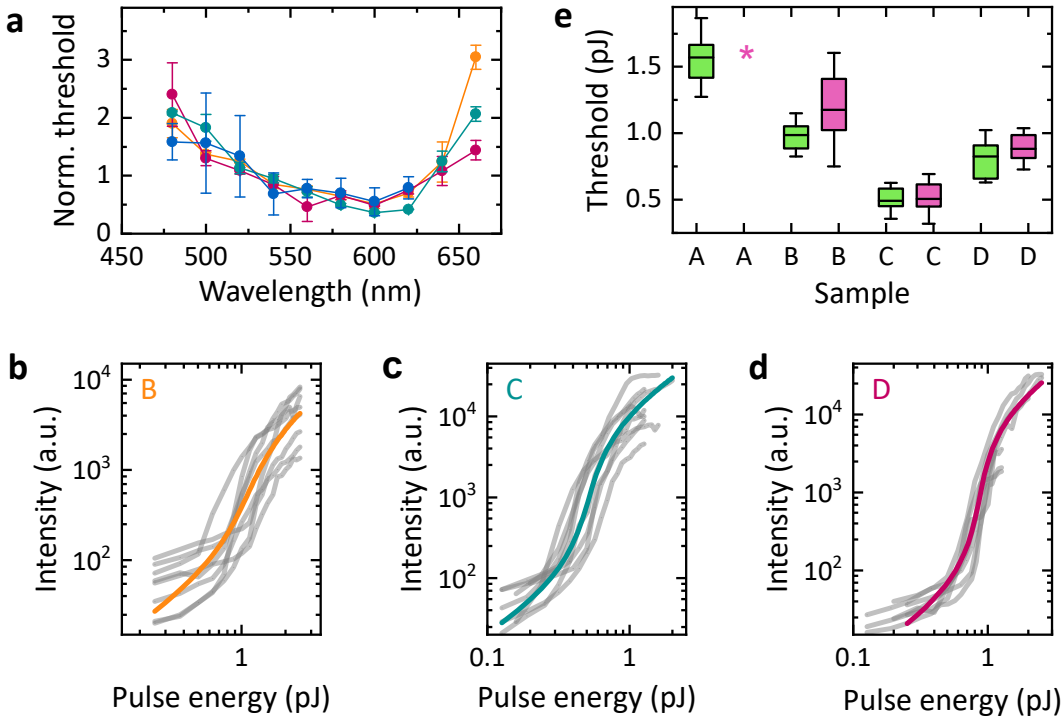

Fig. 3.4. Spectral dependence of lasing thresholds. a, Normalised threshold curves of $n \geq 2$ nanolasers from each wafer excited with a tuneable laser over a broad spectral range, colour-coded according to previous figures. **b-d,** Thresholds of $n \geq 6$ nanolasers from wafers B-C at 642 nm pumping, whose average thresholds are summarised in **e,** along with analogous results for 532 nm pumping. The threshold statistics show the mean (centre line), the 25-75 percentile (box) and 1.5 standard deviations (whiskers), while the asterisk marks the sample with no detectable lasing.

showed a very similar pattern, with the minimal lasing threshold around 600 nm. Above 620 nm, nanolasers from Wafer A could not reliably be excited above the lasing threshold. Wafers B and C both showed lasing over all wavelengths tested, but the threshold of Wafer B increased more steeply above 640 nm than that of Wafer C despite the identical QW composition and similar PL spectra of the two materials. This is further evidence for the

increase in long-wavelength absorption in Wafer C. Lastly, the lasing thresholds of Wafer D showed the best performance at 640 nm and 660 nm pumping, which is not surprising given that this structure has the smallest band gap. Detailed methods for the optical characterisation for these experiments are provided in Appendix A.1.

Next, these trends were confirmed for pumping nanolasers with the two high-repetition rate diode lasers (532 nm @ 125 kHz, 642 nm @ 10 MHz) that are relevant for integration with CHSI. For each wavelength, $n \geq 6$ devices from each material were randomly selected, a threshold curve was measured and fitted according to Equation 2.23, and the threshold energy was calculated using Equation 2.24. This allowed to compile statistics of how the threshold values compare between the two excitation wavelengths used (Figure 3.4). A summary of all average threshold values and their standard deviations for the two

threshold - pump source	Wafer A	Wafer B	Wafer C	Wafer D
F_{th} (µJcm^{-2}) - 530 nm OPO	57.8 ± 30.4	67.1 ± 3.6	34.8 ± 2.8	18.7 ± 1.9
F_{th} (µJcm^{-2}) - 640 nm OPO	-	79.2 ± 22.1	41.6 ± 6.0	20.9 ± 4.9
E_{th} (pJ) - 530 nm OPO	1.45 ± 0.76	1.68 ± 0.09	0.87 ± 0.07	0.47 ± 0.05
E_{th} (pJ) - 640 nm OPO	-	1.98 ± 0.55	1.04 ± 0.15	0.52 ± 0.12
E_{th} (pJ) - 532 nm DL	1.60 ± 0.19	0.99 ± 0.11	0.49 ± 0.09	0.83 ± 0.13
E_{th} (pJ) - 642 nm DL	-	1.18 ± 0.28	0.51 ± 0.13	0.88 ± 0.10
$\frac{E_{th}^R}{E_{th}^G}$ OPO	-	1.18	1.20	1.12
$\frac{E_{th}^R}{E_{th}^G}$ DL	-	1.19	1.04	1.06

Table 3.2. Comparison of green and red excitation of nanolasers from measurements with OPO and diode lasers (DL).

measurements is given in Table 3.2, where the 530 nm value for the OPO measurement was calculated by linearly interpolating the values from 520 nm and 540 nm. Experiment 1 (OPO excitation) and experiment 2 (DL excitation) did not only differ in terms of pump repetition rate, but also used different geometries for excitation: In experiment 1, a collimated beam was used and the thresholds were first calculated in terms of pump fluence in µJcm^{-2}, and for comparison, the average area of the nanolaser surface was estimated to be 2.5 µm^2 to calculate the energy incident on the resonator. In experiment 2, a focused beam was used (representative of the excitation in CHSI), which has a spot size smaller than the area of the resonator. Therefore it was assumed that the entire pulse energy was incident on the resonator, albeit distributed less evenly. Lastly, two different batches of nanolaser were used between the two experiments. Despite these differences, the obtained thresholds are overall in very good agreement, showing that devices from Wafers C and

D show the lowest thresholds overall, while the threshold of Wafer B increased the most between green and red excitation. In neither experiment, Wafer A could be excited in the red. Due to the poor beam quality of the OPO at > 620 nm, and due to the larger sample size in the second measurement and the higher-quality threshold curves which could be fitted with the proper rate equation model, experiment 2 is presumably more indicative of the performance of the materials.

In summary, the engineering modifications to the wafer structures were successful in shifting excitation and emission of QW nanolasers to longer wavelengths. All new structures could successfully be pumped with the 642 nm diode laser, which is attractive for integration with CHSI; and particularly low thresholds under red pumping were obtained with Wafer C owing to the improved barrier absorption, and with Wafer D due to the overall smaller band gap. The long-wavelength absorption behaviour in Wafer C also had the consequence of shifting the lasing gain spectra to even longer wavelengths as compared to the PL spectrum due to losses from reabsorption. Some batch-to-batch variation was observed, which could be an indication of a variation of optical properties across the individual wafers. Indeed, especially in Wafer D, a colour-change from the centre of the wafer to the edges was noted upon visual inspection of the wafer, which might be related to the high strain of this material making it prone to defects. Lastly, the reproducibility of these results are also subject to the reliability of the epitaxial growth, which was not part of this work. Wafers B-D were grown during subsequent runs that were part of the same optimisation project and were therefore assumed to be consistent within this project, but between nominally the same wafers from different epitaxy runs, a substantial change in optical properties was noted, e.g. the PL peak from Wafer A in this work (664 nm) and previous work (675 nm)[17].

3.2 Two-photon excitation of semiconductor nanolasers

The second approach for high-throughput excitation of nanolasers in deep tissue is multi-photon excitation. Given that the previous section showed that nanolasers can be optimally excited between 540 nm and 600 nm, the optimum for two-photon absorption is expected at approximately double the wavelength, which coincides with the NIR II window, where suitable pump lasers are frequently implemented in commercial systems for multi-photon excitation of popular visible-wavelength dyes. Using a 1030 nm laser with a short pulse width of 250 fs, the two-photon excitation behaviour was investigated

by measuring threshold curves of nanolasers from the two wafers with the most efficient single-photon excited lasing, Wafers C and D.

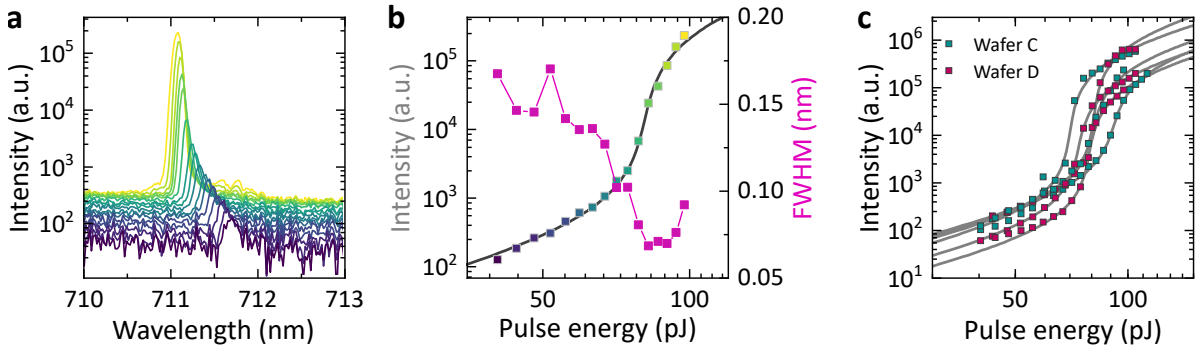

Fig. 3.5. Threshold curves under two-photon excitation. **a,** Measured spectra from a nanolaser under two-photon excitation with pulses of increasing energy (blue to yellow). **b,** Corresponding input-output curve (blue-yellow colours matching the spectra from **a**, which was fitted according to the adjusted rate equation model, and linewidths showing characteristic narrowing (magenta). **c,** All threshold curves measured of devices fabricated from Wafer C (cyan) and Wafer D (magenta).

Typical spectra of a representative device with increasing pulse energy, and a corresponding input-output curve are shown in Figure 3.5a and b, respectively. These results were repeatable for multiple devices tested from both wafers (Figure 3.5c) with average lasing thresholds of 81 ± 11 pJ (Wafer C) and 78 ± 4 pJ (Wafer D) obtained by fitting an adjusted rate equation model. This adjusted model is based on the assumption from Equation 2.34 that the rate of excitation quadratically depends on the excitation power. Given that all other terms in Equation 2.34, i.e. the pump parameters (wavelength and pulse duration) and the optical setup (pump spot and collection optics) were kept unchanged during the measurement, a simple effective excitation cross section α was defined to represent all the constant terms, such that the rate of pumping R_P to the pulse energy E could be expressed as

$$R_P = \alpha E^2. \tag{3.1}$$

The pump power in the regular threshold Equation 2.23 was substituted by this pump rate, which allowed capturing the curve shape noticeably better than with the model without the substitution. From obtaining the threshold pump rate using Equation 2.24, the threshold pump energy could be calculated, such that

$$E_{th} = \sqrt{\frac{T}{\alpha\beta}}. \tag{3.2}$$

The shape of threshold curves under one- and two-photon excitation was very comparable

in its dependence on the pump rate, which could be shown by normalising the threshold curves by their threshold pump rate and output (Figure 3.6a).

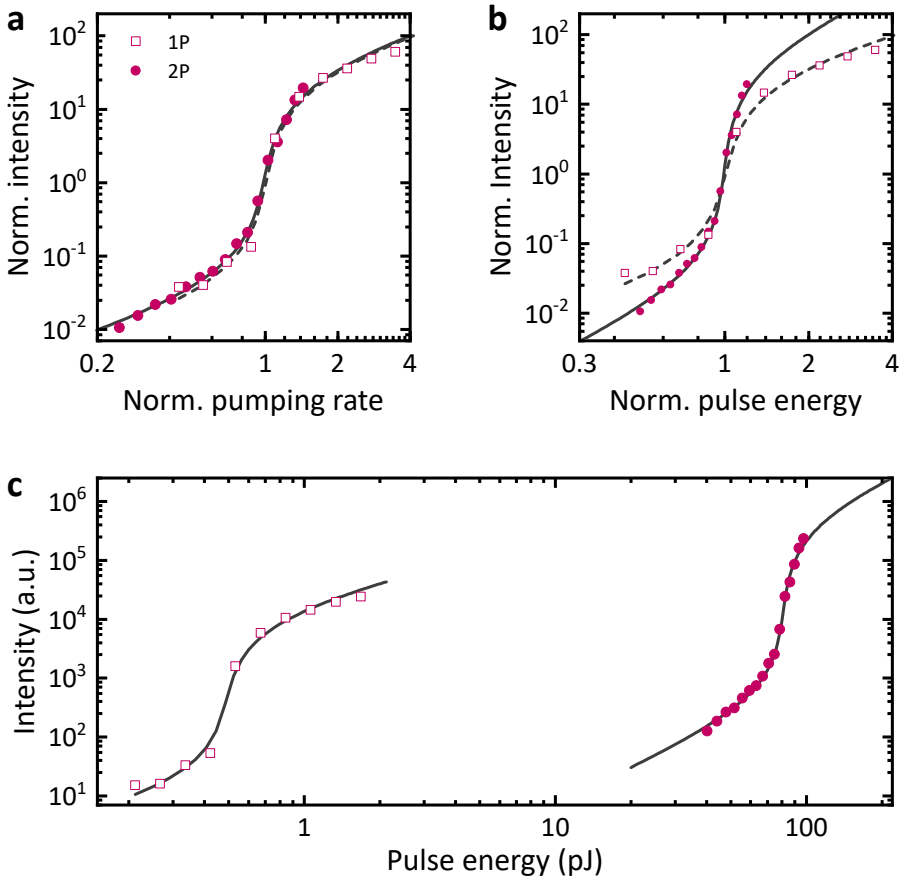

Fig. 3.6. Comparison of one- and two-photon excitation. a, Input-output curves that were plotted and normalised with respect to the threshold pump rate and **b,** according to pulse energy, showing measured data for single-photon (magenta boxes) and two-photon excitation (filled circles), with corresponding rate equation fit to the standard model for one-photon (dashed line) and to the adjusted rate equation model for two-photon excitation (solid line). **c,** Threshold curves for one- and two-photon pumping without normalisation.

This suggests that the lasing dynamics caused by the radiative decay of excited states are independent of the excitation pathway. Plotting and normalising the threshold curves according to pulse energy rather than pump rate reveals that the two-photon excited curve shows a greater slope and more pronounced step at threshold, which is a consequence of the additional non-linearity in the pumping process (Figure 3.6b). A relevant consequence of this increased nonlinearity pertains to the imaging of nanolasers. The observed behaviour suggests that when using two-photon excitation of nanolasers, the improved sectioning

of fluorescence multi-photon imaging and the resolution enhancement of imaging non-linear particles such as nanolasers close to threshold should combine for an even greater improvement in axial resolution.

Lastly, these results allow comparing the absolute threshold energies between one- and two-photon excitation, where an increase by a factor of ∼100 was measured between the sub-pJ thresholds under one-photon excitation and the two-photon excitation around 80 pJ. Few works directly compare single- and two-photon excitation of nanolasers, but among those, a substantial increase in threshold was observed universally[110–112]. This could stem from the reduced absorption cross section, analogous to two-photon excitation of fluorophores[88, 89]. Nevertheless, the measured thresholds for two-photon excitation of the QW nanodisk lasers, which are consistently < 100 pJ, are well within the reach of commercial multi-photon systems, easing the integration with this technology (Section 4.2). Crucially, the expected average power needed to pump nanolasers at 80 MHz repetition rate is considered safe for long-term imaging of biological samples, where the reported damage thresholds of ~ 10 mW[90, 113, 114] would allow excitation of ≤ 125 pJ.

A first indication of the compatibility with commercial multi-photon microscopes was obtained by lifetime analysis of the lasing process through two-photon excited fluorescent lifetime imaging (FLIM). This approach was chosen as a first test whether any changes in lifetime around the expected threshold would indicate the onset of the lasing threshold prior to integrating spectral detection with the commercial microscope. For this measurement, a FOV with three nanodisk lasers was analysed by FLIM at a range of pulse energies ranging from 0.1 % to 1.5 % of the excitation laser power. Based on the equipment specifications and a rough estimation of the efficiency of the system, it was estimated that the 1 % power setting corresponds to a pulse energy of around 10^2 pJ, and the lasing threshold was expected somewhere between 0.5 % to 1 %. Figure 3.7 shows the measurements at 0.2 % (a,d), 0.5 % (b,e), and 1 % (c,f). FLIM data, which is obtained by point-scanning, obtains a spatial map of lifetime data (top panels). At each pixel, the arrival times of emitted photons are recorded and this lifetime data can be analysed using phasor plots (bottom). Each pixel in the spatial image is mapped to the phasor plot; a polar graph of the phase ϕ and the modulation M of the measured signal. These parameters are extracted from a mathematical description of the combined emission of multiple fluorophores showing exponential decay independent from each other[115]. This analysis allows to introduce a unit circle (thin grey line, Figure 3.7 d-f) on which populations characterised by a mono-exponential decay are located with lifetimes increasing along the circle from the right to the left corner. Bi-exponential decay is located within

the unit circle on a line connecting the two contributions, with the positioning along this line reflecting the relative fractions of each contribution[116]. On the outside of the unit circle lay lifetimes with a delay relative to excitation pulse, which is observed for excited-state reactions such as acceptor-emission in Förster resonance energy transfer (FRET), monomer-eximer kinetics, or dipolar relaxation[117].

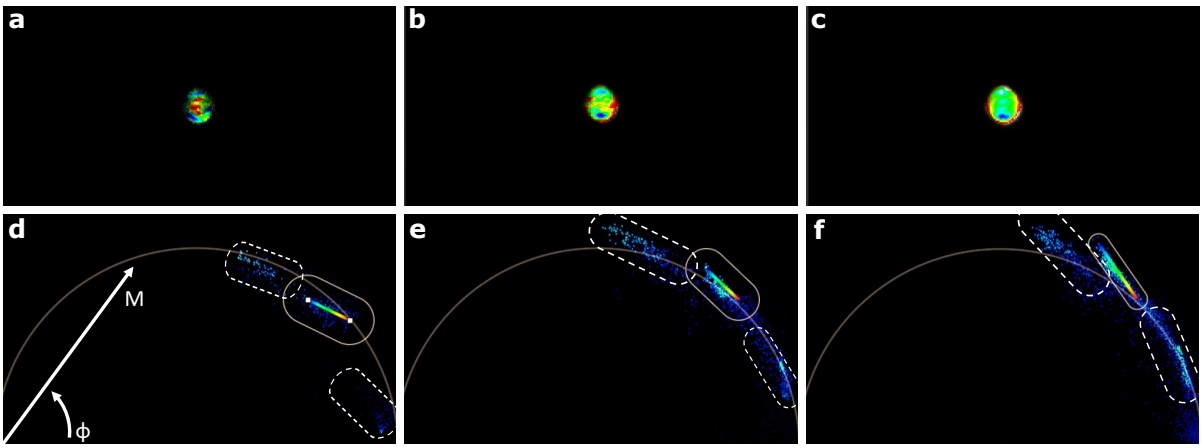

Fig. 3.7. Fluorescence lifetime analysis of lasing process. a-c, FLIM images of a nanodisk laser excited with increasing pulse energy by adjusting the power setting of the pump laser (0.2 % (a), 0.5 % (b), and 1 % (c) of the available power). There were 3 nanolasers present in the FOV of the measurement, but the images in the top row were cropped to magnify just one device. **d-f,** FLIM phasor plots again with pulse energies of 0.2 % (d), 0.5 % (e), and 1 % (f), showing FLIM data for 3 devices as indicated by the rounded boxes. The lifetime data from the nanodisk laser shown in the top panels lays predominantly within the solid-line rounded box of each bottom panel, and the colour-coding of the spatial pixels in the top row matches the coloured line imposed on the lifetime distribution in the corresponding panel in the bottom row. See Figure A.2 for an annotated version. This data was acquired in collaboration with Jens-Peter Gabriel from Leica Microsystems.

Here, with increasing pulse energy, a shift of the population from the inside to the outside of the unit circle is noticed. This trend is observed for all 3 nanolasers present in the FOV of the measurement, whose lifetimes are seen as three distinct populations in the phasor plots (3.7d-f). Below the expected threshold energy, a bi-exponential decay can be seen, which has a slow component at a similar position for the three devices, and a fast component with starkly different values for each nanolaser (3.7d). This was estimated by finding two points on the unit circle for each population such that the line connecting the two points contains the measured lifetime data (Figure A.2). Intuitively, the constant lifetime corresponds to the excited state lifetime in the quantum wells, and the variable lifetime to the cavity lifetime, which could differ for example due to different resonator

geometries that are to be expected during the fabrication process. The spatial distribution of the lifetimes was further investigated for one of the three nanolasers by colour-coding the pixels in the image (top row) by lifetime with a custom colour-coding corresponding to the line drawn in the phasor plots through the lifetime distribution associated with this nanolaser (bottom row). At low pump energies, the positions of faster (red) and slower (blue) components are distributed randomly across the nanodisk (3.7a,d). Above the lasing threshold, the emission dominated by the fast cavity lifetime is clearly located along the circumference of the resonator, where the WGMs are located (3.7c). Moving from the edge to the centre, the lifetimes shift outward of the unit circle (3.7f), which is observed for all lasers in the FOV. The disappearance of the spontaneous emission contribution suggests that pumping the middle of the resonator still leads to lasing, albeit with a delay in onset as compared to the edge where the WGMs are pumped more efficiently. This is consistent with observations of the dynamics of electrically driven quantum well lasers, where a delay of the lasing onset was described that vanishes with increasing pump power[118, 119]. Lastly, when comparing the three nanolasers present in these images, there appears to be an inverse correlation between the cavity lifetime and the onset of lasing as seen by the outward shift in the phasor plot, which is consistent with the theoretical model of the threshold process (Section 2.1.4): A shorter cavity lifetime means a larger cavity decay rate, which according to Equation 2.24 leads to a higher lasing threshold.

In this measurement, a clear transition in the measured lifetimes and their spatial distribution around the expected two-photon excited lasing threshold was observed, that suggests the onset of lasing. This not only confirmed the feasibility of integrating nanolasers with commercial multi-photon microscopes, but also provided interesting insights into the lifetime dynamics of the optically-pumped nanolasers.

3.3 Performance in cell culture conditions

Due to their small size, low lasing thresholds, and long-wavelength operation, semiconductor nanolasers provide many advantages for biological applications including cell tracking and intracellular sensing. One challenge arises due to the toxicity of many semiconductor materials, which often requires encapsulation of the devices to avoid compromising cellular viability[67]. This encapsulation additionally stabilises the wavelength, which improves the reliability of the label for cell tracking, but limits the sensitivity to external refractive index changes. Refractive index sensing utilises the evanescent component of the electric

field, which decays exponentially outside the resonator, leading to a rapid reduction of sensitivity with increasing distance between analyte and resonator (compare also Section redacted). Particularly for sensing applications, an attractive alternative to the encapsulation therefore is to use arsenic-free semiconductor alloys to avoid acute toxic effects[120]. Nanolasers from the AlInGaP/InGaP QW material indeed did not compromise cell viability as confirmed by a 4-day viability assay[17], and subsequently have allowed long-term intracellular sensing measurements[121].

Viability assay

To confirm that the material adjustments in this study did not lead to toxic effects in cell culture settings, a 5-day viability assay was performed. Two controls (HEK293 cells) and two samples (HEK293 cells with nanolasers) were prepared such that the cell viability could be evaluated after 3 and 5 days by fixing one sample of each type after the designated time and performing a live-dead-stain (Figure 3.8a, see Appendix A.1 for methods). By selective staining of live and dead cells, the two groups were easily identifiable by fluorescence imaging, which allowed counting the populations in various FOVs to obtain the viability statistics shown in Figure 3.8b. After 3 days, two samples were fixed for

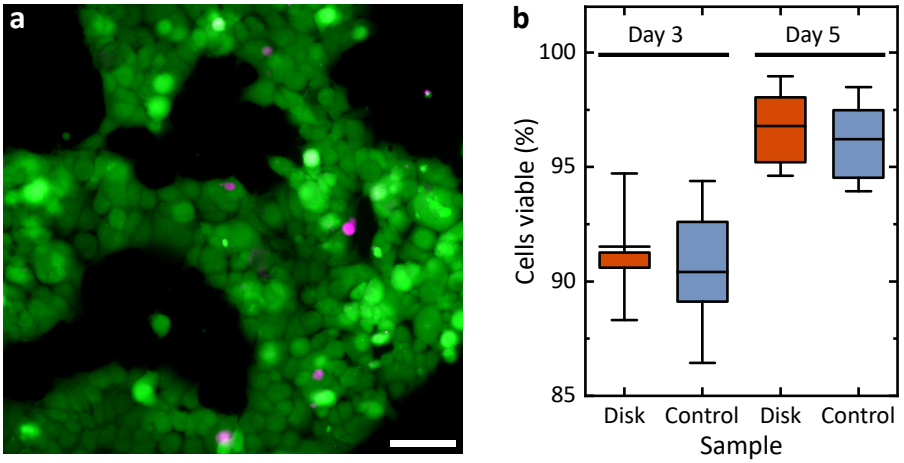

Fig. 3.8. Viability assay with nanodisk lasers. a, Fluorescence image of the fixed cell culture to assess viability by selective staining of live cells (green) and dead cells (magenta). **b,** Cell viability of cells with nanodisk lasers (orange) and the control group (blue) after 3 and 5 days. Shown here are the mean (centre line), 25–75 percentile (box) and 1.5 times the standard deviation (whiskers) of the distribution.

analysis, and a medium change was performed on the remaining two samples. The viability between the nanolaser and control sample showed no significant difference on either

day, but the viability was overall higher on day 5. This suggests that, as expected, the nanolasers do not compromise viability. The medium change of the day 5 samples on day 3 likely removed dead cells in the cultures, therefore the dead cells in the day 5 sample represent the fraction of cells that died between day 3 and 5. The higher viability in the day 5 sample suggests that most cells died in the beginning, likely during the process of splitting and reseeding the cells, irrespective of the presence of nanolasers.

Optical measurements in aqueous environments

Lastly, the performance of nanolasers and their stability of lasing emission was investigated in aqueous environments due to the interest in using nanolasers in cell culture applications. First, lasing thresholds from Wafer D measured in DIW were found to be 0.90 ± 0.12 pJ (Figure A.3), showing no significant difference to the 0.88 ± 0.10 pJ measured in air. The high-refractive index semiconductor material ($n \approx 3.55$) provides excellent refractive index contrast with both air and water ($n = 1.33$), such that the relatively small change in refractive index between the two media does not reduce the optical confinement significantly, therefore the Q-factor and consequently the lasing thresholds were also expected to be comparable.

Next, the short-term stability of the optical properties was investigated under continuous pumping at 2.55 pJ ($2 - 3\times$ above the usual lasing threshold, although no threshold measurement was performed for this particular batch), and with a pulse repetition rate of 1 kHz (Figure 3.9).

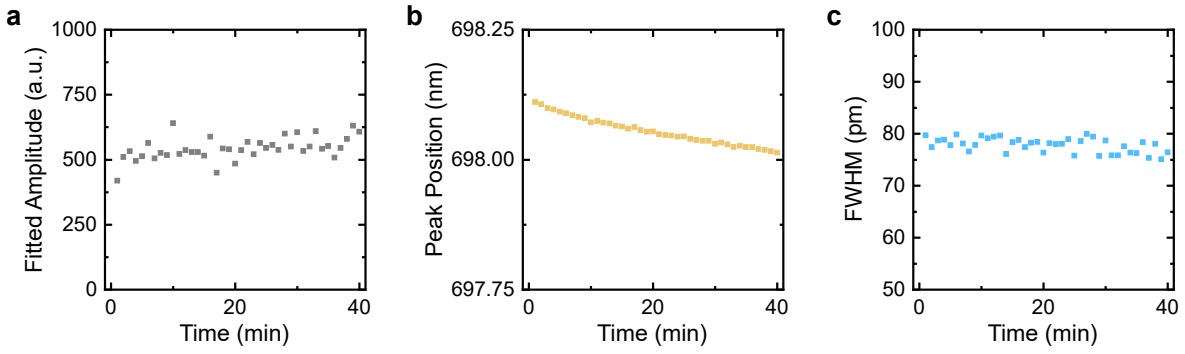

Fig. 3.9. Stability of nanodisk laser emission under continuous pumping. a, Amplitude, **b,** peak position, and **c,** FWHM of the lasing peak. The parameters were extracted from continuously acquiring lasing spectra of a representative nanolaser and fitting each spectrum with a Gaussian.

For sustained biological experiments, stable operation of nanolasers is very important, which entails both the ability of the laser to produce a high-quality lasing peak, as indicated by brightness and linewidth of the laser, as well as wavelength stability, which is relevant to tracking and sensing applications. The intensity (3.9a) and the spectral width (FWHM, 3.9c) of the lasing peak remained constant with some fluctuations attributed to instability of the pump laser, but the position of the lasing peak (3.9b) showed a small (ca. 100 pm) blue-shift over the 40 min experiment. Such a shift could be explained by surface degradation leading to an overall decrease in cavity size, and has been successfully addressed by surface passivation in previous work[17]. Further work to stabilise the lasing wavelength should include developing a passivation routine for the new materials and fabrication conditions. Additionally, a high pump power seems to exacerbate the observed shifts, therefore the pump power should be limited to the minimal amount necessary for excitation of lasing modes and high-quality signal collection. This challenge is revisited in the context of CHSI of nanodisk lasers in Section 4.3.

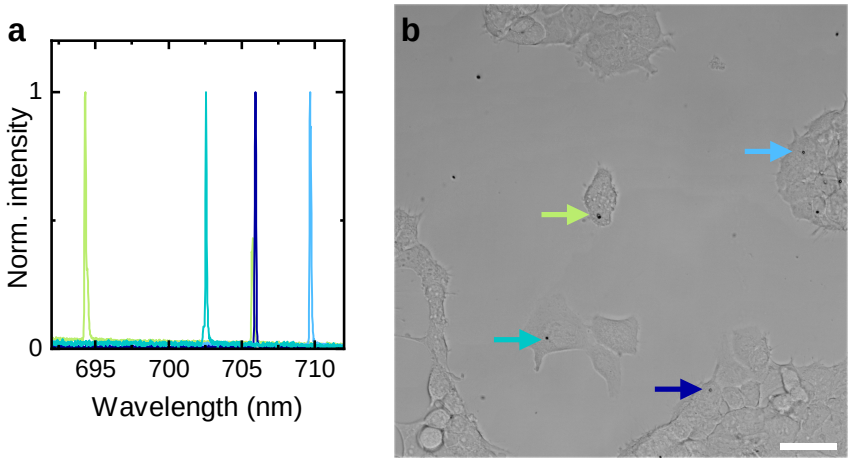

Fig. 3.10. Intracellular lasing with nanodisk lasers. **a,** Normalised exemplary spectra from different nanodisk lasers. **b,** Brightfield image of the cell sample where arrows of matching colour indicate the devices from which the spectra in **a** were taken. Scale bar, 50 µm

Lastly, the long-term stability of the nanolasers was studied. For this, the samples from the viability assay containing nanolasers were imaged on the last day of the assay to obtain intracellular lasing spectra. As indicated by the narrow, bright lasing peaks measured from the devices inside attached cells (Figure 3.10), intracellular lasing measurements are sustainable over the course of multiple days, which has been further confirmed by successful long-term images of cells containing nanolasers in CHSI (Section 5.3).

4 Hyperspectral confocal microscopy for high-throughput microlaser readout

Results discussed in this chapter were published as part of the following publication: Titze, V. M. et al. Hyperspectral Confocal Imaging for High-Throughput Readout and Analysis of Bio-Integrated Microlasers. *Nature Protocols* **19**, 928–959 (2024)[2]. The content of the following sections therefore contains data and results also presented in the aforementioned publication.

Owing to the high information density encoded in the spectra of microscopic lasers, they are extremely well-suited for high-throughput applications including tracking thousands of barcodes[7, 66] and high-throughput intracellular sensing while maintaining single-cell specificity. As discussed in previous sections and demonstrated in previous works[9, 10], this technology also provides many advantages for deep-tissue applications, making this highly attractive for applications in large 3-dimensional biological samples. However, an essential step towards these applications is the construction of an appropriate setup for the readout of the spectra emitted by the microlasers. In addition to a suitable pump laser to excite the microlasers and a high-resolution spectrometer for spectral collection, some form of automated scanning or parallelisation of this readout is required for such high-throughput analysis, which has led to the development of the various custom hyperspectral imaging configurations reviewed in Section 2.2.6. Out of the methods reviewed, CHSI offers the highest combination of spectral and spatial resolution, and has so far enabled the most convincing demonstration of high-throughput measurements by showing long-term tracking of 731 intracellular nanolasers[7]. Therefore, CHSI was also implemented here, but the main drawback of the previous demonstration, which was the slow scan time of 47 min per z-stack, was addressed. A custom-built CHSI setup was developed by automation of scanning and data analysis, which allowed increasing the speed of the spectral acquisition to 125 kHz. The fastest z-stack time here was 58 s for an extended 3-dimensional sample, which was achieved by combining the high-speed detection with a custom confocal scan head constructed with free-space optics. This approach (discussed in Section 4.1) provides great flexibility in the optical engineering of excitation and collection, which is particularly useful for tuning the trade-off of spatial and temporal resolution, leading to additional improvements in measurement speed. While the integration with commercial microscopes does not provide as much flexibility in terms of the optical

implementation, it can be an attractive alternative due to the convenient availability of multi-modal imaging of confocal fluorescence imaging and CHSI. Therefore, this approach was also realised here and is discussed in Section 4.2. After describing these two main implementations of CHSI, the setup performance and the CHSI results for various types of micro- and nanolasers are discussed in Section 4.3.

4.1 Home-built hyperspectral confocal laser scanning setup

In the following sections, the development of the custom-build CHSI setup is described, which includes both the design and construction of the optical setup (Section 4.1.1) and the automation of the data acquisition through custom software solutions for hardware control (Section 4.1.2). Then, the handling and interpretation of the acquired data is discussed, which required developing a custom data processing software[3] and performing calibration measurements that provided reference values for spatial and spectral calibration of the microscope.

4.1.1 Optical setup

The optical setup consists of two main modules: the confocal scan head, and the spectroscopy setup. The confocal scan head (Figure 4.1) is responsible for point-scanning the sample with the pump laser beam (PUMP, green path) and for collecting the lasing signal (magenta path) emitted by the sample at each point. Here, galvo mirrors (GM) are used for the $x-y-$scanning, which deflect the beam by a controlled angle in a plane conjugate to the back aperture of the objective, such that in the conjugate imaging plane (CP), the beam spot is moved. The scan lens (L1) and the tube lens (L2) relay the deflected scanning beam to the back aperture of the objective, such that the objective focuses the scanned spot onto the sample. The objective is mounted on a piezo-electric objective scanner (OS), which moves it along the optical path for scanning in the $z-$direction. The focused beam excites the microlasers in the sample and their lasing emission is collected along the excitation path, i.e. de-scanned, until a dichroic mirror separates the lasing signal from the excitation path. The dichroic mirror, which is housed in a filter cube (FC3), has a dielectric coating which transmits wavelengths below a specific cut-off wavelength, and reflects longer wavelengths, such that the long-wavelength lasing emission is reflected in the collection arm. Here, the signal is coupled into an optical fibre by focusing the light with lens L4 onto the fibre core, which acts as the confocal pinhole to allow optical

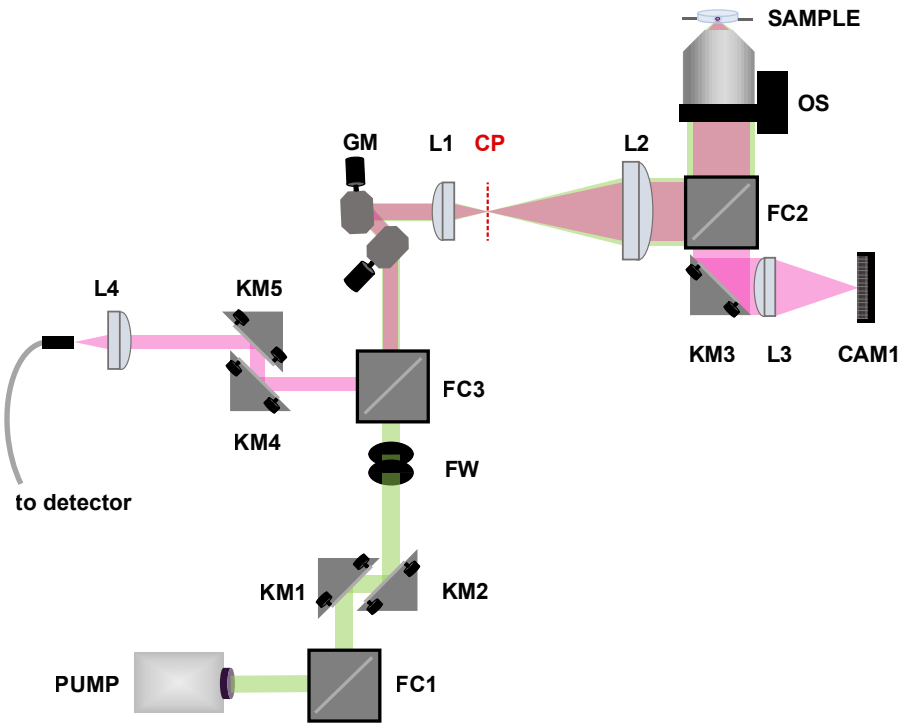

Fig. 4.1. Schematic of the home-built confocal scan head. A pump laser (green) is scanned across the sample using galvo mirrors (GM) and a piezo-electric objective scanner (OS). The de-scanned laser emission (magenta) is split off the optical path by a dichroic mirror (FC3) and coupled into an optical fibre connected to the spectral detector.

sectioning. The fibre then transports the signal to the spectroscopy module containing the detectors for the confocal imaging. Alternatively, transmission Brightfield images of the sample can be recorded on camera CAM1, which is necessary for real-time sample observation. A 90:10 beamsplitter (in FC2) allows 10% of the light emitted by the sample to be transmitted, before it is focused onto CAM1 using a tube lens (L3). Additionally, long-pass filters are added in the two collection paths (LP1, LP2; Figure 4.2) to block the short pump wavelength from the detectors, protecting them from potential damage at high excitation energies. Additional optical elements allow for more flexibility to tune and align the setup: The pump energy can be controlled by inserting variable neutral density filters into the beam path, which attenuate the pump energy in a controlled manner, and are housed on a rotating filter wheel (FW). Different pump lasers (e.g. EXC1, EXC2) can be coupled in by adding a removable mirror to the beam path (FC1). Lastly, various kinematic mirrors (KM) allow aligning different parts of the optical path in the $x-y-$direction: KM1 and KM2 are used to adjust the pump laser, KM3 centres the transmission image on CAM1, and with KM4 and KM5, as well as a translation mount holding L4 for $z-$alignment, the coupling of the fluorescence or lasing emission into the

optical fibre can be optimised. Lastly, the sample is housed on a motorised stage which allows automated movement for scanning of different areas.

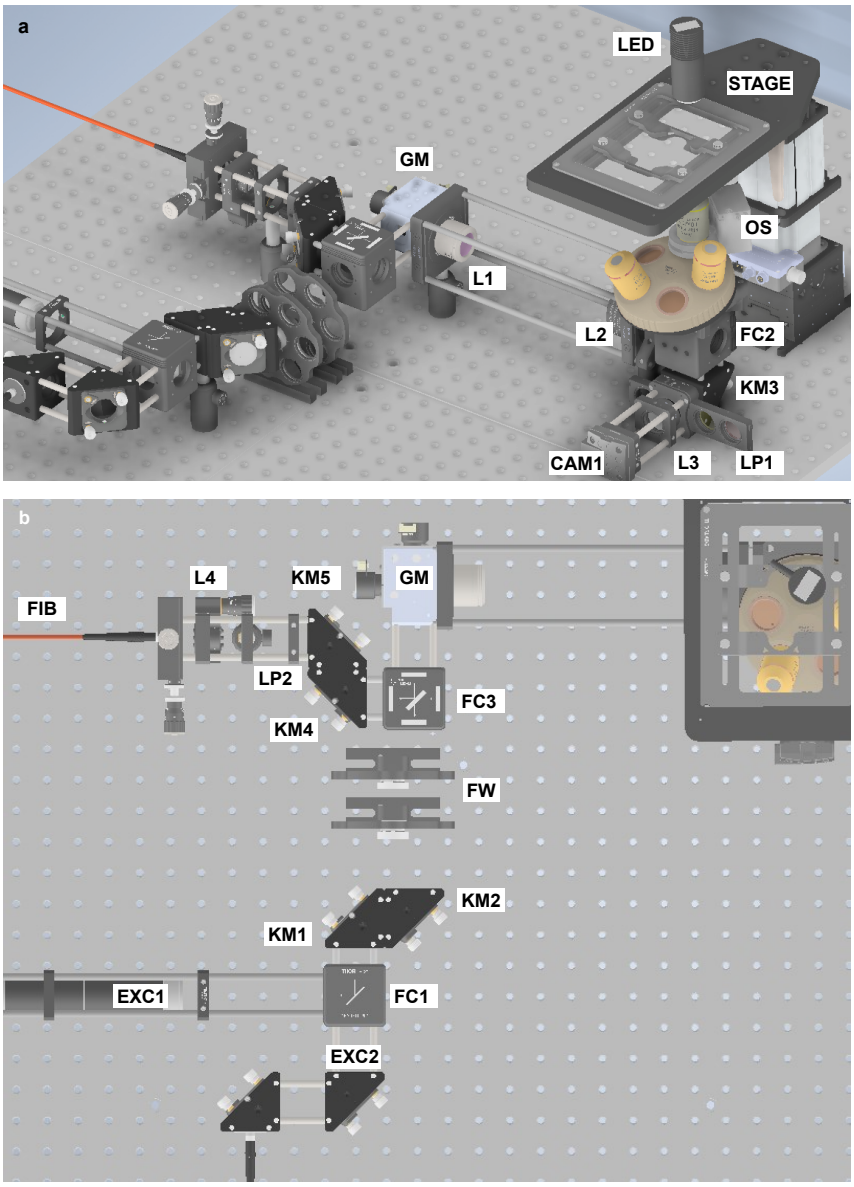

Fig. 4.2. CAD drawing of the home-built confocal scan head with components from Figure 4.1 labelled, as well as additional optics allowing adjustment and alignment of the optical paths.

The other end of the optical fibre is connected to the spectroscopy module (Figure 4.3). The light emerging the optical fibre is imaged to the entrance plane of a dispersive spectrometer, using a simple relay (L5, FC4, L6). The filter cube in the relay system is typically empty, but allows the insertion of additional optics, e.g. during alignment of the optical fibre, where light is coupled from the detector side into the fibre to visu-

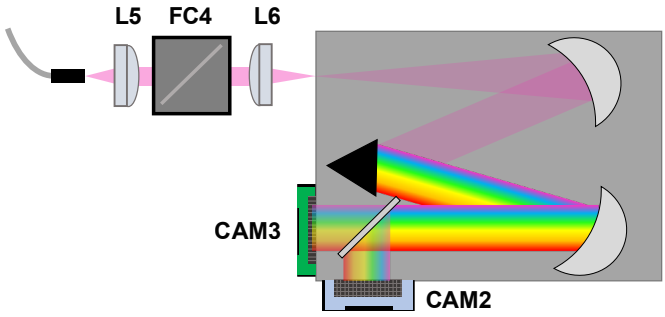

Fig. 4.3. Schematic of the spectroscopy module. A relay system (L5, FC4, L6) images the light emerging the fibre onto the enctrance plance of a dispersive spectrometer. The wavelength-dispersed signal can be read on either of two detectors; the sensitive CCD camera (CAM2) or the high-speed line-scan camera (CAM3).

alise the spot of signal collection (Figure A.5). The spectrometer spatially separates the incoming signal by its wavelengths, such that an image of the fibre core, horizontally convoluted with a translation by a specific distance corresponding to the signal wavelength, is produced on the camera. A flip mirror allows switching between a sensitive and slow EM-CCD camera (CAM2) and a high-speed CMOS line-scan camera (CAM3) that is used for CHSI. The line-scan camera was mounted to the spectrometer with a custom adaptor allowing 3-axis-translation and rotation for precise camera alignment. The spectrometer is equipped with three gratings that have a pitch of 300 $\frac{1}{\text{mm}}$, 1200 $\frac{1}{\text{mm}}$, and 1800 $\frac{1}{\text{mm}}$. Gratings with a higher pitch provide better spectral resolution at the cost of reduced bandwidth and sometimes increased aberrations. The 1200 $\frac{1}{\text{mm}}$ provided the best combination of bandwidth and resolution (27.5 nm and 0.06 nm, respectively) for this work, therefore it was most frequently used here.

A comprehensive list of all hardware used for the custom-built setup can be found in Tables A.2 and A.3, including the labels as used in the figures where applicable.

4.1.2 Automation and hardware control

In addition to constructing and aligning the optical path, an important part of the development of the microscope was to develop software capable of automating and synchronising the measurements. Importantly, the raster-scanning of the confocal spot was automated, and the acquisition of individual spectra on the camera was synchronised to the dwell time of confocal voxels. For the acquisition of spectra on the camera, a GUI called HyperspectralVideo.exe was developed using the C++ based software development kit provided by the camera manufacturer. HyperspectralVideo.exe pre-allocates memory for all images,

or camera buffers, of the measurement and gradually fills them with data during the acquisition. It allows the user to determine the size and resolution of the $x-y-z-$stack, the pixel dwell time and the duration of the time series. These user-defined values are written to a text file such that the script controlling the confocal scanning hardware can access them.

The starting point for this program was the previously developed LabView script GP-Scan[122], which raster-scans the spot in $x-y$ by calculating voltage values for each pixel that are applied to the galvo mirrors through a data acquisition system (DAQ). It thereby rotates the galvos by a controlled angle leading to a deflection of the beam. The DAQ also generates an analogue trigger signal at each pixel, which is then connected to the input trigger cable of the frame grabber of CAM3. Here, the LabView script was first adapted to read the user-defined scan settings from the aforementioned text file such that all parameters automatically match the camera acquisition software. Secondly, the script was updated to include the $z-t-$scanning. For this, the $x-y-$scan was first embedded in an $x-y-z-$loop, where at each iteration, a new $z-$position for the stack is calculated and sent to the piezo-electric objective scanner, which moves the objective such that the confocal spot is focused at a new $z-$plane. This $x-y-z-$loop was embedded in another loop for time series acquisition, which simply repeats the acquisition of the stack for a specified number of time steps. Lastly, delays after each line of the $x-y-$scan and after each $x-y-$scan, or frame, were implemented to reduce image artefacts.

The remaining hardware, including the pump laser and the spectrometer, was not integrated in this software solution, therefore the desired measurement settings, like the pump repetition rate or the type and position of the spectrometer grating, need to be set using the respective instrument software prior to starting the measurement. Importantly, the mechanical shutter of the spectrometer needs to be set to the 'Open' position at all times.

The motorised stage of the microscope was also automated separately using Python, such that large-FOV stitching or parallel scanning of multiple FOVs was possible. The synchronisation of the movement of the stage with the confocal scanning was achieved by continuously writing the frame number of the scan to a text file, which was then read by the Python script. The script also read the other parameters of the acquisition, including the spatial dimensions of the scan, so that it could automatically calculate on which frames to move to a new position. Images of large FOVs could then be stitched together during the data analysis in Python either by simply combining the images (Figure A.6) or by smoothing the edges of the tiles (Figure A.7).

Data structure

The specifics of the hardware control and synchronisation also determine the structure of the resulting data sets. Each $x-y-$scan, or frame, in the acquisition corresponds to one image stored by HyperspectralVideo.exe. Each image therefore holds an $x-y-\lambda-$hypercube, where each row in the image holds an individual spectrum and the rows are sequentially filled at each pixel of the $x-y-$scan. For the $z-$ and $t-$dimensions, separate frames are then stored as separate images. Therefore, individual images have N_λ columns and $N_{x\times y}$ rows, and each measurement creates $N_{z\times t}$ images, which are then interpreted by custom data processing software to map the measured spectra to the correct positions in the hypercube. In measurements with automated scanning of multiple FOVs, these are also stored as additional images, and the dimension F representing the different scan areas is again encoded in the sequence of stored images, which then becomes $N_{z\times F\times t}$. Lastly, the wavelength information is stored in an interleaved form in the individual rows, which is a consequence of the high-speed readout of the line-scan camera that divides the sensor in four segments which are read out in parallel (Figure A.4).

The images acquired by the camera contain exclusively intensity information, therefore an important function of the processing software is to apply correct spatial and spectral calibration. The following two sections discuss how this is implemented here.

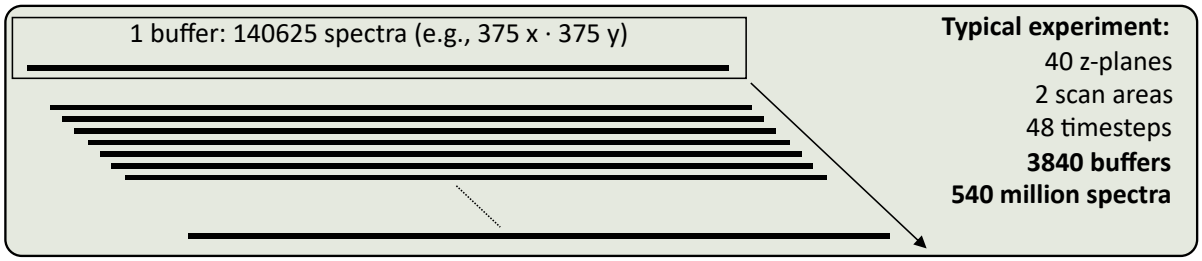

Fig. 4.4. Schematic summarising the structure of data acquired in CHSI, here shown for an example measurement (the corresponding measurement is shown in Section 5.3). Individual camera buffers hold spectral and spatial information of one $x-y-$plane, and all other dimensions are encoded in the sequence of separately stored images.

4.1.3 Data processing

The data processing algorithms were developed in Python and organise the large, multi-dimensional data sets in a way that enable easy extraction of spectral features of interest, and straightforward display of image data with intuitive colour-coding representing specific quantities of interest[3]. A custom data structure was developed that holds all the metadata of a given measurement and therefore can map the sequentially acquired spectra to the correct spatial positions. This data structure was implemented as a Python class with the metadata stored as attributes, which has the advantage that any methods for performing data processing operations can directly access these attributes. For example, the object *Measurement_A* will have the $x - y - z$ dimensions of the confocal acquisition stored as class attributes, and the method creating images can automatically create an image representation of the hypercube from the $(x \times y \times z)$-long train of spectra with the correct pixel size without requiring further specification of this from the user. This metadata is directly read from the log files returned by the camera.

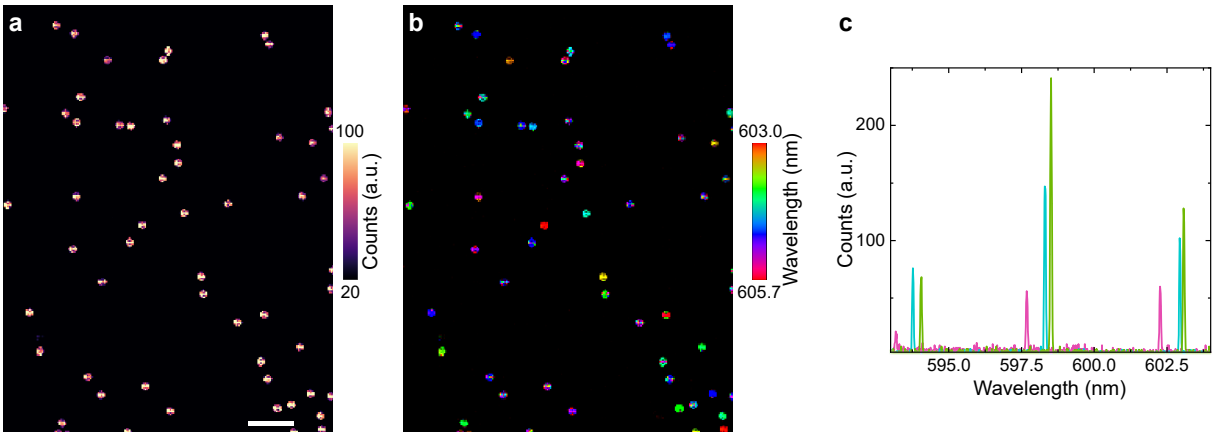

Fig. 4.5. Standard methods of the CHSI data processing software. a, Displaying the image data as intensity-based image and **b,** colour-coded according to wavelength. Scale bar, 100 µm. **c,** Extracting individual spectra from specified positions in the image.

Some results from fundamental image processing methods are displayed in Figure 4.5 using the example of a hyperspectral image of 15 µm polystyrene (PS) microbead lasers. The images can be represented either colour-coded by the maximum intensity of the spectrum at the given pixel (4.5a), or by wavelength (4.5b). For the wavelength-based image, the wavelength corresponding to the brightest pixel value in the spectrum determines the colour, and the colour-mapping can be limited to a spectral region of interest, e.g. between 603 nm and 605.7 nm in Figure 4.5b. This can be useful to limit the colour-mapping to only a subset of the spectrum, e.g. the wavelength range expected for peaks of the same

mode number in a multi-mode spectrum. Such colour-coded images are displayed in 2D using the standard python library matplotlib[123], or in 3D with the multi-dimensional viewer napari[124].

The individual spectra can also be extracted from positions specified by the user (Figure 4.5c), and some functionality for routine data analysis such as peak fitting is implemented to allow automated high-throughput data analysis. More advanced data analysis programs were developed on the basis of this fundamental processing suite, which are specific to some of the applications shown in Chapter 5 and will be revisited in the respective sections. A detailed description of all data processing software and its functionality is found in Appendix A.1.

4.1.4 Calibration

The results obtained with the data processing software rely on prior performance of a series of calibration measurements, whose results are stored in the processing script and use the metadata stored in the measurement class to adapt the calibration for new acquisition settings.

First, the spectral calibration was performed by recording spectra of a calibration lamp with at least three well-defined peaks corresponding to atomic transition lines present in the emission spectrum of the calibration lamp. For each grating, the spectra were imaged on the calibrated CAM2 first for reference, and then the same spectrum was recorded on CAM3 for the CHSI calibration. Using the reference spectrum from CAM2, the peak

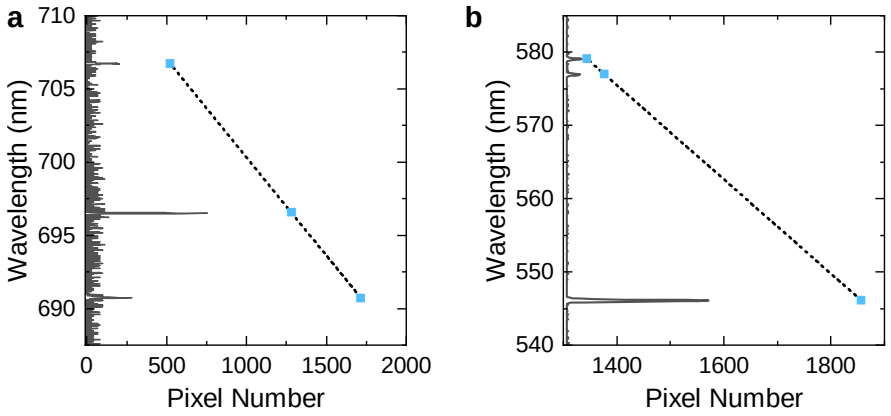

Fig. 4.6. Spectral calibration. Measured calibration spectra (solid line) showing 3 well-defined peaks (blue symbols) used for the linear calibration function (dashed line). **a,** Calibration for the 1200 $\frac{1}{\text{mm}}$ grating and **b,** for the 300 $\frac{1}{\text{mm}}$ grating.

position was roughly determined and the closest-matching transition from literature[125] was assigned to the peak. Assuming a linear relationship between the camera pixel on CAM3 and the assigned wavelength, the three peak positions were fitted and the two fit parameters (a, b) were stored in the calibration function of the processing script, along with the centre wavelength λ_0 of the grating, which had been set in the spectrometer software during the calibration measurement. Shifting the centre wavelength to a new centre wavelength λ_c should add a constant offset to the spectral calibration corresponding to the shift of the central position, allowing the calibration to be applied to measurements with settings differing from those used during the calibration measurements. All spectral calibration peaks and fit parameters are summarised in Table A.4. Using these parameters, the calibration of a camera pixel is given by

$$\lambda(p, \lambda_c) = a \times p + b + (\lambda_c - \lambda_0). \tag{4.1}$$

Next, the spatial calibration of the custom-built scan head was performed. For this, a calibration slide with marked distances was imaged with all three objectives that are of interest for CHSI applications (4×, 10×, and 25× magnification). In the processed images (Figure 4.7b), the marks of the calibration slide allowed to accurately determine the size of the scan field of the respective scan. From this, a scan calibration value was calculated,

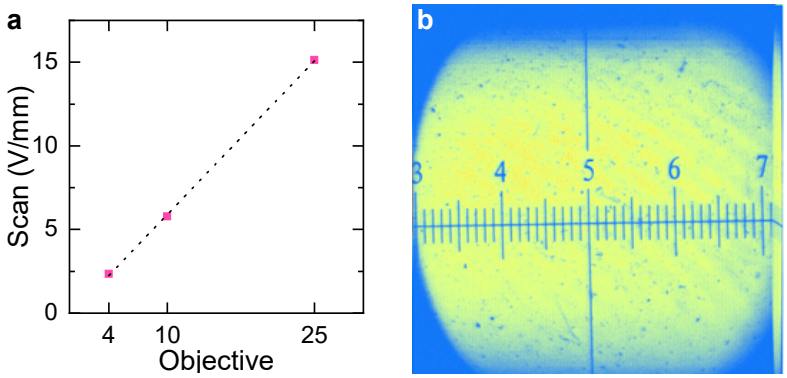

Fig. 4.7. Spatial calibration of the scan head. **a,** Measured scan field calibration values for the three objectives commonly used for CHSI. **b,** Exemplary image to determine the size of the scan field obtained with the 4× objective.

which represents the voltage amplitude in the LabView software needed to achieve a scan field with an edge length of 1 mm (Figure 4.7a). As expected, the magnification of the confocal scan field linearly scales with the objective magnification. A summary of all measured calibration values can be found in Table A.5. The calibration image shown here was obtained at a voltage of ±5 V, at which some vignetting is noticeable, which is typically observed for scan voltages of approximately ±4.5 V and higher. The origin

of this is the confocal tube lens, since the specific component integrated into this setup was not designed for laser scanning. Where large FOV measurements are a priority, and budgeting is not a concern, designated telecentric tube lenses are a better alternative.

4.2 Integration with commercial confocal microscopy

For integration of CHSI with commercial confocal microscopes, several modifications were made to both hardware and software compared to the home-built system described in the previous sections. For the optics, some constraints result from the specifications and engineering choices of the commercial microscope used, which means that this microscope needs to satisfy some requirements to be compatible with CHSI. Additional custom hardware solutions for the coupling of the optical signal from the microscope to the CHSI module are necessary, which vary depending on the type of microscope. A description of the requirements on a commercial system, as well as the necessary modifications, is provided in Section 4.2.1. Additionally, communication between the commercial confocal scan head and the CHSI acquisition was established to ensure synchronisation (Section 4.2.2), and the data processing routines were adapted to the different data format of this technique (Section 4.2.3).

4.2.1 Optical setup

For integrating CHSI with commercial laser scanning microscopy, the main requirements on the side of the optics pertain to the pump source and the signal collection. A challenge for the pump source is that typical visible lasers used for confocal imaging are not compatible with exciting micro- and nanolasers because either the pump lasers operate in the CW mode, or their pulses are not energetic enough for exciting typical microlasers above threshold. One alternative can be coupling in additional sources, if the scan head allows this. Here, this approach was used to implement CHSI measurements on the Nikon C1si confocal microscope, where the confocal pump laser is free-space coupled to an optical fibre, which is then connected to a flexible fibre port in the scan head. This allows both coupling another pump laser into the optical fibre, and simply switching the fibre, but care should be taken to ensure compatibility with the other components in the scan head, including dichroic mirrors and filters. An alternative is using one of the lasers of the commercial system for excitation of the microlasers, which is possible with the high-energy pulsed lasers used in multi-photon microscopy, either by single-photon excitation

of IR-emitting microlasers[7] or by two-photon excitation of microlasers with band gaps in the visible as demonstrated in Section 3.2. In the present work, the latter approach has allowed pumping semiconductor nanolasers with a Leica Stellaris microscope that was equipped with the DIVE multi-photon module and a Spectra Physics Insight X3 fs laser.

Secondly, the optical path of the emitted light needs to be accessible for coupling to the high-speed and high-resolution spectral readout. For this, the spectroscopy module was placed on a portable trolley including the optical fibre relay, such that this 'spectrolley' module could be moved between the respective setups. Flexible fibre mounts allowed con-

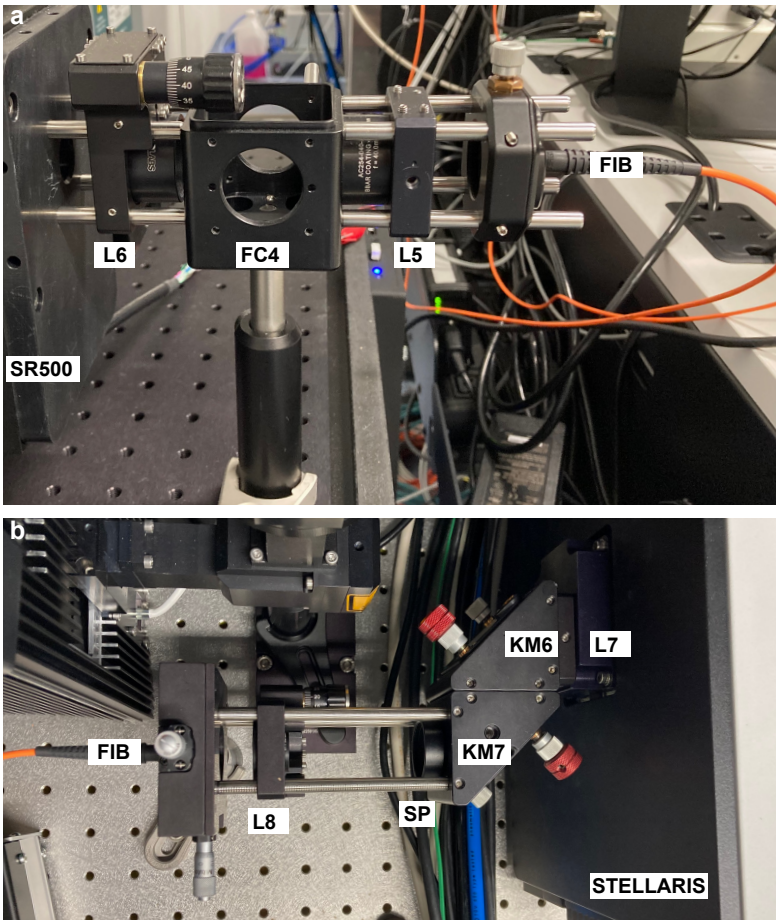

Fig. 4.8. Labelled photograph of the custom fibre coupling modules. a, Fibre port and relay for coupling the signal from any microscope to the spectrometer (SR500) and **b,** custom optics to collect the signal from the Leica Stellaris.

necting various fibres from the respective microscopes to the unit (Figure 4.8a). Thanks to the relatively open design of the Nikon C1si, the other end of the fibre could directly be connected to the scan head, making use of a second flexible fibre port present on this

scan head. For retrieving the microlaser emission from the Leica Stellaris, a custom out-coupling module was constructed to collect the descanned signal (Figure 4.8b). In the microscope, a flip mirror allows the signal to emerge through a window in the side wall of the scan head casing rather than deflecting it towards the in-built detectors, and the custom coupling port was designed to seamlessly attach to this window. The signal is first collimated at the exit by lens L7, before the beam is aligned in x and y by using a pair of kinematic mirrors (KM6, KM7). Lens L8 focuses the signal onto the fibre face and is housed in a translation mount for re-positioning along z. Additionally, a short-pass filter (SP8) prevents back-reflections of the NIR excitation to be transmitted to the detectors.

4.2.2 Camera control and synchronisation

Similar to the home-built CHSI setup, an analogue trigger signal is generated by the scan head, which starts the spectral acquisition on CAM3. Both of the commercial scan heads used here have an electronic interface for connecting trigger cables, but neither of the devices provides a trigger at each pixel like the home-built setup. Therefore, the line trigger is used to start the camera acquisition, but the individual pixels are gated by the internal clock of CAM3, and the pixel dwell time needs to be set manually in the camera software to match the scan speed of the confocal scan head. Additionally, a delay between the trigger signal and the scan start was found, which caused the hyperspectral image to contain a large fraction of dark pixels at the beginning of each line, and miss the equal amount of pixels from the real image at the end of each line. The magnitude of this delay could easily be calculated based on the number of missed pixels, which allowed to set a delay for the start of the camera acquisition by the correct interval to match the confocal scan start. These delays were 812.76 µs for the Leica trigger signal and 5529.6 µs on the Nikon C1si scan head, which were set in the camera configuration file under 'External Trigger Delay' in units of nanoseconds.

Owing to the different triggering configuration, the allocation and layout of the camera buffers needed to be adjusted, too. To ensure the camera acquires the correct number of pixels per line, the confocal line trigger is used as a frame trigger in the camera environment, and the number of spectra contained in an individual image now is equal to the number of pixels in the spatial $x-$direction. Consequently, the individual camera buffers now are $x-\lambda-$images and the $y-$dimension is encoded in the buffer sequence along with z and t.

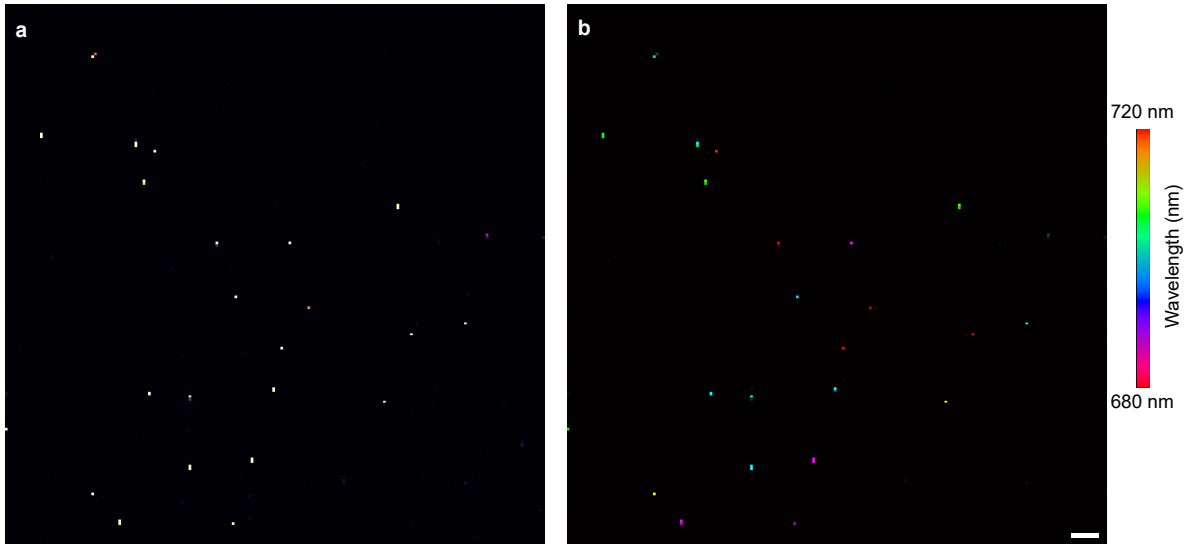

Fig. 4.9. Processed results of a two-photon excited hyperspectral image of nanodisk lasers, displayed as **a,** intensity image and **b,** wavelength image. Taken with the Leica Stellaris CHSI setup. Scale bar, 25 µm.

4.2.3 Modifications of data processing workflows

Following these changes in configuration of triggering and acquisition, the data structure of the measurements is different, therefore the data processing software needed to be adapted. The previously used Python structure holding measurement metadata and providing data analysis functionality can also be used for commercial confocal acquisitions after some designated methods were added to this class. Firstly, the automated reading of metadata from the acquisition log files was updated given that in the commercial confocal acquisition the axis labelling convention has changed. Secondly, any function that accesses raw data from the measurement was adapted to include the new mapping of data storage location to spatial axes. Specifically, this meant updating the method of encoding the spatial $y-$axis, which is interleaved with the spatial $x-$axis in individual images in the case of the home-built setup, and interleaved with spatial z as well as time dimension in the commercial confocal version. Therefore, a set of methods with the affix 'CCF' (for commercial confocal) in the function name was added to the software package that allows achieving equivalent results as previously described from the home-built setup. Figure 4.9 shows intensity- and wavelength information of hyperspectral images of semiconductor nanodisk lasers obtained using the CHSI implementation on the Leica Stellaris scan head.

For the commercial confocal scanning implementation of CHSI, the spectral calibration

is identical to that of the home-built setup, given that the same spectroscopy module is used. The spatial calibration is provided by the software of the respective confocal scan head, and is stored in the metadata of the dark image that is automatically acquired by the confocal microscope during CHSI measurements.

4.3 Hyperspectral imaging results

In the following sections, the results of imaging micro- and nanolasers with the developed CHSI setups are discussed. Firstly, the general measurements performed to characterise the home-built setup are summarised, which includes measurements to quantify spectral and spatial resolution, as well as investigating speed and spatial scalability of the measurements. Then, results specific to each type of laser are presented, i.e. polystyrene microbead lasers and semiconductor nanodisk lasers, which includes results with both the custom and the commercial scan head.

4.3.1 Performance of the home-built microscope

Spectral resolution

Optimising the spectral resolution is crucial for successful measurements and analysis of lasing spectra, such that minuscule shifts in the mode position, e.g. during refractive index sensing measurements, can be resolved. In the dispersive spectrometer used here, high spectral resolution is achieved by employing a grating with a high pitch, and by closing the entrance slit of the spectrometer. As briefly discussed in Section 4.1, the highest-pitch grating (1800 $\frac{1}{\text{mm}}$) was rarely used in this work because of the limited bandwidth and risk for aberrations. Therefore, the resolution of the spectrometer using the 1200 $\frac{1}{\text{mm}}$ grating was optimised through careful selection of coupling optics at the entrance slit of the spectrometer. Closing the slit to its minimum value of 10 µm and ensuring parallel alignment of the slit and the vertical axis of the camera produces the sharpest image of the wavelength-dispersed signal on the detector and therefore the optimal resolution. However, closing the slit also rejects part of the signal by cropping the edges of the image formed by the fibre in the plane of the slit, depending on the fibre core size used and the relay optics. Although de-magnifying the image of the fibre core such that its size is $\leq$10 µm might at first sound like a sensible solution, this would in return increase the divergence of the signal and lead to a mismatch with the NA of the parabolic mirrors

inside the spectrometer. Higher throughput is achieved by magnifying the image of the fibre core to match the NA of the spectrometer, such that the full signal can be used in the $y-$direction, allowing to crop the signal in the $x-$direction for resolution optimisation. Therefore, the magnification of the relay system ($M = 1.25$) was chosen to reduce the divergence of the light emerging the low-NA multimode optical fibre (NA=0.1 for all fibres used) to match the spectrometer acceptance angle (NA=0.077). This approach

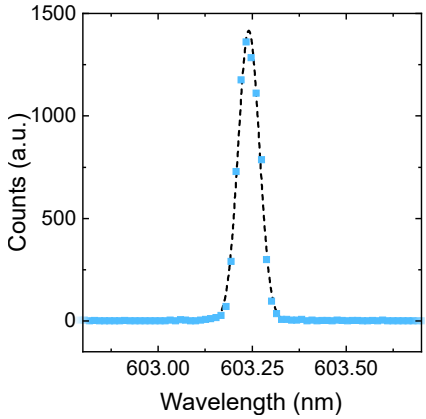

Fig. 4.10. Measurement of a resolution-limited lasing peak (blue symbols) fitted with a Gaussian function (dashed line) with a FWHM of 66 pm.

allowed for a good combination of throughput and resolution, such that the nominal optimal resolution quoted by the manufacturer of the spectrometer was reached even at the shortest pixel dwell time of 8 µs, corresponding to integrating only over a single excitation pulse. Figure 4.10 shows the resolution-limited lasing peak of a PS microbead laser acquired with the 25× objective.

Spatial resolution

Compared to the spectral resolution, the spatial resolution is less important for the setup development, given that aim of the setup is to resolve microscopic lasers that are typically $2 - 15$ µm in diameter. Although it can be of interest to perform high-resolution CHSI of sub-resonator patterns (e.g. some of the results shown in Section 4.3.2), it is usually sufficient for high-throughput biological applications (e.g. Chapter 5) to accurately localise the microscopic lasers. Nevertheless, understanding how the optical engineering choices affect the spatial resolution is an important part of optimising the setup. Assuming otherwise correct alignment and proper overfilling of the back aperture of the objective, the

spatial resolution is mainly controlled by the confocal pinhole, which here corresponds to the diameter and acceptance angle of the optical fibre.

Two different fibres were used routinely that could be readily switched by using flexible fibre mounts, reflecting 'open pinhole' and 'closed pinhole' configurations. Both fibres had a small acceptance angle (NA=0.1) due to the considerations on the spectrometer side discussed above, and also were selected from standard suppliers of optical components to ease reproducibility. The 'open pinhole' fibre with a diameter of 105 µm was chosen as a good trade-off of easy incoupling on the scan head side, and acceptable losses from edge clipping at the spectrometer slit. The 10 µm core size corresponds to a pinhole size of $\sim$ 2 AU for the combination of lenses in our scan head, which was selected as the 'closed pinhole' configuration. The size of the pinhole as compared to the diffraction-limited excitation spot can be assessed by imaging both the excitation spot, using a fluorescent target, and a spot of light that appears when coupling light from the far-end of the optical fibre (i.e., the 'pinhole' alignment method mentioned in Section 4.1.1). Figure A.5 shows results from performing this visualisation technique with both fibres used in the setup.

A z-stack of polystyrene microbead lasers was acquired under various measurement parameters to compare the resulting images, all obtained with a 10× objective. Figure 4.11a,b show images obtained prior to ensuring overfilling of the back aperture of the objective, which led to poor axial resolution as expected. After adding a beam expander to the excitation path, the back aperture was properly overfilled (Figure 4.11c,d), which allowed decent localisation of the microlasers along z, but still showed substantial out-of-

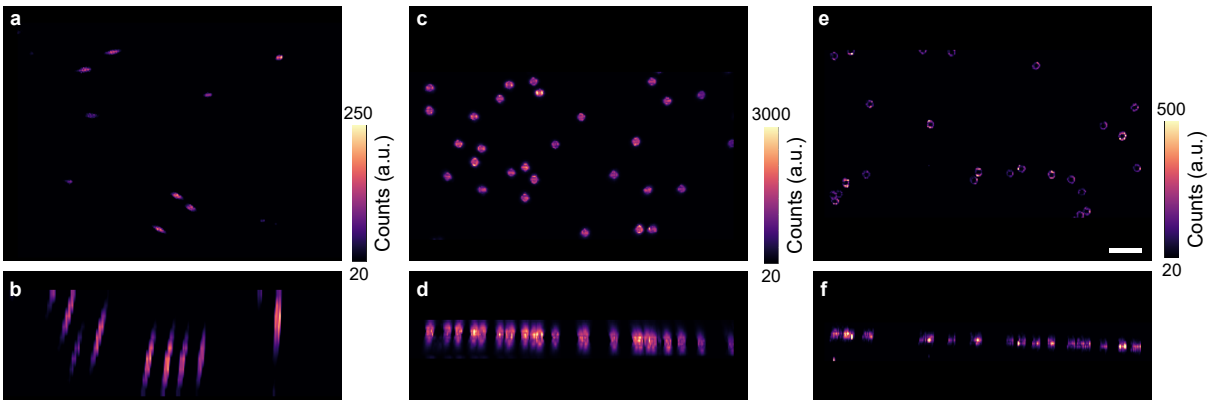

Fig. 4.11. Spatial resolution under different imaging conditions. a, $x-y-$MIP and **b,** $x-z-$MIP of PS lasers with the back-aperture underfilled and the 'open pinhole' fibre. **c, d,** corresponding results for the back aperture overfilled and the 'open pinhole', and **e, f,** for the back aperture overfilled and the 'closed pinhole'. Scale bar, 100 µm.

plane signal collection. The best sectioning was achieved with the 'closed pinhole' fibre (Figure 4.11e,f), but the overall signal amplitude was reduced compared to the 'open pinhole' image acquired with the same acquisition settings. While properly overfilling the back aperture obviously is necessary, both the open and closed pinhole configurations produced high-quality images and the trade-off between axial resolution and signal amplitude can be chosen according to the given application.

Quantifying the optimal spatial resolution by measurement of the PSF was attempted, but has proven to be challenging due to the lower signal level of the light emitted by the small fluorescent beads. The excitation with the strong and short pulses in CHSI typically damaged the beads before a high-resolution $z-$stack could be obtained. A measurement of dye-doped polystyrene spheres with a diameter of 1.61 µm was possible using the more sensitive CAM2, but this in return led to such slow scan times that there was substantial sample drift during the course of the measurement. The resulting image of the bead was deconvolved into a ground truth image of the object and a PSF, using a double-blind implementation[126] of the Richardson-Lucy algorithm for image deconvolution[127, 128]. The resulting FWHM of the PSF with the 25× objective was 631 nm laterally and 2.48 µm axially, however, due to the difficulty in obtaining high quality PSF measurements, these results likely overestimate the actual resolution due to the large noise and drift (Figures A.8 and A.9). The validity of this result for CHSI is further limited particularly in the axial direction, where the resolution of images of microlasers differs from that of fluorescent particles: In small nanolasers (compared to the Rayleigh length of the focused excitation beam), the nonlinear effects discussed in Section 2.2.5 can improve the resolution substantially. Additionally, the high refractive index contrast between the resonator and its environment, which is necessary for the optical confinement of the lasing mode, also leads to refraction of the pump laser beam at the interface of resonator and medium. Particularly in large microlasers, this artificially increases the extent of images of the particles in the $z-$direction.

One problem that appeared using the 10 µm fibre was the observation of an unexpected modulation of the fluorescent signal, that became apparent when using the sensitive EM-CCD camera (Figure 4.12). This effect is likely due to modal interference in small core multimode fibres, which happens when the fibre can only support a small number of modes that interfere with one-another[129]. Although this effect was not noticeable in CHSI images of lasing beads due to the high SNR of the lasing signal, which is much more pronounced than the interference effect, it might still have an effect on the relative intensity of measured peaks.

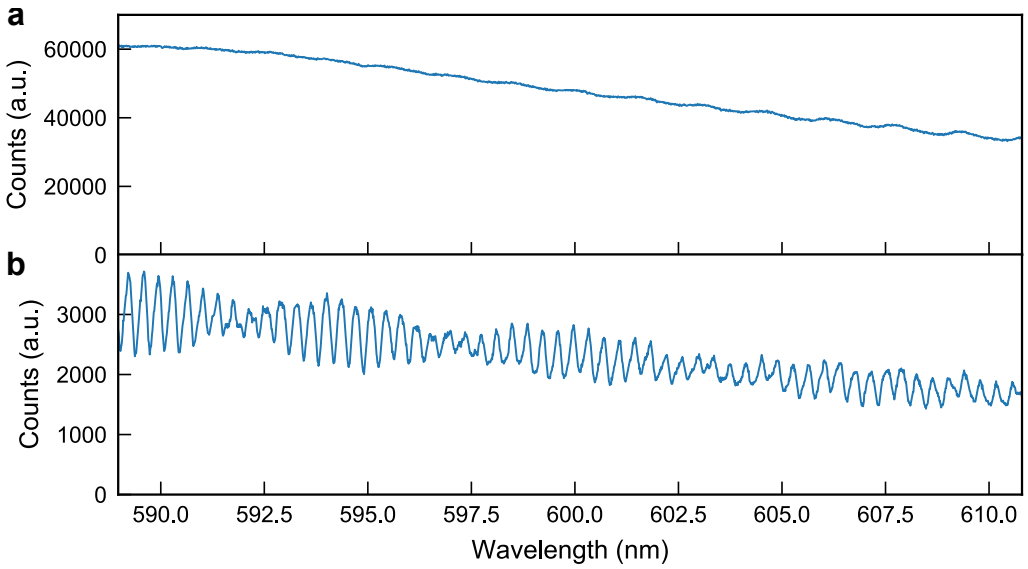

Fig. 4.12. Interference in multi-mode fibres. Fluorescent signal measured on the EM-CCD camera, **a,** using the 105 µm fibre and **b,** with the 10 µm fibre.

Spatial scalability

An interesting advantage of micro- and nanolaser measurements is that they contain near-field information about the surroundings of the microlasers in far-field imaging configurations. As long as enough photons are collected, this approach should be scalable for arbitrarily large samples, thereby allowing measurements like nanoscale refractive index sensing on macroscopic samples. A simple approach of attaining different spatial scales in microscopy is the use of objectives with different magnification, therefore it was of interest to establish how the use of different objectives affects the signal intensity. To avoid bias of the sample itself, this was measured by imaging a large number of PS microbead lasers with each objective, where the particles were randomly selected from a batch of commercial particles with generally very homogeneous quality. For each image, the peak intensities of the 499 brightest spectra were recorded to calculate an average brightness value (Figure 4.13). The images at the two high-resolution objectives (10×, NA=0.45; 25×, NA=1.05) were acquired with the same acquisition settings, whereas the image with the 4× objective (NA=0.1) required longer pixel dwell times to achieve sufficient signal quality. The brightness values for the 4× in Figure 4.13 were therefore divided by the factor which the integration time was increased by to correct for this, assuming a linear increase of collected photons with increasing integration time. Overall, a clear correlation was found between the average image brightness and the square of objective NA, which represents the solid angle of collection. The linear fit in Figure 4.13 does not describe

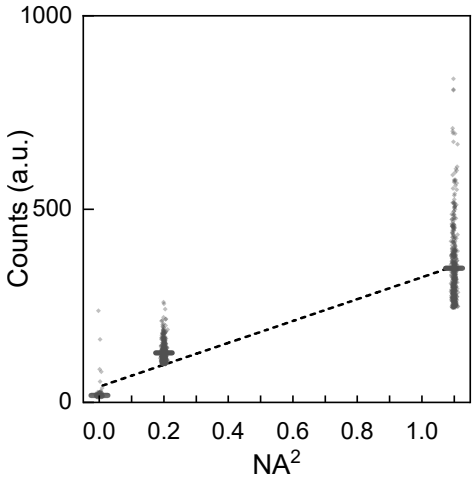

Fig. 4.13. Measurement of the average intensity in hyperspectral images measured with three different objectives (4×, 10×, 25×), plotted as a function of the NA^2 of each objective. Shown are the brightness values of all spectra ($n = 499$, grey dots) and the corresponding average values (centre line), which were used for the linear fit (dashed line).

the measured trend perfectly, which is likely due to different transmittances of the three objectives. Nevertheless, this measurement confirmed that good quality hyperspectral images can be acquired with a range of vastly different objectives when accounting for the decreased collection efficiency of low-NA objectives by increasing the pixel dwell time.

Scanning speed

The microscope was designed to run at a spectral acquisition rate of up to 125 kHz, which was limited by the minimum pixel dwell time achievable with CAM3. A further improvement to up to 250 kHz is in principle possible with this camera model, but this would require changing the settings on CAM3 to reduce the dynamic range of the image acquisition substantially. This is challenging for CHSI images of microlasers, given that their non-linear emission characteristics often lead to stark intensity fluctuations. Additionally, other hardware components limit the practical acquisition rate to 125 kHz: Firstly, the 532 nm pump laser used for exciting PS microbead lasers has a maximum repetition rate of 125 kHz. Secondly, the galvo mirrors used here have a maximum line rate of 175 Hz. The line rate of the galvos dictates the time it takes to scan a line of pixels in the $x-$direction, which is equal to the product of the number of pixels in x and the pixel dwell time. When running CAM3 at 125 kHz, the minimum number of pixels per line is already ∼715, which is often not a good choice because it oversamples the image (i.e., ac-

quires a large number of pixels per microlaser which provide no additional information). Oversampling the image does not only inflate the size of the data sets, but also does not provide a true improvement in speed. Therefore, a reduction in pixel dwell time on CAM3 would not only compromise spectral quality, but also require exchanging various hardware components. Consequently, the setup was operated at up to 125 kHz. Figure 4.14) shows exemplary images at 25 kHz (4.14a) and 125 kHz (4.14b). In both images, a small distortion artefact is present in the image, which is a result of imperfect movement of the galvos, but in the 125 kHz image, the nominal maximum speed of the galvos was exceeded (208 Hz line rate for a 600 pixel image sampled at 125 kHz), and this effect was more pronounced compared to the 25 kHz image (62.5 Hz line rate for a 400 pixel image). This issue can be circumvented by adding more pixels in the $x-$direction. Given that the distorted area is simply a resized mirror image of the non-distorted area, it is also possible to acquire at such fast scan times and simply discard the data in the distorted region, but operating the galvos outside their designated range is generally not advisable and can lead to additional errors in their movement during longer measurements.

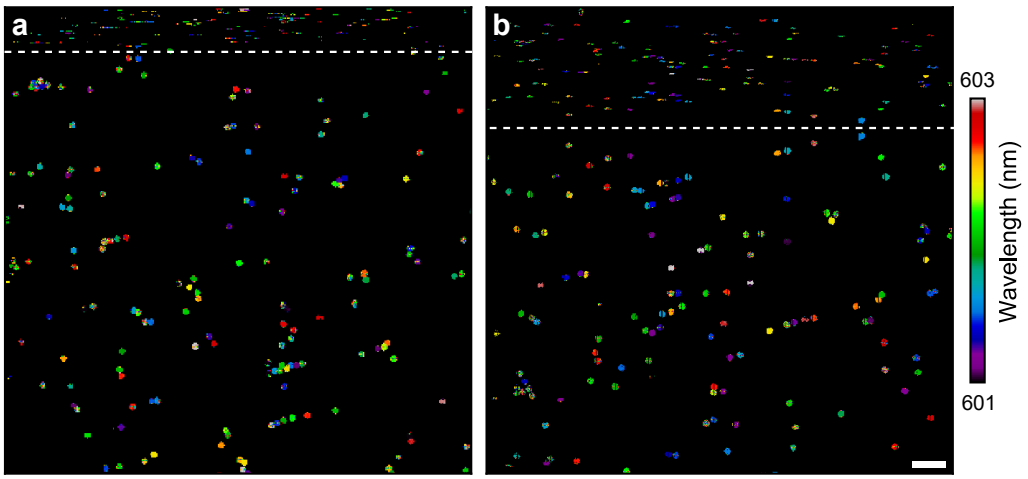

Fig. 4.14. CHSI wavelength maps of PS microbead lasers. **a,** Imaged at an spectral acquisition rate of 25 kHz and excited with a pulse energy of 1 nJ and **b,** at 125 kHz with a pulse energy of 1.5 nJ. The dashed lines indicate the boundaries of the distorted areas.

Nevertheless, high-quality hyperspectral image data could be obtained at all scan speeds, as shown by the clear non-distorted region in both images, as well as the excellent quality of lasing spectra measured at both speeds (Figure 4.15). Both images were acquired at 125 kHz pulse repetition rate of the pump laser, which corresponds to spectra with single-pulse excitation for the high-speed scan. To ensure sufficient signal brightness, the

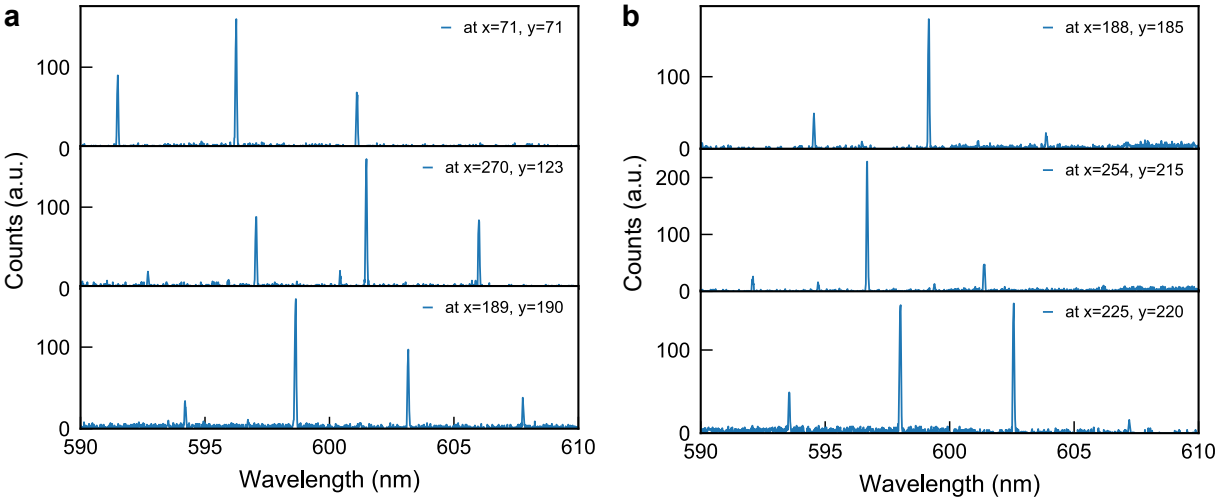

Fig. 4.15. Representative spectra of polystyrene microbead lasers. a, Acquired at 25 kHz acquisition time and an excitation pulse energy of 1 nJ and **b,** at 125 kHz acquisition time and an excitation pulse energy of 1.5 nJ.

excitation pulse energy was increased for faster acquisitions. Here, pulse energies of 1 nJ for the 25 kHz image and 1.5 nJ for the 125 kHz led to good results, which corresponds to 2× and 3× the lasing threshold of PS microbead lasers of ∼ 0.5 nJ (Figure A.10).

4.3.2 Polystyrene bead lasers

Many of the general properties of the optical setup were investigated and demonstrated using PS microbead lasers due to their high brightness, homogeneous sample quality, and commercial availability. These performance characteristics of the microscope apply to measurements of different types of microscopic lasers with the main differences dictated by the emission brightness of the respective lasers. The next two sections, however, discuss observations gained through hyperspectral imaging of micro- and nanolasers that are specific to the type of microscopic laser used, starting with PS microbead lasers.

Additional interesting information about these microlasers is gained by high-spatial resolution CHSI to reveal emission patterns that link the polarisation of the lasing emission to the molecular orientation of gain molecules. As already seen in Figure 4.11e,f, hyperspectral images of polystyrene microbeads show the lasing pixels predominantly along the circumference of the bead. High-resolution hyperspectral imaging was performed using the Nikon C1si scan head and a 25× objective, which revealed a characteristic pattern of TE-dominant and TM-dominant areas that alternate with angular position around the circumference, as seen by the colour distribution that represents the wavelength of the brightest peak (Figure 4.16a, e.g. cyan and red areas in the uppermost resonator).

The underlying trend in relative intensities of the TE and TM modes was examined by comparing individual spectra from a single resonator depending on their angular position along the circumference, i.e., the pixels which are false-coloured according to their position θ along the circumference (false-coloured pixels in Figure 4.16b). The projection of

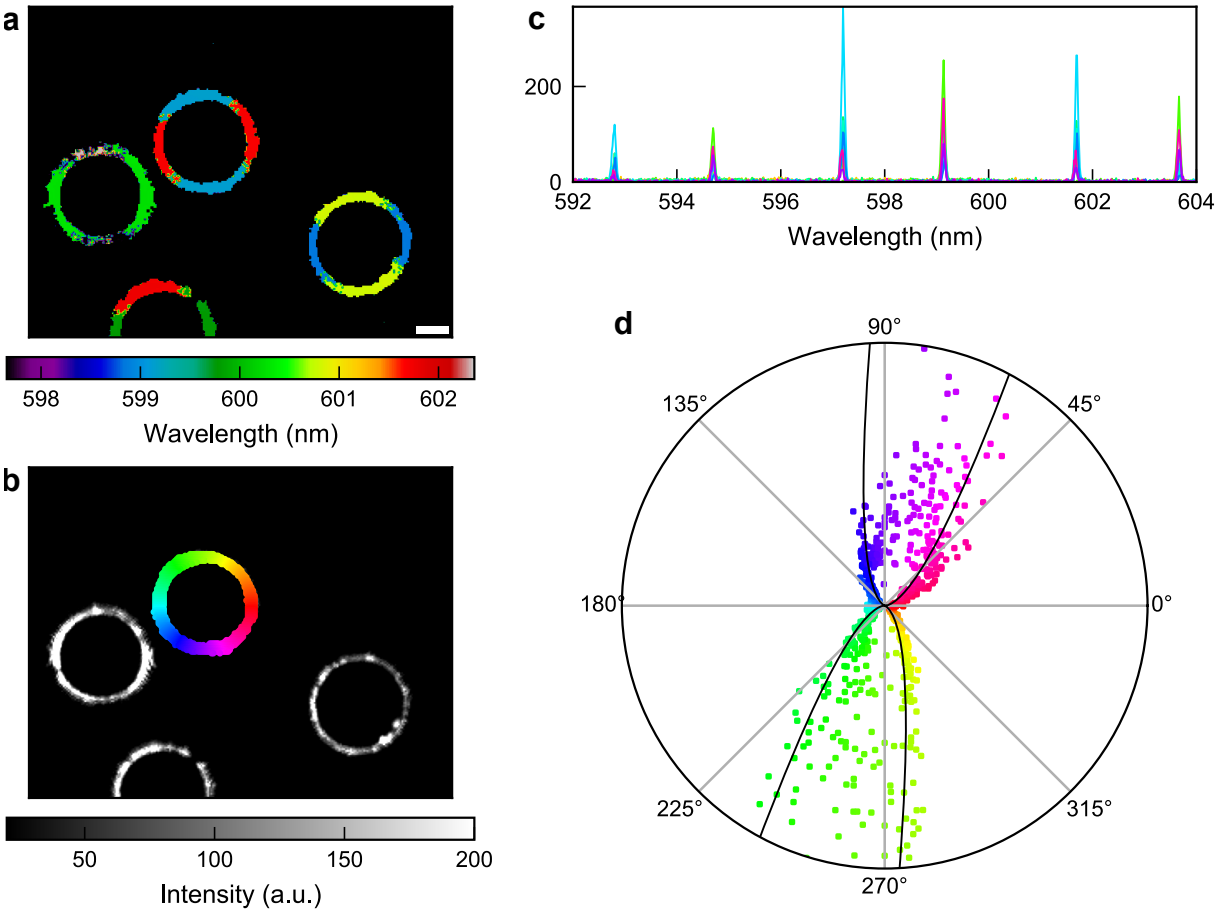

Fig. 4.16. Polarisation of polystyrene microbead emission. **a**, Hyperspectral image of four microbeads, colour-coded according to the dominant lasing mode within a narrow spectral window. Scale bar, 5 µm. **b**, Corresponding intensity image (grey scale) with superimposed pixels whose spectra were used for subsequent analysis, colour-coded by their angular position along the circumference of the microbead. **c**, Exemplary lasing spectra randomly extracted from various positions along the circumference, with colour-coding matching to that in **b**. **d**, Calculated ratio of the average brightness of three central TE and TM modes, showing an angular dependence in good agreement with the theoretical model (black fit). The limit of the radial axis is $\frac{I_{TE}}{I_{TM}} = 12.39$.

a linearly polarised beam onto the axis of a rotating polarizer is described as a function of angle of rotation θ by Malus' law, here with an arbitrary phase ϕ:

$$I = I_0 \cdot \cos^2(\theta - \phi). \tag{4.2}$$

Some example spectra are shown in Figure 4.16c, where the colour of the plotted spectrum is equal to the colour in panel b, and therefore also represents the angle θ. Spectra from the green area (Figure 4.16b) for example have the brightest TE modes in Figure 4.16c and the light-blue positions correspond to the brightest TM modes. This pattern was further analysed by calculating the average brightness from three central lasing peaks of each mode family, and determining the relative ratio of TE/TM brightness. The angular dependence of this is shown in the polar plot in Figure 4.16d, were the results were fitted to a model explained below. The projection of a linearly polarised pump beam onto the surface tangent of the microbead, which has a rotational symmetry, should behave analogously and vary with radial position as described by Equation 4.2. Due to the preferential excitation of molecules whose dipole moments align well with the polarisation of the pump laser, it is assumed that this trend remains valid for the intensity variation of the TE modes with θ. On the other hand, the electric field of TM modes oscillates in perpendicular direction, therefore the point of best overlap between pump and mode polarisation is shifted by $\frac{\pi}{2}$, which in return gives:

$$I_{TM} \propto I_{TM0} \cdot \cos^2(\theta - \phi - \frac{\pi}{2}) = I_{TM0} \cdot \sin^2(\theta - \phi). \tag{4.3}$$

In the measured spectra, the ratio of the two mode families was considered. The dependence of this ratio on θ was derived by combining equations 4.2 and 4.3:

$$\frac{I_{TE}}{I_{TM}} = A_0 \cdot \tan^2(\theta - \phi). \tag{4.4}$$

The experimental values (Figure 4.16d) were fitted according to Equation 4.4, with the phase ϕ and an initial amplitude ratio A_0 as free parameters.

To verify that this effect originates from the polarisation orientation of the pump, a half wave plate (HWP) was added into the excitation beam path. Rotating the half wave plate in the excitation path by a controlled angle rotates the polarisation of the pump laser accordingly. Therefore, the angular phase ϕ of the measured polarisation pattern is expected to shift by the angle of rotation of the pump. The measured trend indeed confirms this theory, but some divergence from unity is noticeable (Figure 4.17). Likely, some of the optics in the fibre-coupled confocal scan head are polarisation-sensitive, but due to the closed-system nature of the commercial confocal scan head, this could not be investigated further.

In conclusion, CHSI measurements with high-spatial resolution can provide further insight on the spatial distribution of mode families within the resonator, and the experiments here

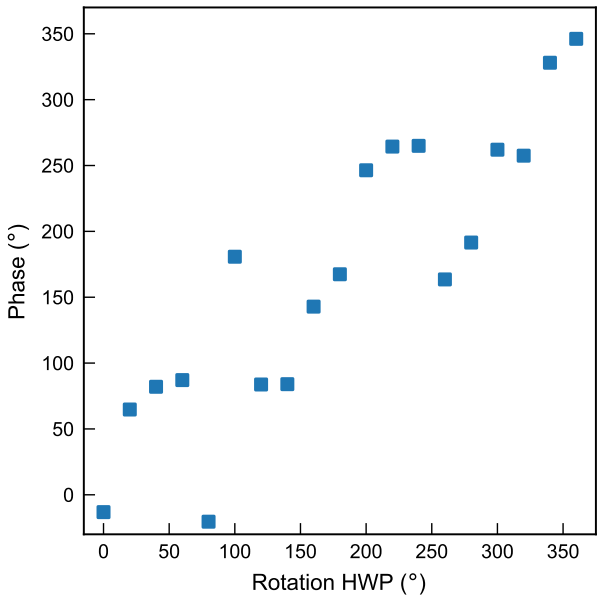

Fig. 4.17. Phase of the polarisation pattern extracted from fits to the theoretical model at different angles of rotation of the pump polarisation.

demonstrated the role of pump polarisation on the observed patterns. This is not only helpful for a more complete understanding of the factors involved in the lasing processes in such microresonators, but also could provide additional information in future measurements that had so far been unattainable. For example, in refractive-index sensing, only the average value of the external refractive index can be measured with the mathematical models introduced so far. Selective excitation of certain lasing paths or mode families, along with spatially resolved analysis of the spectral response of the resonator, might prove insightful for understanding more complex local environments around the microlasers.

4.3.3 Semiconductor nanodisk lasers

Many of the differences in imaging PS microbead lasers and semiconductor nanodisk lasers originate from the size difference of the two types of lasers. Firstly, CHSI images of nanodisk lasers need to be more finely sampled due to the Nyquist sampling theorem, which states that ≥ 2.3 samples should be acquired per object, which in return dictates the pixel size of CHSI. Secondly, not only the lasing threshold, but also the damage threshold and the emission brightness are about three orders of magnitude smaller, which affects the choices of the pump parameters and also highlights the need for efficient signal collection.

Consequently, nanodisk lasers were typically imaged with the 25× objective, and sometimes the 10× objective, whereas PS microbead lasers could also be imaged with a 4× objective. Objectives with even higher magnification were not included because the reduced FOV is often not ideal for the high-throughput focus of this work. For the typically single-mode semiconductor nanolasers, no spatial dependence of the lasing wavelength and polarisation was expected and therefore an analogous experiment to the one presented in Section 4.3.2 was not performed. Instead, the following section discusses how the results on the flexible excitation of nanodisk lasers (Chapter 3) can be exploited in CHSI. In the following section, a summary of how the excitation scheme affects some important measures of spectral and image quality is provided. Following the demonstration of nanodisk

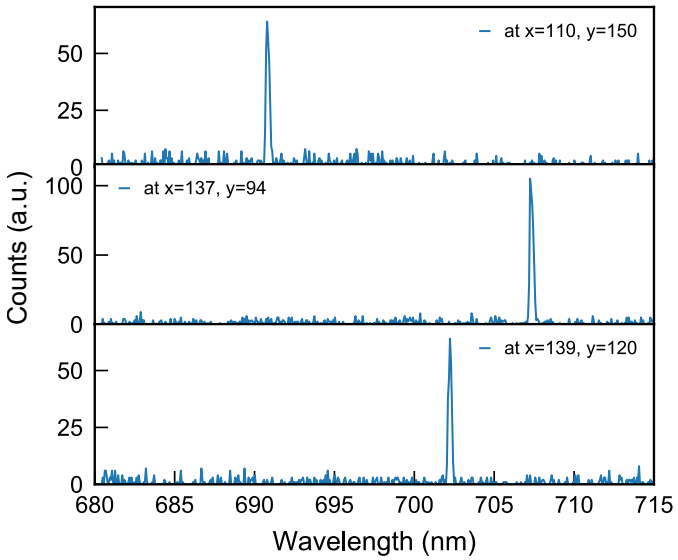

Fig. 4.18. Spectra of semiconductor nanodisk lasers obtained with excitation at 642 nm.

laser excitation at ≥ 640 nm through band gap engineering, CHSI of nanodisk lasers under single-photon excitation was usually performed with a 642 nm diode laser, which not only operates in the first therapeutic window but also offers a tuneable pulse repetition rate of up to 80 MHz. Exemplary spectra from a representative CHSI measurement are shown in Figure 4.18, showing narrow and well-defined peaks with excellent SNR. Due to the tuneable repetition rate of the pump laser, a large range of speeds for spectral acquisition led to high-quality spectra, and further experiments were conducted to investigate which combinations of pulse energy, pump repetition rate, and pixel dwell time are most favourable. Specifically, in the context of long-term applications of bio-integrated lasers, the stability of the lasing spectrum is very important, but stability is easily compromised due to overpumping.

Generally, higher pulse energies are required in CHSI as compared to traditional μ − PL setups due to the less sensitive camera and increased optical losses from the scanning optics, which poses a risk of overpumping. Therefore, pulse energy, repetition rate, and pixel dwell time should be balanced diligently to ensure good image quality and minimise nanolaser degradation. To examine this, a $z-$stack of nanodisk lasers embedded in agarose was imaged for an extended measurement, and all nanolasers in the stack that continuously showed lasing were detected and tracked such that their lasing wavelength could be extracted at each time step.

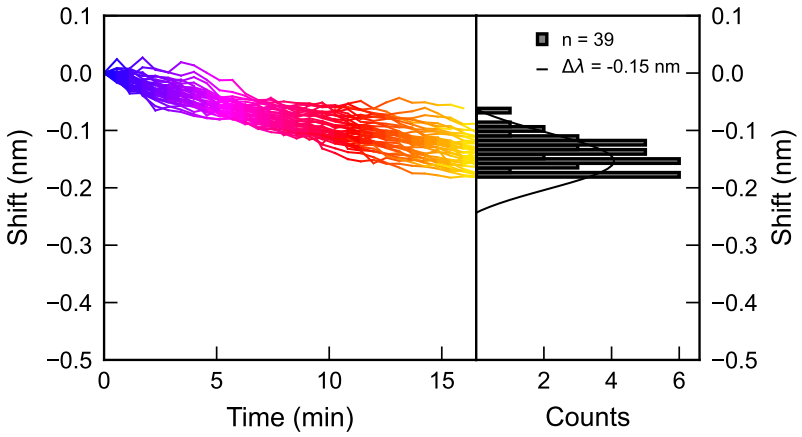

Fig. 4.19. Spectral stability of semiconductor nanodisk lasers. Left: Spectral shifts of all nanolasers during the measurement, $n = 39$. Right: Histogram of the distribution of the total spectral shift during the measurement. A Gaussian function was fitted to the histogram (black line) to determine the mean of the distribution.

Figure 4.19 shows the results of this measurement at a pump rate $f_r = 10$ MHz, a pulse energy $E_p = 5$ pJ, and a pixel dwell time $t_d = 19\,\mu s$. Four additional measurements with a different combination of parameters were performed following the same approach. The results from all measurements are summarised in Table 4.1, where experiment 4 corresponds to the data shown in Figure 4.19. The data from experiments 0, 1, and 3 is shown in Figures A.11, A.12, and A.13, respectively, whereas for experiment 2, only one nanolaser could be analysed, therefore no histogram is shown. To compare different parameters, the measured wavelength shift was also normalised by time ($\Delta\lambda_t$) and by number of incident excitation pulses ($\Delta\lambda_p$). Both high repetition rate and high excitation energy clearly increased the amount of red-shift of the lasing mode. There is a large variability observed in the shifts for each sample, and as a result of this, some noise was observed in the trends of the measured shifts. In general, however, the amount of degradation seems to roughly scale with the number of excitation pulses, apart from the case where the nanolasers were excited far ($\sim 10\times$) above threshold in experiment

3, which led to an $\sim 6\times - 10\times$ increase in observed shift per pulse. Of course, fast measurements like experiment 4, that require high pulse repetition rates due to the short pixel dwell time, also led to a stronger shift per total time elapsed, therefore increasing the measurement speed beyond the necessary sampling interval is not beneficial. While

Exp.	f_{rep} (MHz)	E_p (pJ)	t_d(µs)	$\Delta\lambda$ (nm)	$\Delta\lambda_t(\frac{\text{pm}}{\text{min}})$	$\Delta\lambda_p(\frac{\text{pm}}{10^3\text{pulses}})$	n
0	0.5	2.5	399	-0.14	-1.30	-0.702	10
1	0.5	5	399	-0.21	-1.95	-1.05	14
2	1	5	399	-0.24	-2.23	-0.602	1
3	1	9.9	360	-2.32	-11.9	-6.44	237
4	10	5	19	-0.15	-9.07	-0.789	39

Table 4.1. Wavelength stability of nanodisk lasing peaks for different imaging conditions.

these results suggest that both pulse energy and repetition rate of the pump should be limited where possible, it also was apparent that higher excitation energy allowed to excite larger fractions of the nanodisk lasers present in the FOV. Although separate FOVs were used for the measurements, which presumably contain different numbers of high-quality nanolasers, it was routinely observed that even increases in pump energy far above the expected lasing threshold still led to larger number of lasing devices in the recorded images. To ensure that imaging can be performed at the lowest overall pulse power possible, it is not only important to have a high-quality (i.e., low-threshold and homogeneous) nanolaser sample, but it is also crucial to avoid undersampling. The voxel size used in this measurement was 2.20 µm in $(x,\ y)$ and 1 µm in z, which means that the images were slightly undersampled. Therefore, some nanolasers were likely positioned in a way that did not permit exciting them with the full pulse energy at any pixel of the scan, which would also explain the spread in observed degradation. The correct sampling interval corresponds to a pixel size approximately equal to either half the size of the object, or half the optical resolution, whichever is larger. E.g., for a horizontally oriented nanodisk laser ($d = 2$ µm, $h = 186$ nm), the ideal pixel size would be $\sim$1 µm in $(x,\ y)$, which is half the disk diameter, and 0.5 µm in z, which follows from the theoretical resolution of the CHSI system according to Equation 2.33. Of course, the real measurement scenario is more complex, because, depending on the orientation of the disk with respect to the pump, Equation 2.36 may apply, and disks can be arbitrarily rotated, too. Additionally, imperfections in the optical setup can compromise the optical resolution. Therefore, it was typically empirically confirmed that nanodisk lasers spanned two pixels in each spatial dimension, and, if this was the case, this was taken as an indication of sufficient sampling.

In the next section, a brief discussion of some observations from two-photon CHSI is provided. 2P-CHSI of nanodisk lasers could be performed in both the home-built setup (Figure 4.20a) and the Leica commercial setup (Figure 4.20b). As can be seen in both panels of Figure 4.20, some spectra appear broadened with a small shoulder emerging on the left side of the peak. It already could be seen during earlier studies of single- and two-photon excitation that the two-photon excited lasing peaks broaden more quickly above the lasing threshold (e.g., compare Figure 2.10 (1P) and Figure 3.5 (2P)), which is likely another consequence of the quadratic dependence of the excitation density in the QWs on the pump power under two-photon excitation.

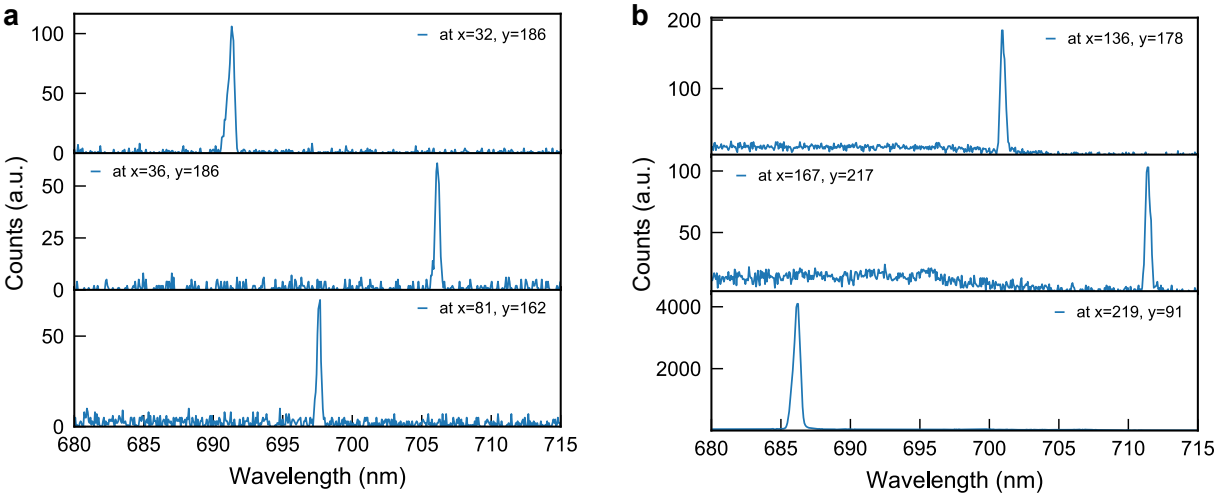

Fig. 4.20. Representative spectra of semiconductor nanodisk lasers in 2P-CHSI. a, Acquired on the home-built setup and **b,** on the modified Leica confocal microscope.

To acquire high-quality two-photon datasets, it is therefore even more important to have a very homogenous nanodisk laser sample with a small spread in lasing threshold, given that the range of optimal pulse energies (i.e. above the lasing threshold and below causing broadening) is reduced compared to single-photon excitation. Additionally, due to the high sensitivity of pulse energy along z, it is challenging to obtain 2D 2P-CHSI images of a sample that is not perfectly flat, given that any inhomogeneity in the $z-$position leads to stark intensity fluctuations that can not easily be compensated by excess excitation energy due to the risk of damaging the nanodisk lasers. Therefore, 2P-CHSI of nanodisk lasers is, as one might have expected, much better suited for the acquisition of high-resolution $z-$stacks.

In general, CHSI is subject to similar trade-offs as fluorescence confocal microscopy: Measurements with both large FOVs and high spectral resolution require a large number of pixels or voxels, and thereby decrease the scan speed. Also, in some cases, like faster scans or images with the closed pinhole, additional excitation energy is required to ensure sufficient signal brightness, which might then also increase the risk for photodamage. The quality of the acquired spectra was the main priority for setup development, and it remained excellent for the different measurement settings and engineering choices demonstrated in this chapter, but such high-resolution spectra have the downside of creating a large volume of data. Given that the image data is held in the RAM during the measurement, the instrument PC was upgraded to have 96 GB of RAM available, but still, long-term measurements required pausing the scan to export the data to the persistent storage and then restarting the measurement. The amount of data generated can be reduced by reading out only a portion of the detector, in cases where a smaller measurement bandwidth is sufficient (or a lower spectral resolution, in which case the 300 $\frac{\text{lines}}{\text{mm}}$ grating was used, and the emission bandwidth of the micro- and nanolasers spanned a smaller part of the detector).

While some of these limitations are dictated by the hardware used here, like the 175 Hz scan rate of the galvos on the home-built setup, or the 125 kHz spectral acquisition, many of the limitations and trade-offs discussed above can be addressed by making use of the high flexibility, particularly of the home-built setup. As demonstrated in this chapter, the excitation and collection optics can be adapted to tune the spatial resolution, enabling both very precise localisation of micro- and nanolasers, as well as larger voxel sizes for high speed measurements, like the 58 s scan times per $z-$stack for a measurement that will be presented in Section 5.1. Due to the speed limitation given by the 'fast-axis' (x) galvo, the highest measurement speed can be obtained by imaging rectangular FOVs with fewer pixels along the 'slow axis' (y), as e.g. demonstrated in Section redacted. Additionally, a large flexibility on the excitation side was demonstrated here, which allows optimising parameters such as pump repetition rate, penetration depth, and spatial resolution to the demands of the measurement. With this, an approximately 50-fold increase in speed for a large $z-$stack has been achieved as compared to previous implementations of CHSI for nanolaser readout[7]. As shown in the next chapter, this is particularly relevant for microlaser-based refractive index sensing in dynamically changing environments. Additionally, the investigation of stability and the operation in wavelength ranges with minimum tissue damage have allowed long-term measurements in biological samples, such as the 3-day cell tracking experiment with nanodisk lasers that is discussed in Section 5.3.

5 High-Throughput applications of bio-integrated microlasers

Results discussed in Sections 5.1 and 5.3 were published as part of the following publication: Titze, V. M. et al. Hyperspectral Confocal Imaging for High-Throughput Readout and Analysis of Bio-Integrated Microlasers. *Nature Protocols* **19**, 928–959 (2024)[2]. The content of these sections therefore contains data and results also presented in the aforementioned publication.

In this chapter, various application examples of CHSI of micro- and nanolasers will be presented. For initial experiments, an important part of these measurements was further development and application-specific optimisation of the imaging routines. Therefore, the optimisation of imaging parameters will be discussed in more detail in these sections. Following successful demonstrations of both high-speed and long-term measurements, CHSI was then also used for measurements in more extensive and complex biological environments such as 3D cell culture models and small animals. Here, the flexible imaging combined with high-throughput microlaser readout enabled to substantially scale up both main applications of bio-integrated microlasers, i.e. tracking and refractive index sensing.

5.1 High-throughput large-volume microlaser sensing

The first experiment highlighted here demonstrates the capabilities of the home-built microscope for fast 3D imaging, and for optimising the algorithms for automated data analysis of multimode lasing spectra. The goal of the measurement was to track the diffusion of a high-refractive index glucose solution through an extended 3D microlaser sample by monitoring the lasing spectra of PS microbeads and calculating the external refractive index in the immediate environment of each microlaser.

5.1.1 Experimental setup

For this experiment, a 3D matrix of agarose (1% w/v in DIW) containing PS microbead lasers was prepared such that in the middle of the sample, a small well was created that was surrounded by the agarose-microlaser matrix (Figure 5.1, see Appendix A.1 for details on the sample preparation). A large 3D FOV (1.6 mm × 1.6 mm × 0.8 mm, 300 × 300 × 20 voxels) was chosen at the edge of the agarose well. Hyperspectral confocal $z-$stacks of this volume were continuously recorded for 19 minutes, and at the beginning of the measurement, a glucose solution (40% w/v in DIW) was carefully pipetted into the well. Over the course of the 19 minutes, the glucose solution diffused through the agarose matrix, which caused a change in local refractive index due to replacing the DIW in the agarose by the high-index glucose solution.

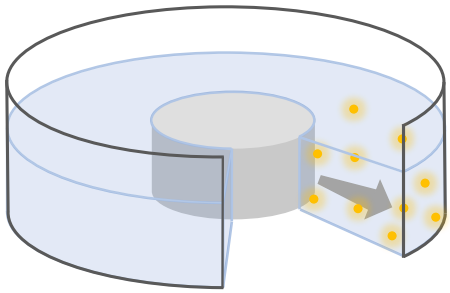

Fig. 5.1. Experimental setup for high-throughput sensing experiment. A 3D dispersion of microlasers (orange) was embedded in agarose (blue), and a high-refractive index glucose solution was left to diffuse from the centre well (grey).

Due to the large size of the PS microbeads, a coarse axial resolution - using the 10× objective and the 'open pinhole' fibre - was chosen, which allowed a comparably large step size of 40 µm in z. The pixel dwell time was set to 34 µs such that artefact-free high-speed imaging was possible, while the rate of data acquisition remained low enough to record the entire diffusion process with one continuous acquisition held in the RAM of the PC. Further, the amount of data generated was reduced by reading only the centre-most 680 pixels of the camera sensor. Using the 1200 $\frac{1}{\text{mm}}$ grating, an excellent spectral resolution of 0.06 nm was maintained, but the measurement bandwidth was reduced to $\sim$ 9.1 nm. Given the *FSR* of $\sim 4-5$ nm of the PS microbead lasers, this bandwidth typically allowed to measure four lasing peaks: two TE and two TM modes of consecutive angular mode number m. The combination of these settings allowed to record high-resolution spectra with a frame rate of 3.02 s and a scan time of 58 s per $z-$stack, which results in a 47-fold decrease in scan time compared to previous demonstrations of CHSI for nanolaser readout in extended 3D samples[7].

5.1.2 High-throughput refractive index fitting

Owing to the large number of recorded spectra over the course of the measurement (34.2×10^6), an automated workflow was developed for the data analysis and mathematical fitting. Chiefly, the functions designated for organising CHSI data and visualising the results[3] were combined with a previously developed optimisation algorithm, which employs the asymptotic expansion model (Section 2.1.5, Equation 2.25) for fitting the measured spectra to optimised physical parameters[9, 130].

First, all spectra in the data set were screened for actual lasing spectra (as opposed to fluorescence or background signal), which was evaluated on the presence of sharp and bright peaks. Then, the brightest peaks in the spectrum were fitted and their centre wavelengths were stored. Additionally, the spatial position and time step at which the spectrum was found, and the intensity of the largest lasing peak, were recorded. The resulting pre-processed data was stored as text files for subsequent analysis with the asymptotic expansion script. This algorithm first assigns the polarisation (TE or TM) to the measured peaks and then compares the experimental mode positions to the theoretical model through least-squares error minimisation. The radius r of the microlaser, the refractive index of the host n_h and the angular mode number m (compare equations 2.13 and 2.25) are free parameters of the optimisation, but in the actual implementation of the algorithm, the size is expressed as diameter d rather than the radius r to comply with conventions for commercial particles. The refractive index of the resonator n_r is treated as a known value in the model. The accuracy of these input parameters, i.e. the internal refractive index of the microlasers and the expected size range of the beads, was optimised by performing a designated calibration measurement such that the most accurate results for the external refractive index were obtained. This calibration entailed performing the measurement and fitting routine on a sample of microlasers in DIW. Due to the well-known refractive index of DIW, it was possible to set the external index as a known parameter in the model, and the internal index of the microlasers was left as a free parameter. With this, it was found that $n_r = 1.56977$ and the bounds of the microlaser size for the optimisation were $d = 15 - 18\,\mu\text{m}$.

Using the values obtained with the calibration measurement, and allowing values for n_h between 1.33 RIU and 1.4 RIU, the optimisation algorithm was applied to the diffusion data, and the fitted parameters and the residual error of the fit were added to each entry in the data text files. Using the data stored in these files, previously developed routines for 3D visualisation of the hyperspectral data were applied, but rather than encoding

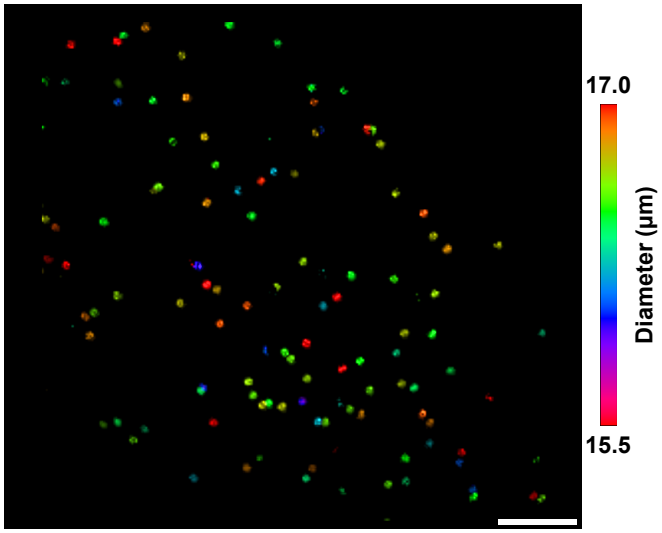

Fig. 5.2. Processed $x-y-$MIP of the 3D sample after 8 min, colour-coded according to the fitted diameters of all microlasers. Scale bar, 200 µm.

the wavelength of the lasing peaks, the optimised parameters like refractive index or microlaser diameter were visualised (Figure 5.2).

The diffusion gradient originating from the transport of the glucose solution through the agarose can clearly be seen in the refractive-index map (Figure 5.3a,b). The refractive index n of the 40% glucose solution in DIW is approximately 1.38 RIU, which was calculated from the following model for the dependence of the refractive index on the glucose concentration $C[\frac{\mathrm{g}}{\mathrm{l}}]$[131]:

$$n = 0.00011889C + 1.33230545. \tag{5.1}$$

Similarly, the refractive index of the agarose gel is concentration-dependent and is approximately 1.3344 RIU for the 1% agarose used here[132]. The refractive index maps obtained from the fitted lasing spectra show the highest refractive index near the edge between the agarose matrix and the well containing the glucose solution, e.g. an refractive index of ~ 1.35 RIU after 8 min in top right corner in the $x-y$ MIP (Figure 5.3a). The refractive index gradients at the time steps $t = 3\,\mathrm{min}$ and $t = 16\,\mathrm{min}$ are shown as side projections in Figure 5.3b.

Exemplary diffusion traces for the whole measurement duration, which were extracted from analysing individual microlasers, are displayed in Figure 5.3c. Due to the presence of some movement of the microlasers during the measurement, the refractive index traces were obtained by developing a tracking script that allowed following individual microlasers, which will be explained in more detail in the next section. The traces in Figure

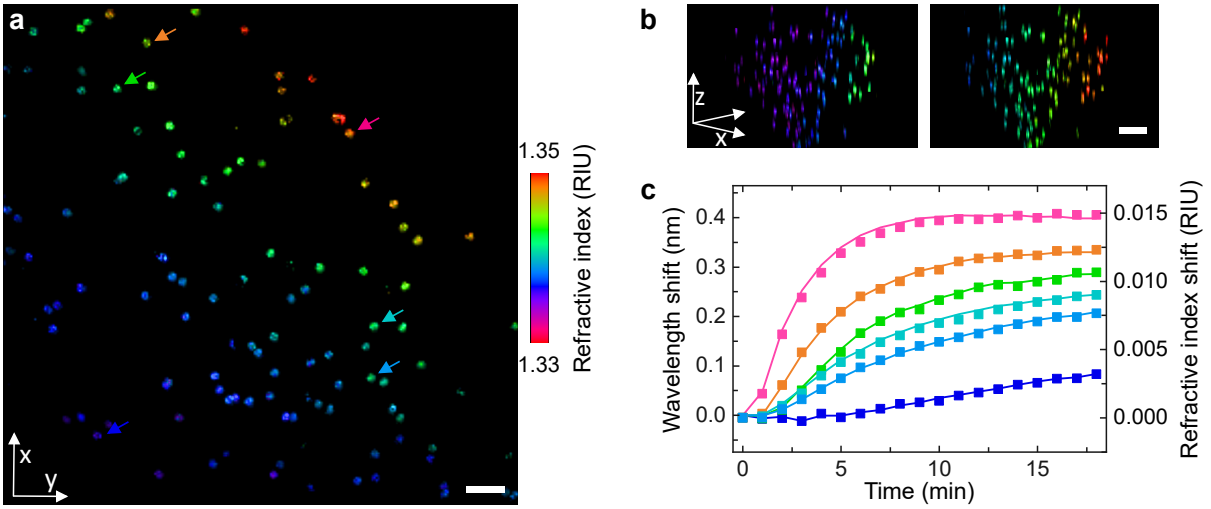

Fig. 5.3. Results for the fitted refractive index. **a,** Processed $x-y-$MIP of the 3D sample after 8 min, colour-coded according to the external refractive index. Scale bar, 100 µm. **b,** $x-z-$MIP of the refractive index map after 3 min (left) and 16 min (right). Scale bar, 200 µm. **c,** Traces of wavelength shifts of a TM mode (lines) from each of the 5 microlasers marked with an arrow in **a**, along with the shift of the fitted refractive index (symbols) for the same spectrum, over the duration of the entire measurement.

5.3 show the averaged fitted external refractive index from all pixels associated with an individual microlaser, and the initial value of external refractive index around each microlaser was subtracted from each trace. The subtracted values of initial refractive index were 1.335 ± 0.001 RIU, which is in good agreement with the literature value of the 1% agarose. The variations and the small discrepancy from the literature value could come from local concentration differences in the agarose, from evaporation of water during sample preparation, or from incorrect convergence of the mathematical fitting. The resulting traces exhibit a shape characteristic for a diffusion process, and the amount of refractive index change induced is in good agreement with other measurements of refractive index changes from the diffusion of glucose through agarose[133].

5.1.3 Combined tracking and sensing

As briefly mentioned above, developing automated tracking is essential for analysing the high-throughput sensing data, because - unless the microlasers remain completely stationary throughout the measurement - tracking their positions manually would be time-consuming and potentially a source of error or bias in the data analysis. Therefore, matching algorithms were developed here to identify spectra in the dataset which belong to the same microlaser. This assignment problem was applied i) to determine which

pixels in each $z-$stack are part of the same microlaser, and ii) to track the microlaser movement between adjacent time steps. In a first version, the size returned from the fitting algorithm (Figure 5.2) was used as a unique tag, and spectra with a size difference below a given threshold were defined as originating from the same microlaser. However,

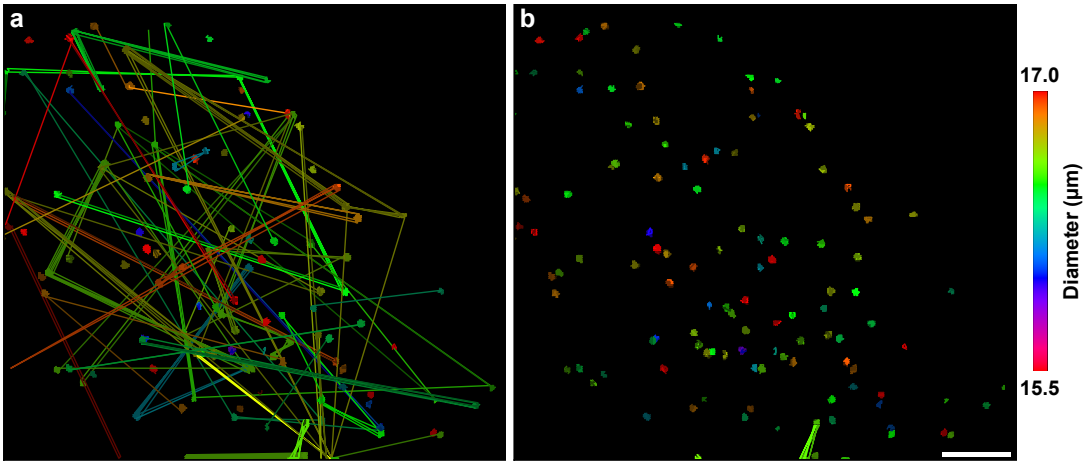

Fig. 5.4. Combined tracking and sensing. a, Plotting the objects that were tracked with an algorithm based only on comparing the microlaser diameter, where the lines connecting the microlasers represent incorrectly matched spectra. **b,** Visualised results from tracking based on the position and the fitted microlaser diameter. Scale bar, 100 µm.

it was found that the uncertainty of the fitted diameter ($\sim$ 2 nm) was larger than the bead-to-bead variation for the large sample size used here. This led to too many spectra being incorrectly identified as belonging to the same microlaser, i.e. false-positives, which is represented in the visualisation of the tracking results (Figure 5.4a) as lines connecting different microlasers. Decreasing the threshold used for assignment to a smaller size range, however, led to a large number of false-negatives, i.e. spectra from the same microlaser not being identified as such. Therefore, in addition to the microlaser diameter, the spatial information was taken into account, too, and the image was divided into segments in the $x-y-$plane where only spectra in the same segment with a similar fitted size were assigned to the same microlaser (Figure 5.4b). This substantially reduced the number of false-positives, but led to false-negatives where microlasers were positioned on the edges of the quadrants. Therefore, more advanced tracking algorithms were developed in further measurements, which entailed proper optimisation rather than a purely threshold-based assignment (Section 5.3). However, in this experiment, the share of correctly tracked microlasers was deemed sufficient to use these results for further analysis of the refractive index sensing results.

To determine the sensitivity of the microlasers, i.e. the wavelength shift per change in

external refractive index, the spectral position of a central lasing peak was taken from each spectrum and plotted against the fitted change in refractive index. Given that the peaks were chosen blindly, they could either be TE or TM peaks, and indeed, two distinct populations (Figure 5.5a, magenta and green) were found when calculating the sensitivity from the slope of a linear fit. A sensitivity cut-off of $S = 22\ \frac{\text{nm}}{\text{RIU}}$ was defined

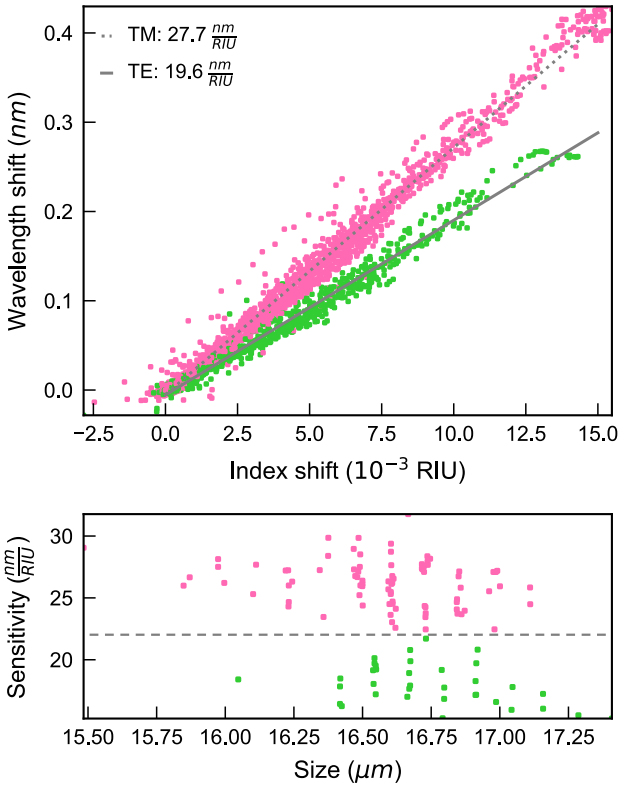

Fig. 5.5. Sensitivity of PS microbeads. a, Shift of a single lasing peak from each of the tracked microlasers vs measured refractive index shift, colour-coded according to mode assignment (pink - TM, green - TE). The lines represent the average parameters from linear fits to each trace (dashed grey, TM; solid grey, TE) to show the sensitivities of the respective mode families. **b,** Fitted sensitivities of all microlasers vs their fitted sizes. The dashed line represents the sensitivity cut-off of $S = 22\ \frac{\text{nm}}{\text{RIU}}$.

based on visual inspection of the two distributions, and peaks with a larger sensitivity were identified as TM modes, which are known to be less well-confined in the resonators and therefore are expected to exhibit higher sensitivities[134]. All sensing traces were fitted to a linear model individually, and lines showing the average sensitivities of the two populations were added to Figure 5.5a ($S_{TM} = 27.7\ \frac{\text{nm}}{\text{RIU}}$, dashed line; $S_{TE} = 19.6\ \frac{\text{nm}}{\text{RIU}}$, solid line). It was also expected that the electric field is less confined and the sensitivity is higher in microlasers with a smaller diameter and therefore a smaller angular mode

number m. To investigate this, the fitted sensitivities were plotted against the fitted size, again colour-coded according to the polarisation assignment (Figure 5.5b). Although a slight trend of decreasing sensitivity with increasing size is noticeable, there is also an unexpected discretisation in the fitted diameters that is not likely present in the actual sample, and therefore was deemed to be an artefact from the fitting algorithm. The significant disagreement of the fitted sizes with the nominal size of the microlaser batch, which was $d = 15.35\,\mu\text{m}$, also indicates a lack of accuracy of the fitting results. The fitting accuracy would not only benefit from adjustments in the optimisation algorithm itself, but also potentially from using a larger number of lasing peaks per resonator, which was not possible here due to the limited spectral bandwidth of the measurement. However, it should be noted that the calibration measurement, which used 6 rather than 4 lasing peaks, also exhibited a discretisation pattern. Lastly, implementing dispersion, i.e. a wavelength-dependence of the refractive index, would make the model more representative of the actual physical problem. This would not only improve the accuracy of determining the size of the microlasers and the refractive index around them, but also would likely increase the number of microlasers that can be tracked prior to encountering false-positives in the tracking algorithm.

The obtained sensitivity values of both mode families are a useful reference to correlate wavelength shifts to changes in external refractive index in future measurements. In addition, knowing the sensitivity also allows to define a limit of detection. Assuming a minimal resolvable wavelength shift of 1 pm from high-resolution spectroscopy and subsequent peak fitting[9], the corresponding resolvable refractive index change for the more sensitive TM modes is 3.6×10^{-5} RIU. This technique thus offers very high sensitivity and good spatial resolution due to the small footprint of the free-standing microlasers. The spatial resolution of CHSI in combination with developed tracking algorithms allowed robust automated localisation of microlasers. Further, this experiment demonstrated excellent time resolution and high-throughput, which was shown by measuring what is to our knowledge the fastest $z-$stack of microlaser spectra demonstrated so far. With this, refractive index information could be obtained from the spectra of 115 microlasers that were successfully tracked by the developed algorithm (Figure 5.4b).

5.2 Redacted

5.3 Cell tracking in a 3D epidermis model

To verify the capability of the CHSI setup for long-term measurements and for cell tracking in large biological samples, the migration of keratinocytes was tracked for 68 h during the formation of a 3D epidermis model. The present chapter will first introduce this epidermis model and discuss the motivation for cell tracking in this system (Section 5.3.1), before reporting on the experimental setup of the long-term CHSI measurements (Section 5.3.2). Lastly, further developments of the tracking algorithm and the results obtained from applying it to the keratinocyte tracking data will be discussed in Section 5.3.3.

5.3.1 3D model of keratinocyte stratification

The epidermis is composed of multiple layers as sketched in Figure 5.6a, where the bottom layer (Stratum basale) is comprised of proliferating keratinocytes that differentiate as they migrate upward and eventually form the skin barrier (Stratum corneum)[135, 136]. The process of stratification and keratinocyte differentiation is regulated by Calcium; therefore, switching a cell culture of primary keratinocytes from a low-Ca^{2+} to a high-Ca^{2+} environment allows studying the stratification in a controlled manner. This epidermis model was implemented by our collaborators as a model for stratifying epithelia, which

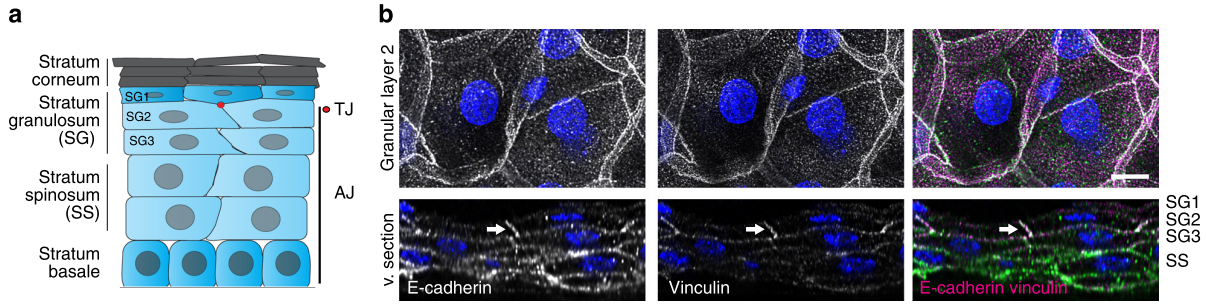

Fig. 5.6. Structure of epidermal layers. a, Schematic of the multi-layered epidermal structure. **b,** Immunofluorescence analysis of a whole-mounted tissue section the epidermis of newborn mouse. Scale bar, 10 µm. Reproduced from [137].

allows investigating factors driving the formation of intracellular junctions including tight junctions (TJ) and adherens junctions (AJ), both in a cell-culture setting and in whole-mounted tissue sections (Figure 5.6b)[137]. Generally, understanding what determines whether cells remain in the basal layer or initiate the upward migration and differentiation

remains an open question. Here, we use semiconductor nanolasers for tracking the 3D migration of individual cells during this stratification process. Owing to the large labelling capabilities, small footprint, and low thresholds of nanolasers, this approach is expected to provide more accurate positional information and reduced photodamage compared to alternative methods such as continuous confocal imaging of stained cells.

5.3.2 Experimental setup for long-term tracking

The objective of this experiment was to track the migration of cells in 3D for up to 3 days, which is the expected duration of the formation of the epidermis model after initiating stratification by switching to a high-Ca^{2+} medium. Additionally, a control sample was kept in a low-Ca^{2+} environment, and both samples were monitored simultaneously using the automated motorised stage, which continuously moved the scanned FOV back and forth between the samples after each z-stack. 24 h prior to starting the measurement, both samples were incubated with the nanolasers to initiate their uptake by the cells (see Appendix A.1 for cell culture and nanolaser seeding methods).

Long-term hyperspectral imaging was performed on the home-built CHSI setup, where an on-stage incubator allowed to control the temperature and CO_2 concentration around the cell culture samples. Using the 25× objective, each scan field was acquired with a size of 0.48 mm × 0.48 mm × 40 µm and a voxel size of 1.3 µm × 1.3 µm × 1 µm. Due to the interest in accurate tracking of the cells in the axial direction, which corresponds to upward migration in the epidermis model, the 'closed pinhole' fibre was used for this experiment. Based on the results discussed in Section 4.3.3, nanolaser excitation was performed with the 642 nm pump laser at a pulse energy of 5 pJ and a repetition rate of 1 MHz, which was found to be the optimal balance of limiting nanolaser degradation and achieving high-throughput excitation. For each imaging iteration, 6 consecutive z-stacks of each sample were acquired, and then the data was exported and the measurement was restarted. Given that the amount of data that could be stored in the RAM of the measurement PC was again the limiting factor for the time of continuous acquisition before a restart was required, this was maximised by a reduction in scan speed (419 µs pixel dwell time) and by reading only the central 600 pixels of the sensor. To achieve sufficient spectral bandwidth to cover the expected emission range of the nanolasers, the $300\frac{\text{l}}{\text{mm}}$ grating was used. In this case, the low spectral resolution was sufficient, given that the peak position did not have to be resolved more accurately than the uncertainty due to the intrinsic shift of the lasing peak. With these setting, a total of ~ 8.5 h could be

stored in one continuous acquisition. In total, 8 iterations were performed, leading to a total measurement time of 68 h with a duration of 40 min per $z-$stack. The results from the 68 h tracking measurements will be shown in Section 5.3.3.

Immediately after finishing the last scan, the sample was fixed and stored for further analysis. To investigate the structure of the epidermis model and the positioning of the nanolasers, the sample was stained and fluorescence confocal imaging was performed on the Leica Stellaris. Figure 5.7 shows an area in the high-Ca^{2+} dish, where a multi-layer structure consisting of two layers can be seen. Presumably, the cell culturing conditions were not yet optimised, leading to the epidermis model not developing to the full multi-layer structure (Figure 5.6). This would also explain observations for the cells in the low-Ca^{2+} sample, which began to detach after 48 h. The low-Ca^{2+} medium, which is a less stable environment for these cells, prevents them from forming intracellular junctions, making them more sensitive to non-optimal conditions. Due to the poor health of the cells in this sample, it was not analysed further. Appropriate controls without nanolasers confirmed that nanolasers did not decrease cell viability. The high-Ca^{2+} sample, however, did not only show better survival of the cells, but importantly, also showed a homogeneous distribution of the nanolasers throughout the sample. To validate the 3D tracking of the

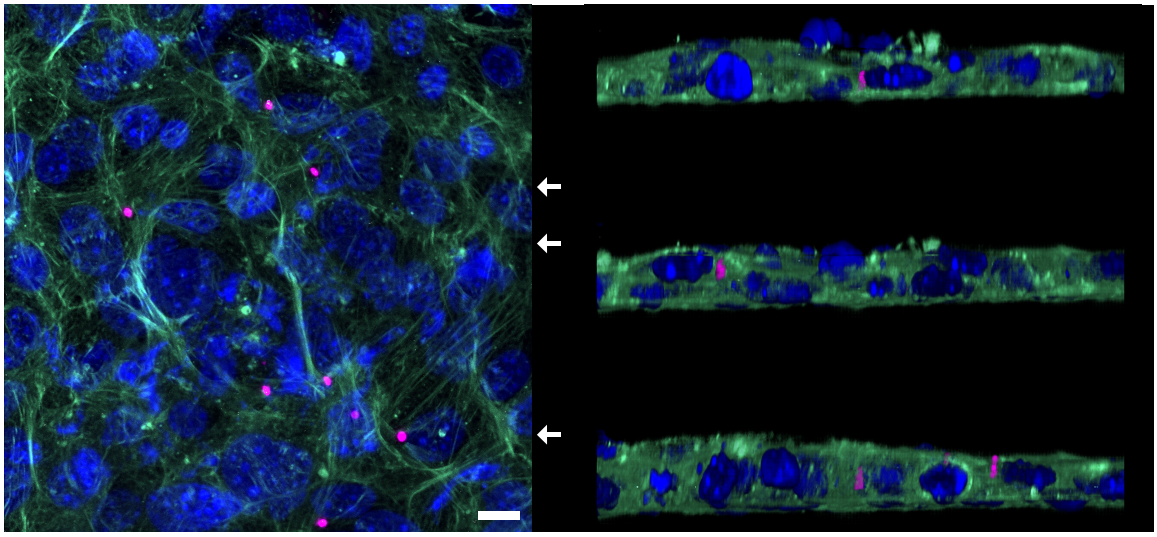

Fig. 5.7. Confocal image of 3D epidermis model with nanolasers. Left: $x-y-$MIP of the stratified epidermis model with intracellular nanolasers (magenta), stained for nuclei (Hoechst, blue) and F-actin (phalloidin, green). Scale bar, 10 µm. Right: Three $x-z-$MIPs taken from the sections that are indicated by white arrows in the $x-y-$MIP.

position of cells with nanolasers within the epidermis model, it was important to verify that the presence of the nanolasers did not affect the ability of cells to migrate upward. Indeed, the confocal imaging demonstrated that cells with nanolasers were present in

both layers of the model, which can be seen by comparing the cross-sectional MIPs of the sample (Figure 5.7, right side).

5.3.3 Tracking algorithm development and results

To compute trajectories of nanolasers over the course of the measurement, various approaches were developed and tested. The optimisation task of multi-object tracking is an example of what is known as a rectangular assignment problem, which means that two groups of objects, which can have different sizes, need to be matched pairwise[138]. One solution for this problem, the Jonker-Volgenant algorithm[139], has been implemented in the open-source scientific Python library SciPy[140]. This solution is based on computing a cost matrix C_{ij}, which describes the cost (comparable to an error value) of assigning objects i and j to each other. The goal of the algorithm is to minimise the total cost

$$\sum_i \sum_j C_{ij} X_{ij}, \tag{5.2}$$

where X_{ij} is a boolean matrix with value 1 for assigned objects and value 0 otherwise. The practical implementation of this algorithm only requires the cost matrix to be defined, which here was chosen to be

$$C_{ij} = \sqrt{\left(\frac{x_i - x_j}{w_0}\right)^2 + \left(\frac{y_i - y_j}{w_1}\right)^2 + \left(\frac{z_i - z_j}{w_2}\right)^2 + \left(\frac{\lambda_i - \lambda_j}{w_3}\right)^2}. \tag{5.3}$$

This equation represents a quasi-distance in the 4D space of the 3 spatial positions (x, y, and z) and the wavelength λ, which is similar to previous metrics used for tracking nanolasers[7]. The weights w_0 to w_3 can be set based on the expected movement or wavelength shift of the nanolaser, but also allow weighing the importance of the quantities on the total cost. This algorithm was developed and tested while working on the data sets presented in Section 4.3.3, and there, led to robust results allowing to track large populations of nanolasers and extract the stability statistics. A visualisation of a representative cost table is shown in Figure A.14. However, in these measurements, the nanolasers were stationary (apart from the small sample drift during the measurement), and yet, the weights required substantial sample-specific manual optimisation for the tracking to be successful.

Rather than optimising this approach further for the more complex scenario of tracking cellular migration, a suitable existing solution for both particle detection and tracking

was adapted. The open-source Python project Trackpy[141, 142] performs predictive particle tracking based on a previously developed algorithm by Crocker and Grier[143]. Trackpy is capable of handling the hyperspectral datasets by treating the wavelength-axis as a 4^{th} spatial dimension. One additional step of pre-processing the hyperspectral images to be compatible with the data format accepted by Trackpy was performed before running the 4D object detection and linking algorithms. Additional functions were written to extract and visualise the trajectories of the tracked microlasers with custom colour-coding (Figure 5.8). Although the multi-dimensional tracking algorithms were found to be

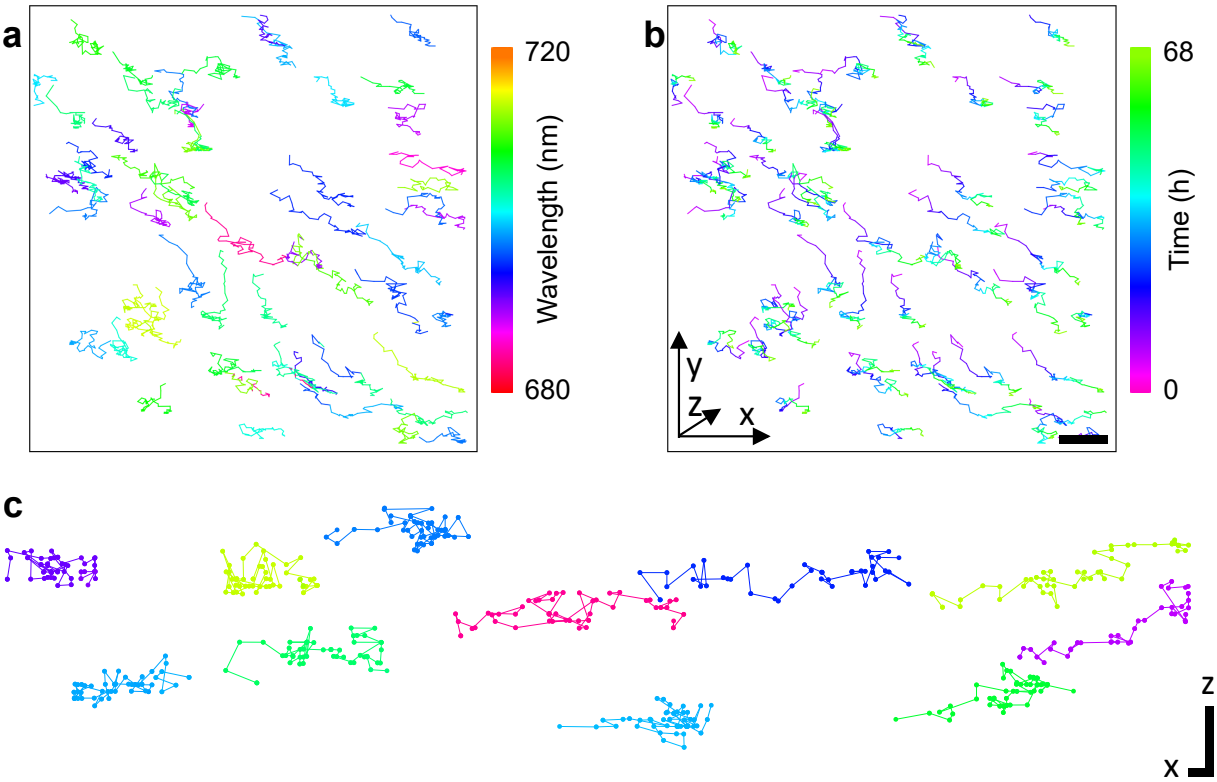

Fig. 5.8. Cellular migration in 3D epidermis model tracked with nanolasers. **a,** $x-y$ projection of migration trajectories of cells colour-coded by the wavelength of the nanolaser emission peak, and **b,** colour-coded according to time passed. Scale bar, 50 µm. **c,** $x-z$ projection of migration trajectories of a subset of cells colour-coded by emission wavelength. The trajectories were offset in z for clarity. Scale bar, 10 µm.

significantly slower and more prone to crashes than their 2D or 3D equivalents, ultimately, approximately 50 nanolasers were tracked across the majority of the measurement. During the first day of the measurement, most cells showed a pronounced lateral movement, which then slowed down, likely due to increased junction formation between neighbouring cells (Figure 5.8b). Some cells also showed upward migration of up to 10 µm: Figure 5.8c shows trajectories from randomly selected cells, which were purposefully offset in the z-direction

to show the traces relative to their respective starting position. Due to the much greater overall movement in x as compared to z, an anisotropic scaling was applied to panel c, as denoted by the 2D scale bar. The magnitude of this upward movement is in good agreement with the height of the final epidermal structure (compare Figure 5.7).

Despite this overall positive result, it should be noted that the upward migration is barely distinguishable from the general noise in the migration trace, which originated from multiple factors including sample slant, drift, and potentially movement of the nanolaser within the cell. Therefore, distinguishing between adjacent cell layers would require some further optimisation of the microscopy and data analysis, namely stabilisation of the stage and drift correction of the data set. However, in the full epidermis model, which is expected to have a final height that is $2-3\times$ larger than in this measurement, the localisation capabilities demonstrated here are expected to be sufficient to discriminate between the base layer and the upper layers in the model.

In this measurement, the excitation of nanolasers with the 642 nm pump laser (Section 3.1) was combined with high-resolution, long-term CHSI measurements, allowing to obtain intracellular lasing spectra for three consecutive days without noticeable damage to either the nanolasers or the cell culture. With this, the feasibility of long-term cell tracking was demonstrated, and basic data processing routines for the analysis of this tracking data were developed. Further optimisation of hardware and software, and an improvement in experimental cell culture conditions, are expected to further improve this technique and thus make it a powerful tool for non-invasive measurements of 3D cellular migration.

5.4 Redacted

6 Conclusions and Outlook

In this work, microscopy methods for optical pumping of nano- and microlasers and collection of their emission spectra in a spatially resolved manner were developed. Central to these efforts was the construction of a high-speed, high-resolution confocal hyperspectral imaging setup. This microscope along with its variations has proven its capability of acquiring high-resolution lasing spectra of excellent quality in different measurement settings of vastly different temporal and spatial scales. Demonstrations shown here range from high-speed hyperspectral measurements at 25 fps to long-term measurements over multiple days, and from sub-cellular spatial resolution to whole animal studies. Strategic material optimisations of the nanolaser material and investigations of excitation schemes have added further flexibility to the pumping process, which is an important constituent of the CHSI setup, and have allowed optical pumping of nanolasers at wavelengths particularly beneficial for operation in deep-tissue. In addition to the technical developments, which will be reflected on in Section 6.1, this has enabled a range of interesting high-throughput applications of bio-integrated microlasers. The insights gained from these measurements will be summarised in Section 6.2.

6.1 High-throughput microlaser readout

In Chapter 4, a comprehensive overview of the performance of the CHSI setup was provided. There, it was shown that common trade-offs of confocal imaging could be addressed effectively by allowing maximum flexibility to optimise the imaging conditions through the use of accessible free-space optics, and by offering variations of the setup including the integration with commercial confocal microscopy. This CHSI setup and its variations provide effective solutions for reliable high-throughput spectral readout, and the setup can be adapted to satisfy the demands of many different applications. Rather than repeating the details of the successful development of hardware and software for this microscope, the following discussion highlights areas where potential for further improvements to the imaging setup was identified.

Although the speed of high-resolution CHSI was greatly improved in this work compared to previous implementations, further increase in scan speed would be highly interesting

for certain applications, and moderate improvements would be possible simply by replacing some hardware components. Using a resonant scanner for the fast (x) scanning in the home-built setup, and upgrading the camera to the very latest model, which could allow measurements at 250 kHz without compromising the dynamic range, are accessible modifications expected to allow a two-fold improvement in speed. Even with these improvements, the rate of spectral acquisition is likely to remain a bottleneck for greater improvements in measurement speed.

Paragraph redacted.

There are additional suggestions for improvement of the CHSI setup that do not require a fundamental change in the imaging approach. One important next step that was not implemented here simply due to time constraints addresses the bottleneck of data storage in the RAM of the measurement computer. Storing of the entire measurement in the RAM does not only limit the duration and/or resolution of measurements, but also poses an increased risk for data loss. A better alternative would be to implement buffer cycling, which means that only a subset of the camera buffers are stored in the RAM at a given time. This allows to already save the previously acquired buffers in the permanent storage while continuing to fill the remaining buffers with new data, until the already saved buffers can be overwritten with new data. Implementing this is possible with the hardware used in this work, but requires substantial changes to the camera software. The example code that was heavily used for building the camera user interface does not employ buffer cycling; therefore, a more extensive software development project could address this limitation.

For deep-tissue applications, it is highly advantageous that the spectral information of the microlaser emission is not affected by strongly scattering media[9], but in highly scattering samples, the spatial information is mainly lost[10]. This challenge greatly benefits from two-photon excitation, which provides better tissue penetration depth and intrinsically improves the axial resolution on the excitation side. This would also allow to remove the confocal pinhole in the collection path such that non-ballistic photons also reach the detector, as often done in multi-photon imaging. However, reading the non-descanned signal on a similar spectroscopy module as the one used here, poses additional optical engineering challenges, given that the étendue of the collected signal is linked to the spectral resolution, and is also constrained by the finite height of the pixels on the line-scan camera needed for the high-speed readout. Although these approaches are generally promising, multi-photon excitation could not be demonstrated for all types of microlasers used in this work; rather, it was only successful so far for semiconductor nanodisk lasers although at the cost of greater risk of damaging the devices. An interesting alternative for

operating microlasers at much greater depths might be to combine the spectral readout of microlasers with emerging techniques of adaptive optics, for example by wavefront shaping of the excitation to focus in deep-tissue far beyond the transport mean free path length[144, 145].

In CHSI measurements of semiconductor nanodisk lasers, particularly when working with two-photon excitation, further upgrades to the CHSI setup are suggested to improve the reliability of pumping nanolasers without damaging them. Importantly, the shape of the excitation beam and the pixel size used during the measurement need to be tuned better to the needs of a specific sample. In many nanolasers measurements, an undersampling in z (which includes 2D imaging of a thicker sample, e.g. in the redacted Chapter) was compensated by excess excitation energy, which greatly increased the risk of photodamage to the lasers, particularly when operating in the two-photon regime. In samples with slow dynamics, such as the cell tracking experiment, this problem was avoided by adding additional z-planes; but in highly dynamic samples, this option is typically not feasible at the measurement speeds that are currently possible. Therefore, a good alternative is beam shaping, such that the excitation energy is distributed more evenly along z. This would alleviate the selectivity to narrow z-planes, without increasing the risk for photodamage, albeit of course at the cost of axial resolution. Additional factors such as pulse duration of the pump laser, especially for multi-photon excitation, should also be investigated to check how damage to the nanolasers can be kept at a minimum.

Lastly, further work on investigating the effect of various excitation parameters would be helpful to make more informed choices on which pumping scheme is preferable for a given measurement. While the demonstration of CHSI with many different pump lasers offers many options for optimisation, a thorough investigation of how settings such as pulse energy and repetition rate of the pump affect the signal and the stability of nanolasers has so far only been performed for the 642 nm pump laser. Particularly for two-photon excitation, where measurements sometimes led to pulse broadening and even damage of the resonators, this would add important knowledge to inform future choices of measurement parameters.

6.2 Applications of microlasers in biology and ecology

In Chapter 5, four application examples of CHSI were provided, which included two projects working with polymer microbead lasers and two experiments with semiconductor nanodisks. This showcased the reliable performance and flexibility of the setup in the context of a range of highly versatile biological applications. These examples also highlighted the capability of CHSI measurements to scale up both main uses of bio-integrated microlasers, namely tracking and refractive index sensing. To achieve practical usefulness of these techniques, further steps need to be taken to optimise the nanolasers and the CHSI optics. Additionally, some improvements are suggested to the data analysis routines and the application-specific processing algorithms.

An important aspect of reliable nanolaser excitation pertains to the quality of the semiconductor nanodisk laser sample. Possible next steps include the optimisation of the fabrication protocol to achieve batches with more uniform quality, leading to homogeneously low lasing thresholds. This would predominantly address the problem that exciting a large share of nanolasers in the sample will already cause photodamage to some of the devices, thereby inducing blue-shifts of the lasing wavelength or even destroying the nanolasers. Additionally, establishing a surface passivation routine[146, 147] to stabilise the lasing wavelength is expected to improve the reliability of the tracking algorithm for nanodisk lasers, and lead to more accurate sensing measurements without the need of a baseline subtraction.

For PS microbead lasers, the main limitation for both tracking and sensing is currently software-based. The discretisation in the fitted sizes and the constant offset between the fitted diameters and the nominal sample size distribution are indicative that further work on the refractive index fitting workflow is necessary. Improvements to both the underlying mathematical formalism, e.g. by implementing dispersion in the model, and to the optimisation algorithm are required to eliminate errors in the convergence. The elimination of the discretisation is expected to greatly enhance the tracking capabilities by removing the artificial grouping of the fitted size, which is the parameter used as a label for tracking, around discrete values. Additionally, the implementation of more reliable convergence and a more representative mathematical model are important for obtaining accurate refractive index information. In previous work, the precision of the relative change in refractive index was substantially improved by performing a multi-step fitting workflow, where in the second step, the microlaser diameter was set to a fixed value, which avoids the problem of shifts in diameter and external refractive index compensating for

one-another[9]. However, in high-throughput measurements, an automation of the fitting workflow is highly desirable, which is much more readily implemented with an algorithm converging reliably without additional optimisation at each iteration. Therefore, an improved model in conjunction with a more robust optimisation algorithm is expected to lead to substantial improvements. Particularly the integration of this analysis with CHSI is very promising for realising combined tracking and sensing applications, capitalising on the high information density of the multi-mode lasing spectra.

For single-mode resonators such as semiconductor nanodisk lasers, combined tracking and sensing is possible in configurations with continuous imaging. This was seen in Section 5.3, where the developed algorithms were able to track nanolasers despite their intrinsic wavelength shifts. This sensing capability provides an important advantage, as compared to purely image-based cell tracking with bright and well-localised small intracellular particles. Another key advantage of nanolaser-based tagging and tracking is that it allows single-cell specificity across various high-throughput platforms such as imaging methods like the one shown here, and complimentary techniques such as flow cytometry[148].

While the modifications and improvements suggested here would further add to the reliability of measurements and data analysis, it was shown that the CHSI setup already performs very well under many different experimental conditions. Likely, future work can focus on developing novel applications of CHSI of bio-integrated microlasers and perform further improvements to hardware and software on an application-specific case-by-case basis.

Bibliography

1. Titze, V. M., Caixeiro, S., Di Falco, A., Schubert, M. & Gather, M. C. Red-Shifted Excitation and Two-Photon Pumping of Biointegrated GaInP/AlGaInP Quantum Well Microlasers. *ACS Photonics* **9,** 952–960 (2022).
2. Titze, V. M. *et al.* Hyperspectral confocal imaging for high-throughput readout and analysis of bio-integrated microlasers. *Nature Protocols* **19,** 928–959 (2024).
3. Titze, V. M., Caixeiro, S., Schubert, M. & Gather, M. C. *GatherLab/sphyncs* (DOI: 10.5281/zenodo.8121099, 2023).
4. Schubert, M. *et al.* Lasing within Live Cells Containing Intracellular Optical Microresonators for Barcode-Type Cell Tagging and Tracking. *Nano Letters* **15,** 5647–5652 (2015).
5. Humar, M. & Yun, S. H. Intracellular microlasers. *Nature Photonics* **9,** 572–576 (2015).
6. Schubert, M. *et al.* Lasing in Live Mitotic and Non-Phagocytic Cells by Efficient Delivery of Microresonators. *Scientific Reports* **7,** 1–9 (2017).
7. Martino, N. *et al.* Wavelength-encoded laser particles for massively multiplexed cell tagging. *Nature Photonics* **13,** 720–727 (2019).
8. Li, X. *et al.* In vivo tracking of individual stem cells labeled with nanowire lasers using multimodality imaging. *Biomedical Optics Express* **13,** 4706 (2022).
9. Schubert, M. *et al.* Monitoring contractility in cardiac tissue with cellular resolution using biointegrated microlasers. *Nature Photonics* **14,** 452–458 (2020).
10. Kavčič, A. *et al.* Deep tissue localization and sensing using optical microcavity probes. *Nature Communications* **13,** 1269 (2022).
11. Toropov, N. *et al.* Review of biosensing with whispering-gallery mode lasers. *Light: Science & Applications* **10,** 42 (2021).
12. Foreman, M. R., Swaim, J. D. & Vollmer, F. Whispering gallery mode sensors. *Advances in Optics and Photonics* **7,** 168 (2015).
13. Su, J. Label-Free Biological and Chemical Sensing Using Whispering Gallery Mode Optical Resonators: Past, Present, and Future. *Sensors* **17,** 540 (2017).

14. Lv, Z. *et al.* Intracellular near-Infrared Microlaser Probes Based on Organic Microsphere-SiO2 Core-Shell Structures for Cell Tagging and Tracking. *ACS Applied Materials and Interfaces* **10,** 32981–32987 (2018).

15. Tang, S. K. *et al.* A multi-color fast-switching microfluidic droplet dye laser. *Lab on a Chip* **9,** 2767–2771 (2009).

16. Richter, D., Marinčič, M. & Humar, M. Optical-resonance-assisted generation of super monodisperse microdroplets and microbeads with nanometer precision. *Lab on a Chip* **20,** 734–740 (2020).

17. Fikouras, A. H. *et al.* Non-obstructive intracellular nanolasers. *Nature communications* **9,** 4817 (2018).

18. Tang, S.-J. *et al.* Laser particles with omnidirectional emission for cell tracking. *Light: Science & Applications* **10,** 23 (2021).

19. Liao, Q. *et al.* Perovskite microdisk microlasers self-assembled from solution. *Advanced Materials* **27,** 3405–3410 (2015).

20. Gargas, D. J. *et al.* Whispering gallery mode lasing from zinc oxide hexagonal nanodisks. *ACS Nano* **4,** 3270–3276 (2010).

21. Chen, Y. C. *et al.* Monitoring Neuron Activities and Interactions with Laser Emissions. *ACS Photonics* **7,** 2182–2189 (2020).

22. Wu, X. *et al.* Nanowire lasers as intracellular probes. *Nanoscale* **10,** 9729–9735 (2018).

23. Hua, B., Motohisa, J., Kobayashi, Y., Hara, S. & Fukui, T. Single GaAs/GaAsP Coaxial Core-Shell Nanowire Lasers. *Nano Letters* **9,** 112–116 (2009).

24. Feng, C. *et al.* Organic-Nanowire-SiO2 Core-Shell Microlasers with Highly Polarized and Narrow Emissions for Biological Imaging. *ACS Applied Materials and Interfaces* **9,** 7385–7391 (2017).

25. Lee, S. S., Kim, J. B., Kim, Y. H. & Kim, S.-H. Wavelength-tunable and shape-reconfigurable photonic capsule resonators containing cholesteric liquid crystals. *Science Advances* **4,** 8276–8298 (2018).

26. Humar, M. & Muševič, I. 3D microlasers from self-assembled cholesteric liquid-crystal microdroplets. *Optics Express* **18,** 26995 (2010).

27. Cho, S., Humar, M., Martino, N. & Yun, S. H. Laser Particle Stimulated Emission Microscopy. *Physical Review Letters* **117** (2016).

28. Svelto, O. *Principles of lasers* 1–620 (Springer US, Boston, MA, 2010).

29. Csele, M. *Fundamentals of Light Sources and Lasers* (Wiley, 2004).

30. Hill, M. T. & Gather, M. C. Advances in small lasers. *Nature Photonics* **8,** 908–918 (2014).

31. Kuehne, A. J. & Gather, M. C. Organic Lasers: Recent Developments on Materials, Device Geometries, and Fabrication Techniques. *Chemical Reviews* **116,** 12823–12864 (2016).

32. Dannenberg, P. H. *et al.* Multilayer Fabrication of a Rainbow of Microdisk Laser Particles Across a 500 nm Bandwidth. *ACS Photonics* **8,** 1301–1306 (2021).

33. Blood, P. in *Semiconductor Lasers* 3–55 (Elsevier, 2013).

34. Hastie, J., Calvez, S. & Dawson, M. in *Semiconductor Lasers* 341–393 (Elsevier, 2013).

35. Ozasa, K., Yuri, M., Tanaka, S. & Matsunami, H. Effect of misfit strain on physical properties of InGaP grown by metalorganic molecular-beam epitaxy. *Journal of applied physics* **68,** 107–111 (1990).

36. Nomura, I., Kishino, K., Kikuchi, A. & Kaneko, Y. 600-nm-Range GaInP/AlInP Strained Quantum Well Lasers Grown by Gas Source Molecular Beam Epitaxy. *Japanese Journal of Applied Physics* **33,** 804–810 (1994).

37. Arakawa, Y. & Yariv, A. Quantum well lasers–Gain, spectra, dynamics. *IEEE Journal of Quantum Electronics* **22,** 1887–1899 (1986).

38. Miller, D. A. B. in *Quantum Dynamics of Simple Systems* 239–266 (CRC Press, 2020).

39. Zhang, Z. *et al.* Visible submicron microdisk lasers. *Applied Physics Letters* **90,** 3–5 (2007).

40. McCall, S. L., Levi, A. F., Slusher, R. E., Pearton, S. J. & Logan, R. A. Whispering-gallery mode microdisk lasers. *Applied Physics Letters* **60,** 289–291 (1992).

41. Samuel, I. D., Namdas, E. B. & Turnbull, G. A. How to recognize lasing. *Nature Photonics* **3,** 546–549 (2009).

42. Bour, D. P. *et al.* 610-nm Band AlGaInP Single Quantum Well Laser Diode. *IEEE Photonics Technology Letters* **6,** 128–131 (1994).

43. Ma, R. M. & Oulton, R. F. Applications of nanolasers. *Nature Nanotechnology* **14,** 12–22 (2019).

44. Ning, C.-Z. Semiconductor nanolasers and the size-energy-efficiency challenge: a review. *Advanced Photonics* **1,** 1 (2019).

45. Rayleigh, L. CXII. The problem of the whispering gallery. *The London, Edinburgh, and Dublin Philosophical Magazine and Journal of Science* **20,** 1001–1004 (1910).

46. Mie, G. Beiträge zur Optik trüber Medien, speziell kolloidaler Metallösungen. *Annalen der Physik* **330,** 377–445 (1908).

47. Debye, P. Der Lichtdruck auf Kugeln von beliebigem Material. *Annalen der Physik* **335,** 57–136 (1909).

48. Chiasera, A. *et al.* Spherical whispering-gallery-mode microresonators. *Laser and Photonics Reviews* **4,** 457–482 (2010).

49. Chin, M. K., Chu, D. Y. & Ho, S.-T. Estimation of the spontaneous emission factor for microdisk lasers via the approximation of whispering gallery modes. *Journal of Applied Physics* **75,** 3302–3307 (1994).

50. Sedlmeir, F. *et al.* Polarization-Selective Out-Coupling of Whispering-Gallery Modes. *Physical Review Applied* **7,** 024029 (2017).

51. Betzig, E. & Chichester, R. J. Single Molecules Observed by Near-Field Scanning Optical Microscopy. *Science* **262,** 1422–1425 (1993).

52. Tenopala-Carmona, F. *et al.* Orientation distributions of vacuum-deposited organic emitters revealed by single-molecule microscopy. *Nature Communications* **14,** 6126 (2023).

53. Senthil Murugan, G., Wilkinson, J. S. & Zervas, M. N. Selective excitation of whispering gallery modes in a novel bottle microresonator. *Optics Express* **17,** 11916 (2009).

54. Lin, Z. H. *et al.* Impact of Plasmonic and Dielectric Substrates on the Whispering-Gallery Modes in Self-Assembled Fluorescent Semiconductor Polymer Microspheres. *Nano Letters* (2023).

55. Lei, J., Hu, A., Wang, Y. & Chen, P. A method for selective excitation of Ince-Gaussian modes in an end-pumped solid-state laser. *Applied Physics B* **117,** 1129–1134 (2014).

56. Schepers, F., Bexter, T., Hellwig, T. & Fallnich, C. Selective Hermite–Gaussian mode excitation in a laser cavity by external pump beam shaping. *Applied Physics B* **125,** 75 (2019).

57. Bachelard, N., Gigan, S., Noblin, X. & Sebbah, P. Adaptive pumping for spectral control of random lasers. *Nature Physics* **10,** 426–431 (2014).

58. Kavokin, A. V., Baumberg, J. J., Malpuech, G. & Laussy, F. P. *Microcavities* (Oxford University PressOxford, 2017).

59. Purcell, E. M. Spontaneous emission probabilities at radio frequency. *Physical Review* **69,** 681 (1946).

60. Rice, P. R. Photon statistics of a cavity-QED laser : A comment on the laser – phase- transition analogy. *Physical Review A* **50** (1994).

61. Bjork, G. & Yamamoto, Y. Analysis of semiconductor microcavity lasers using rate equations. *IEEE Journal of Quantum Electronics* **27,** 2386–2396 (1991).

62. Jiang, X. F., Zou, C. L., Wang, L., Gong, Q. & Xiao, Y. F. *Whispering-gallery microcavities with unidirectional laser emission* 2016.

63. Diez, I., Krysa, A. & Luxmoore, I. J. Inverse Design of Whispering-Gallery Nanolasers with Tailored Beam Shape and Polarization. *ACS Photonics* (2022).

64. Cao, H. & Wiersig, J. Dielectric microcavities: Model systems for wave chaos and non-Hermitian physics. *Reviews of Modern Physics* **87,** 61–111 (2015).

65. Schiller, S. Asymptotic expansion of morphological resonance frequencies in Mie scattering. *Applied Optics* **32,** 2181 (1993).

66. Dannenberg, P. H. *et al.* Droplet microfluidic generation of a million optical microparticle barcodes. *Optics Express* **29,** 38109 (2021).

67. Liapis, A. C. *et al.* Conformal Coating of Freestanding Particles by Vapor-Phase Infiltration. *Advanced Materials Interfaces* **7** (2020).

68. Yu, D. *et al.* Whispering-gallery-mode sensors for biological and physical sensing. *Nature Reviews Methods Primers* **1,** 83 (2021).

69. Pirnat, G., Marinčič, M., Ravnik, M. & Humar, M. Quantifying local stiffness and forces in soft biological tissues using droplet optical microcavities. *Proceedings of the National Academy of Sciences* **121** (2024).

70. Oki, O. *et al.* FRET-mediated near infrared whispering gallery modes: Studies on the relevance of intracavity energy transfer with Q-factors. *Materials Chemistry Frontiers* **2,** 270–274 (2018).

71. Yuan, Z., Wang, Z., Guan, P., Wu, X. & Chen, Y. C. Lasing-Encoded Microsensor Driven by Interfacial Cavity Resonance Energy Transfer. *Advanced Optical Materials* **8** (2020).

72. Wang, Y. *et al.* Demonstration of intracellular real-time molecular quantification via FRET-enhanced optical microcavity. *Nature Communications* **13** (2022).

73. Liu, P. Y. *et al.* Cell refractive index for cell biology and disease diagnosis: past, present and future. *Lab on a Chip* **16,** 634–644 (2016).

74. Kane Yee. Numerical solution of initial boundary value problems involving maxwell's equations in isotropic media. *IEEE Transactions on Antennas and Propagation* **14,** 302–307 (1966).

75. Taflove, A., Hagness, S. C. & Piket-May, M. Computational electromagnetics: the finite-difference time-domain method. *The Electrical Engineering Handbook* **3,** 629–670 (2005).

76. Sullivan, D. M. *Electromagnetic simulation using the FDTD method* (John Wiley & Sons, 2013).

77. Berenger, J.-P. A perfectly matched layer for the absorption of electromagnetic waves. *Journal of Computational Physics* **114,** 185–200 (1994).

78. Gedney, S. D. & Zhao, B. An Auxiliary Differential Equation Formulation for the Complex-Frequency Shifted PML. *IEEE Transactions on Antennas and Propagation* **58,** 838–847 (2010).

79. Sinclair, M. B., Haaland, D. M., Timlin, J. A. & Jones, H. D. T. *Hyperspectral confocal microscope* tech. rep. ().

80. Lichtman, J. W. & Conchello, J.-A. Fluorescence microscopy. *Nature Methods* **2,** 910–919 (2005).

81. Pawley, J. *Handbook of biological confocal microscopy* (Springer Science & Business Media, 2006).

82. Huisken, J. & Stainier, D. Y. R. Selective plane illumination microscopy techniques in developmental biology. *Development* **136,** 1963–1975 (2009).

83. Minsky, M. Memoir on inventing the confocal scanning microscope. *Scanning* **10,** 128–138 (1988).

84. Kihm, K. D. in *Near-Field Characterization of Micro/Nano-Scaled Fluid Flows* 55–79 (Springer Berlin Heidelberg, Berlin, Heidelberg, 2011).

85. Denk, W., Strickler, J. H. & Webb, W. W. Two-photon laser scanning fluorescence microscopy. *Science* **248,** 73–76 (1990).

86. Göppert-Mayer, M. Über Elementarakte mit zwei Quantensprüngen. *Annalen der Physik* **401,** 273–294 (1931).

87. Kaiser, W. & Garrett, C. G. B. Two-Photon Excitation in CaF2:Eu2+. *Physical Review Letters* **7,** 229–231 (1961).

88. Xu, C. & Webb, W. W. Measurement of two-photon excitation cross sections of molecular fluorophores with data from 690 to 1050 nm. *Journal of the Optical Society of America B* **13,** 481 (1996).

89. Zipfel, W. R., Williams, R. M. & Webb, W. W. Nonlinear magic: multiphoton microscopy in the biosciences. *Nature Biotechnology* **21,** 1369–1377 (2003).

90. Squirrell, J. M., Wokosin, D. L., White, J. G. & Bavister, B. D. Long-term two-photon fluorescence imaging of mammalian embryos without compromising viability. *Nature Biotechnology* **17,** 763–767 (1999).

91. Lu, G. & Fei, B. Medical hyperspectral imaging: a review. *Journal of Biomedical Optics* **19,** 010901 (2014).

92. Schultz, R. A. *et al. Hyperspectral Imaging: A Novel Approach For Microscopic Analysis* tech. rep. (2001).

93. Gao, L. & Smith, R. T. Optical hyperspectral imaging in microscopy and spectroscopy - a review of data acquisition. *Journal of Biophotonics* **8,** 441–456 (2015).

94. Caixeiro, S., Wijesinghe, P., Dholakia, K. & Gather, M. C. Snapshot hyperspectral imaging of intracellular lasers. *Optics Express* **31,** 33175 (2023).

95. Jacques, S. L. Optical properties of biological tissues: a review. *Physics in Medicine \& Biology* **58,** R37 (2013).

96. Weissleder, R. A clearer vision for in vivo imaging. *Nature biotechnology* **19,** 316–317 (2001).

97. Smith, A. M., Mancini, M. C. & Nie, S. Second window for in vivo imaging. *Nature nanotechnology* **4,** 710–711 (2009).

98. Friebel, M., Helfmann, J., Netz, U. & Meinke, M. Influence of oxygen saturation on the optical scattering properties of human red blood cells in the spectral range 250 to 2000 nm. *Journal of Biomedical Optics* **14,** 034001 (2009).

99. Bashkatov, A. N., Genina, E. A., Kochubey, V. I. & Tuchin, V. V. Optical properties of human skin, subcutaneous and mucous tissues in the wavelength range from 400 to 2000 nm. *Journal of Physics D: Applied Physics* **38,** 2543–2555 (2005).

100. Bednarkiewicz, A., Chan, E. M., Kotulska, A., Marciniak, L. & Prorok, K. Photon avalanche in lanthanide doped nanoparticles for biomedical applications: super-resolution imaging. *Nanoscale Horizons* **4,** 881–889 (2019).

101. Chan, K. K. *et al.* Monitoring Amyloidogenesis with a 3D Deep-Learning-Guided Biolaser Imaging Array. *Nano Letters* **22,** 8949–8956 (2022).

102. Li, X. *et al.* Optical coherence tomography and fluorescence microscopy dual-modality imaging for in vivo single-cell tracking with nanowire lasers. *Biomedical Optics Express* **11,** 3659 (2020).

103. Dannenberg, P. H. *et al.* Laser particle activated cell sorting in microfluidics. *Lab on a Chip* **22,** 2343–2351 (2022).

104. Humar, M., Upadhya, A. & Yun, S. H. Spectral reading of optical resonance-encoded cells in microfluidics. *Lab on a Chip* **17,** 2777–2784 (2017).

105. Huang, J., Kim, S.-H. & Scherer, A. Design of a surface-emitting, subwavelength metal-clad disk laser in the visible spectrum. *Optics Express* **18,** 19581 (2010).

106. Usman, M., Munsif, M., Mushtaq, U., Anwar, A.-R. & Muhammad, N. Green gap in GaN-based light-emitting diodes: in perspective. *Critical Reviews in Solid State and Materials Sciences* **46,** 450–467 (2021).

107. Auf der Maur, M., Pecchia, A., Penazzi, G., Rodrigues, W. & Di Carlo, A. Efficiency Drop in Green InGaN/GaN Light Emitting Diodes: The Role of Random Alloy Fluctuations. *Physical Review Letters* **116,** 027401 (2016).

108. Adachi, S. in *Springer Handbooks* 1–1 (Springer, 2017).

109. Krysa, A. *written communication* 2019.

110. Xing, G. *et al.* Ultralow-Threshold Two-Photon Pumped Amplified Spontaneous Emission and Lasing from Seeded CdSe/CdS Nanorod Heterostructures. *ACS Nano* **6,** 10835–10844 (2012).

111. Zhang, C. *et al.* Low-threshold two-photon pumped ZnO nanowire lasers. *Optics express* **17,** 7893–7900 (2009).

112. Yan, D. *et al.* Stable and low-threshold whispering-gallery-mode lasing from modified CsPbBr3 perovskite quantum dots@ SiO2 sphere. *Chemical Engineering Journal* **401,** 126066 (2020).

113. König, K., Becker, T. W., Fischer, P., Riemann, I. & Halbhuber, K.-J. Pulse-length dependence of cellular response to intense near-infrared laser pulses in multiphoton microscopes. *Optics Letters* **24,** 113 (1999).

114. Li, B., Wu, C., Wang, M., Charan, K. & Xu, C. An adaptive excitation source for high-speed multiphoton microscopy. *Nature Methods* **17,** 163–166 (2020).

115. Weber, G. Resolution of the fluorescence lifetimes in a heterogeneous system by phase and modulation measurements. *The Journal of Physical Chemistry* **85,** 949–953 (1981).

116. Ranjit, S., Malacrida, L., Jameson, D. M. & Gratton, E. Fit-free analysis of fluorescence lifetime imaging data using the phasor approach. *Nature Protocols* **13,** 1979–2004 (2018).

117. Malacrida, L., Ranjit, S., Jameson, D. M. & Gratton, E. The Phasor Plot: A Universal Circle to Advance Fluorescence Lifetime Analysis and Interpretation. *Annual Review of Biophysics* **50,** 575–593 (2021).

118. Dutta, N., Hartman, R. & Tsang, W. Gain and carrier lifetime measurements in AlGaAs single quantum well lasers. *IEEE Journal of Quantum Electronics* **19,** 1243–1246 (1983).

119. Sokolovskii, G. S. *et al.* Turn-on delay of QD and QW laser diodes: What is the difference? *Journal of Physics: Conference Series* **461,** 012030 (2013).

120. Ratnaike, R. N. Acute and chronic arsenic toxicity. *Postgraduate Medical Journal* **79,** 391–396 (2003).

121. Caixeiro, S. *et al. Micro and nano lasers from III-V semiconductors for intracellular sensing* in (SPIE-Intl Soc Optical Eng, 2020), 36.

122. Ferrand, P. GPScan.VI: A general-purpose LabVIEW program for scanning imaging or any application requiring synchronous analog voltage generation and data acquisition. *Computer Physics Communications* **192,** 342–347 (2015).

123. Hunter, J. D. Matplotlib: A 2D Graphics Environment. *Computing in Science & Engineering* **9,** 90–95 (2007).

124. Sofroniew, N. *et al. napari: a multi-dimensional image viewer for python.* (DOI: 10.5281/zenodo.3555620, 2022).

125. Burns, K., Adams, K. B. & Longwell, J. Interference Measurements in the Spectra of Neon and Natural Mercury. *Journal of the Optical Society of America* **40,** 339 (1950).

126. Fish, D. A., Walker, J. G., Brinicombe, A. M. & Pike, E. R. Blind deconvolution by means of the Richardson–Lucy algorithm. *Journal of the Optical Society of America A* **12,** 58 (1995).

127. Richardson, W. H. Bayesian-Based Iterative Method of Image Restoration. *Journal of the Optical Society of America* **62,** 55 (1972).

128. Lucy, L. B. An iterative technique for the rectification of observed distributions. *The Astronomical Journal* **79,** 745 (1974).

129. Turek, I. Interference of modes in optical fibers. *Optical Engineering* **39,** 1304 (2000).

130. Caixeiro, S. *et al.* Local Sensing of Absolute Refractive Index During Protein-Binding using Microlasers with Spectral Encoding. *Advanced Optical Materials* **11** (2023).

131. Yeh, Y. L. Real-time measurement of glucose concentration and average refractive index using a laser interferometer. *Optics and Lasers in Engineering* **46,** 666–670 (2008).

132. Fujiwara, E., Cabral, T. D., Sato, M., Oku, H. & Cordeiro, C. M. B. Agarose-based structured optical fibre. *Scientific Reports* **10,** 7035 (2020).

133. Weng, L., Liang, S., Zhang, L., Zhang, X. & Xu, J. Transport of Glucose and Poly(ethylene glycol)s in Agarose Gels Studied by the Refractive Index Method. *Macromolecules* **38,** 5236–5242 (2005).

134. Datsyuk, V. V. Some characteristics of resonant electromagnetic modes in a dielectric sphere. *Applied Physics B Photophysics and Laser Chemistry* **54,** 184–187 (1992).

135. Liu, B., Zhu, F., Xia, X., Park, E. & Hu, Y. A tale of terminal differentiation: IKKα, the master keratinocyte regulator. *Cell Cycle* **8,** 527–531 (2009).

136. Bikle, D. D., Xie, Z. & Tu, C.-L. Calcium regulation of keratinocyte differentiation. *Expert Review of Endocrinology & Metabolism* **7,** 461–472 (2012).

137. Rübsam, M. *et al.* E-cadherin integrates mechanotransduction and EGFR signaling to control junctional tissue polarization and tight junction positioning. *Nature Communications* **8** (2017).

138. Bijsterbosch, J. & Volgenant, A. Solving the Rectangular assignment problem and applications. *Annals of Operations Research* **181,** 443–462 (2010).

139. Crouse, D. F. On implementing 2D rectangular assignment algorithms. *IEEE Transactions on Aerospace and Electronic Systems* **52,** 1679–1696 (2016).

140. Virtanen, P. *et al.* SciPy 1.0: fundamental algorithms for scientific computing in Python. *Nature Methods* **17,** 261–272 (2020).

141. Van Der Wel, C. & Kraft, D. J. Automated tracking of colloidal clusters with sub-pixel accuracy and precision. *Journal of Physics Condensed Matter* **29** (2017).

142. Allan, D. B., Caswell, T., Keim, N. C., van der Wel, C. M. & Verweij, R. W. *soft-matter/trackpy: Trackpy v0.5.0* (DOI: 10.5281/zenodo.3492186, 2021).

143. Crocker, J. C. & Grier, D. G. Methods of Digital Video Microscopy for Colloidal Studies. *Journal of Colloid and Interface Science* **179,** 298–310 (1996).

144. Gigan, S. Optical microscopy aims deep. *Nature Photonics* **11,** 14–16 (2017).

145. Horstmeyer, R., Ruan, H. & Yang, C. Guidestar-assisted wavefront-shaping methods for focusing light into biological tissue. *Nature Photonics* **9,** 563–571 (2015).

146. Wang, S. *et al.* High-Yield Plasmonic Nanolasers with Superior Stability for Sensing in Aqueous Solution. *ACS Photonics* **4,** 1355–1360 (2017).

147. Park, J., Baek, W., Geum, D.-M. & Kim, S. Understanding the Sidewall Passivation Effects in AlGaInP/GaInP Micro-LED. *Nanoscale Research Letters* **17,** 29 (2022).

148. Kwok, S. J. J. *et al.* High-dimensional multi-pass flow cytometry via spectrally encoded cellular barcoding. *Nature Biomedical Engineering* (2023).

149. Baba, T. & Sano, D. Low-threshold lasing and purcell effect in microdisk lasers at room temperature. *IEEE Journal of Selected Topics in Quantum Electronics* **9,** 1340–1346 (2003).

A Appendix

A.1 Methods

Nanodisk laser fabrication

Reproduced from [1].
The wafers were grown on GaAs substrates by metal–organic vapor-phase epitaxy (MOVPE) at the EPSRC National Epitaxy Facility in Sheffield, U.K. Substrates were cleaned by 3 min sonication in IPA, acetone, deionised water, and methanol, followed by 3 min of O_2 plasma. We then spin-coated a ∼380 nm thick layer of SU8 photoresist (SU8 2000.5, KayakuAM, 3:1 dilution with cyclopentanone), which was soft baked on a hot plate at 90°C for 2 min. A pattern of filled circles was exposed with UV lithography, using a mask with 3 µm diameter holes, followed by a 2 min post exposure bake at 90°C. The resist was developed in 2-methoxy-1-methylethyl acetate (EC solvent, Microposit) for 60 s and then cured at 180°C for 10 min. A 30 s descumming step with reactive ion etching in oxygen plasma was performed, followed by a 12 s wet etch in the Br_2/HBr solution. The SU8 caps were then removed by reactive ion etching in oxygen plasma for 7 min. The remaining disk structures rested on columns of the sacrificial layer, which were selectively etched away in 5% hydrofluoric acid for 3 min. During this step, the detached microlasers collapsed onto the GaAs substrate from where they were readily harvested into a Petri dish upon sonication in an aqueous environment, leaving free-floating microlasers in suspension.

Optical characterisation of nanolasers for wafer comparison measurements

Reproduced from [1].
Microlaser performance was characterised using one of two custom-built micro-PL setups constructed on inverted microscopes. For the threshold comparison with green and red excitation, 532 nm (Coherent Helios 532-4-125) and 642 nm (Omicron Quixx 642-140 PS) pump lasers were coupled into the microscope to form a diffraction limited excitation spot. The microlaser signal was collected using a 25× silicone immersion objective (Nikon CFI Plan Apochromat Lambda S 25XC Sil). On the second setup, pump lasers operating

at 473 nm (Alphalas Pulselas-P-473-10, used for cell experiments) and 1030 nm (Toptica Femtofibre Vario 1030) and a tuneable OPO (Opotek Opolette) were used for microlaser excitation. A back focal plane lens was added to form a collimated excitation beam ($d \approx 200\,\mu m$). In this second setup, either a 60× oil immersion objective (Nikon Plan Apo VC) or a 40× air objective (Nikon S Plan Fluor ELWD) was used. Both microscopes were connected to a spectrograph (Andor Shamrock 500i) equipped with an $1800\frac{1}{mm}$ grating and an EM-CCD camera (Andor Newton). The optical resolution of the spectrometer was approximately 0.04 nm.

Toxicity assay

Reproduced from [1].
Four dishes with HEK293 cells were cultured in medium (Dulbecco's modified Eagle's medium, fetal bovine serum, penicillin/streptomycin, glutamine) and incubated at 37°C. For microlaser samples, a piece of a wafer with fully underetched microlasers was sonicated in an Eppendorf tube in phosphate-buffered saline (PBS) to detach microlasers. The microlaser suspension was diluted with cell medium and added to the respective dish through a filter with a pore size of 5 µm. The dishes were then incubated for either 3 or 5 days, with medium replaced after the third day in the two dishes designated for the 5 day stability test. For the fluorescent imaging, cells were stained with green cell tracker dye (5-chlormethylfluorescein diacetate, Fisher Scientific Cat# C2925, 10 µM) for 30 min, with DAPI (4',6-diamidino-2-phenylindole, dilactate, Fisher Scientific Cat# 11530306, 25 µg/mL) for 5 min, and with propidium iodide (Calbiochem, Cat# 537059, 1.5 µM) for 5 min and then imaged immediately. Epifluorescence images for the live–dead assay were obtained on an inverted epifluorescence microscope (Nikon Eclipse Ti) using a 40× or 20× objective (Nikon S Plan Fluor ELWD). Cells were counted manually with the ImageJ cell tracker plugin, using the DAPI stain to count the total number of cells (day 3, $n > 1400$; day 5, $n > 3400$) and discriminating between live (cell tracker) and dead (propidium iodide) cells from the epifluorescence images.

Preparation of agarose sample with microlasers and well

A stock solution of 1% w/v agarose in DIW was heated in the microwave until liquid and then poured into a glass-bottom imaging dish with a circular placeholder in the middle of the dish (an inverted pipette tip was used as a placeholder). Immediately afterwards, a suspension of PS microbead lasers in DIW was pipetted as close to the placeholder as

possible, then the sample was placed into the fridge immediately to solidify the agarose. Finally, the placeholder was removed, leaving a circular well in the middle of the solid agarose-microlaser matrix.

FDTD simulations - Chapter redacted

Preparing keratinocyte cultures with nanodisk lasers

Cell cultures were kept under standard conditions[137] for the 3D epidermis model in an incubator set to 32 °C in the low-Ca^{2+} cell medium, performing regular media changes and re-seeding cells before reaching confluency. 24 h prior to seeding the cells, plastic bottom imaging dishes were filled with a collagen solution (30 µg/mL in PBS) and left in the fridge until seeding cells. Prior to the measurement, semiconductor nanolasers were added to the samples during the reseeding of cells. For this, the cells were detached and the concentration of cells in the suspension was counted with a hemocytometer to determine the volume required for re-seeding, aiming for 68.000 cells per well in a 4-well imaging dish with a volume of 300 µL per well. In parallel, semiconductor nanolasers were detached from the wafer into a microcentrifuge tube containing cell medium, and the nanolaser suspension was filtered through a 5 µm-pore size membrane filter to remove fragments of the wafer substrate from the suspension. Then, the calculated volume of the cell suspension was seeded into the collagen-coated 4-well imaging dish, and the nanolaser suspension was added. The sample was allowed 24 h for the cells to attach and uptake the nanolasers, then the cell medium was exchanged for the high-Ca^{2+} medium just before starting the hyperspectral imaging measurements.

Aquaculture - Chapter redacted

Sphyncs: Software for processing Hyperspectral Confocal Scans

This section is reproduced with minor modifications from 'Supplementary Note 3: Software Architecture' in the Supplementary Information of reference[2] and refers to the published software 'sphyncs'[3]. In the following sections, the word 'microlaser' is used to collectively describe micro- and nanolasers.

Our software processing workflows are predominantly written in Python. Here, we provide four Supplementary Code Files (as jupyter notebooks) and three python helper files

that contain all processing functions and are imported at the beginning of each Supplementary Code File. The four Supplementary Code Files serve as application examples to demonstrate processing functions and algorithms for a range of different applications. Supplementary Code 1 explains fundamental operations, including organising the multi-dimensional datasets into correctly formatted images, 3D-stacks, and sequences of images or stacks. It also explains how to extract and store individual spectra from specified positions in the image. In Supplementary Code 2, we discuss our treatment of multi-mode spectra, with an emphasis on refractive index sensing. This workflow includes high-throughput peak fitting to extract the external refractive index around each microlaser and its size from individual spectra. The results can be displayed as simple 2D traces, or as images with custom colour-coding in the open-source interactive viewer napari[124]. Supplementary Code 3 pre-processes hyperspectral images of single-mode microlasers to a data format compatible with the open-source ND particle tracking algorithm Trackpy[142]. Information of the automatically tracked microlasers is then organised into a custom data structure that allows displaying trajectories of microlasers, the evolution of their mode positions, and other quantities of interest. We also include Supplementary Code 4, where our workflows were adapted to data acquired in a different format (due to a different trigger configuration), which applies to the adaptation of our protocol for integration with commercial confocal microscopes. Each of the files provided in our repository is explained in more detail below and can be found at [3].

"utils.py"

The python helper file "utils.py" first imports the main scientific computing libraries used in our processing toolbox (numpy, matplotlib, scipy, imageio, napari, math). "utils.py" contains a few useful functions including mathematical expressions, spectral analysis, and elementary image data handling. These functions are automatically called as part of larger algorithms without needing further optimisation or adaptation. An exemption is the spectral calibration function 'formAxis', which must be updated after acquiring the calibration data (Section 4.1). 'formAxis' transforms pixel number p on the line-scan camera into wavelength λ, assuming a linear mapping (Equation 4.1). Refer to Table A.4 for the calibration values for all gratings. We have encoded a case structure in our calibration function, allowing to store multiple calibrations for different gratings. In addition to the case structure variable, the centre wavelength of the grating during the measurement λ_c also needs to be passed as input argument 'gratingCentre' to the function 'formAxis'. Note that the accuracy of this linear approximation might be limited for very extended wavelength ranges, therefore the calibration measurement should include peaks

in the same range of the microlaser emission, or as close as possible.

"acquisitionExtended.py"

This file is the acquisition class definition, i.e., a custom Python object specifically designed to represent hyperspectral confocal measurements. This data structure can store all relevant measurement settings as attributes (Table A.1), which can be automatically set by loading the measurement log file or be user-defined. The acquisition class contains all data processing methods (i.e., functions that are specific to the data class). The main advantage of this approach is that operations that require knowledge of important acquisition attributes, which includes almost all processing functions, can access them directly from the acquisition object, rather than requiring user input. These processing methods are used in the Supplementary Code Files and will be explained in detail later.

Attribute	Explanation
name	The name of the stored .tif files of the measurement, without the 'framexxxxx' extension.
directory	Path of the directory containing the raw data. This can be a folder on external drives, too, which can be preferable due to the large file sizes.
xDim, yDim	Number of spatial pixels in x, y. The height of an individual camera buffer will equal xDim × yDim.
zDim	Number of $z-$slices in the stack
tDim	Number of frames in a $x-y-(z-)t$ sequence. The total number of buffers acquired during the measurement will equal zDim × tDim.
xStep, yStep, zStep	The size of individual voxels (x, y, z), in µm.
tStep	The duration between each timestep.
xaxis	Array containing the calibrated wavelength-values corresponding to each camera pixel along its spectral axis.
wLDim	The width of individual camera buffers, equivalent to the number of data points on the spectral axis. This will be equal to the 2048 pixels of the line-scan camera, unless cropped to a smaller number.

Table A.1. Attributes of the Acquisition Data Class

Supplementary Code 1

Here, we first import "acquisitionExtended.py" along with its dependencies, including "utils.py" and the scientific computing libraries used (see jupyter notebook, Cell 1, line 1). We next define the directory and name of the data set and the corresponding log file (Cell 2, lines 1-3), before calling the constructor of the acquisition class (Cell 2, line 4). With the log file name as one argument and the size of the scan field at ± 50 V as

the second argument, the 'autoCalibrate' method can be used (Cell 3, line 2). It will retrieve all relevant settings from the log file, store them as attributes in the acquisition object, and use them to calculate the correct voxel size and spectral calibration. Where no log file is present, the acquisition attributes can be specified manually when calling the class constructor (Cell 4, line 3), which requires subsequent manual calculation of the voxel size (Cell 4, lines 5-6). To process an individual image, the 'construct2D' method is used (Cell 5, line 7). The timestep and $z-$position of the 2D image need to be specified, and there are a few additional optional arguments. With 'threshold', only pixels above a given threshold are included in the image formation; enabling 'save' automatically saves the processed images; s1 and s2 allow limiting the bandwidth of the colour-mapping in spectral images to a user-defined range (useful for avoiding mode jumps in colour-coding of multi-mode spectra); with show='True', the processed images will automatically be displayed; 'specImg=True' enabled spectral processing in addition to intensity-based images; and lastly, a custom scale value 'scaleVal' can be entered to limit the colour map of the intensity image to a certain range. The function returns an intensity-based image 'imap', and the spectral image 'maxmap' (if spectral processing was enabled). Individual spectra can be extracted with the 'getSingleSpectrum' or 'getSingleSpectrumIntegrated' method (Cell 6). A position (x, y, z, t) needs to be specified, and, if the resulting spectra should be exported as .txt files (save='True'), a file path for the saved spectra also needs to be passed to the function. 'getSingleSpectrum' retrieves the spectrum exclusively from the designated position, whereas 'getSingleSpectrumIntegrated' returns an average of all spectra within a certain tolerance (keyword argument 'tol', given as numbers of pixels) that are above a certain threshold (keyword argument 'thresh').

Stacks are processed with the 'construct3D' (intensity only) and 'constructSpec3D' (intensity and spectral information) methods (Cell 7, line 1). The keyword arguments of this method are analogous to its 2D equivalent. Before loading the images in napari (Cell 8, line 6), we typically define a viewing angle of the stack (Cell 8, line 2), the correct spatial scaling (Cell 8, line 3; directly taken from the acquisition object), and an appropriate intensity scaling. Stacks can also be colour-coded according to their spectral information, which requires creating separate RGBA colour channels from the image data (Cell 9, line 2) with the 'VAtoRGBA' function (inputs: the spectral image, the intensity image, and the lower and upper limit of the colour map). The resulting colour-arrays can then be loaded into napari as separate channels (Cell 9, lines 6-8). The 3D-rendered images can be exported as screenshots from napari, where a simple loop over a range of angles can be used to create a flyover video (Cell 10).

Supplementary Code 2

To begin, we set up the acquisition object (Cell 1, lines 1-16; as explained for Supplementary Code 1). Next, the 'fitSpectraToFiles' method is called for detecting all peaks in the data set and storing them in a data format suitable for applying the mathematical model. 'fitSpectratoFiles' will analyse all pixels above a certain intensity threshold (keyword argument 'thresh') and detect all peaks above a certain height (keyword argument 'height') in each spectrum, assuming a given spacing between adjacent peaks (keyword argument 'tol', in pixel number), using an inbuilt scipy function. All detected peaks are then fitted with a gaussian function, where the optimisation algorithm looks at a subset of the whole spectrum, which is a window of size 'tol2' (in pixel numbers) around the peak. A minimum number of peaks ('noPeaks') needs to be found such that spectra are included in the result files. The result files contain separate columns for each spectrum, where the position in the image is stored, as well as the intensity of the spectrum and the fitted peak positions. Such data files can be analysed using the 'AsymptoticExpansion' MATLAB script, which will be explained in more detail later. The script appends the fitted external refractive index (in RIU), microlaser size (in µm), and residual error of the fit (in m) to the end of each result file. These values can again be read into python for further processing and displaying with the 'ResultsFromFiles' method. Either the refractive index (param='n'; Cell 3, line 2), the microlaser size (param='d'; Cell 3, line 3), or two consecutive lasing peaks (param='peak'; Cell 3, line 4) can be read from the files, and for either option, a critical residual error ('maxRes') needs to be specified to exclude poor fits (typically, we use a number similar to the spectral resolution of the measurement, i.e. 4×10-11 m). If microlasers remain stationary during the measurement, their positions can be used to extract traces of the quantities of interest and plot them (Cell 4). The results can also be displayed as 3D-rendered projections in napari, using the 'cmapResultsFromFiles' method. In addition to the parameter of interest, and the critical residual error, upper and lower bounds of the colour mapping need to be included. The refractive index calibration data can be processed following the same routine (Cell 7), to determine the size distribution of the microlasers and their internal refractive index (Cell 8).

Asymptotic Expansion (MATLAB)

This optimisation workflow compares the measured peaks to a theoretical model for the resonance positions of whispering gallery modes based on the asymptotic expansion of resonance frequencies in Mie scattering[65]. Our optimisation assumes that we only observe the fundamental radial mode number l, therefore the measured mode position λ

depends on microlaser size d, refractive indices of the microlaser (nint) and of its environment (next), the angular mode number m, and the polarisation mode number p. For each spectrum containing a pre-defined minimum number of lasing peaks ('noPeaks' in Supplementary Code 2), the optimisation seeks to find a solution for the microlaser size, the external refractive index, and the angular mode numbers of consecutive modes. A range of each of these three parameters therefore needs to be defined prior to using the optimisation function ('fit_peaks.m'). The internal refractive index is assumed to be constant, where we either use the literature value, or find a more accurate number as part of our refractive index calibration workflow (see below). Using 'te_or_tm.m', the algorithm first automatically finds the polarisation mode numbers. Next, the number of initial guesses is specified (we typically use 100) to begin the optimisation. The 'spectral_peaks.m' function is called to calculate a set of mode positions based on the asymptotic expansion model ('wgm_schiller.m'), and the objective of the optimisation is to minimise the least square error between the calculated and experimental mode positions. Finally, the optimised values for microlaser size, the external refractive index, and the angular mode numbers are found, and a residual error for each fit is determined. These values are stored in the result files as described above.

To improve the accuracy of this approach, we typically run a calibration measurement that optimises the internal refractive index for a known external refractive index, using 'Cali_internalref.m' and 'fit_peaks_internalref.m'. Here, we use the calibration data set of microlasers in a medium of homogenous and well-known refractive index (like deionised water). The optimisation works analogous like the one described for finding the external refractive index, using the same functions ('wgm_schiller.m', 'te_or_tm.m', and 'spectral_peaks.m'). After the optimisation, users can filter the results for a critical residual error. From these, the script calculates the average internal refractive index, which can be used as an input parameter for the internal refractive index when using 'fit_peaks.m' and returns a .txt summary file with the filtered results.

Supplementary Code 3

Here, we first create and calibrate the acquisition object, allowing batch-processing the image files into a data format compatible with the ND-tracking algorithm Trackpy (Cell 1). The 'batchProcessND' method is called after deciding whether binning should be applied to reduce the file size ('nBin' keyword argument) and defining a range of intensity values to use during the tracking ('upLim' and 'lowLim'; Cell 1, line 14). In this step, the wavelength-axis is removed from the individual buffers and treated analogous to the $z-$axis (i.e., encoded in separate images). All images are stored in a .zip file (Cell 2) that

can be read into the 'Trackpy' algorithm using the 'pims.ImageSequenceND' function (Cell 3, line 1). Next, 'tp.batch' detects features in the whole data set, expecting features to have a size (in pixels) equal to the input argument 'diameter' (Cell 3, line 6). After calibrating the sequence, using the step sizes from the Scan object (Cell 4, lines 1-6), detected objects can be linked with the 'tp.link_df' function, and the results are stored as a .csv file. To organise the tracking results into a library of microlasers, we make use of two additional data structures: the 'disk' class for individual microlasers, and the 'trackDataND' class for data from the entire measurement. The results from the tracking algorithm are loaded into the database by calling the class constructor, passing the acquisition class an input argument for correct calibration of all dimensions (Cell 5, line 2). The data base contains all tracked microlasers in a library of 'disk' objects, and it can display trajectories of all microlasers in a common image, either colour-coded by wavelength (Cell 6, line 2) or by time (Cell 6, line 3), after defining a minimum length to exclude very short trajectories. One can also investigate individual microlasers (Cell 7) by first extracting them from the database, and then using their inbuilt methods 'plotTraj' to plot the evolution of any quantity of interest (to be specified as keyword argument 'ax0') over the duration of the measurement, or to plot individual $x-y$-migration paths with the 'plotXY' method (analogous to that of the whole database, but for one microlaser only).

Supplementary Code 4

This code file applies to data acquired with the 'Frame Trigger' configuration, which we recommend for integrating hyperspectral measurements with commercial confocal microscopes. The different triggering configuration leads to a different data format, which requires adaptations when processing the data. Specifically, individual buffers contain only one spatial dimension (x) here, in addition to the spectral information, and the additional axes (y-z/t) are all encoded as separate buffers. We have implemented additional 'CCF' (commercial confocal microscope) versions of some basic processing methods, which account for this difference, but take the same input and return the same results as the 'regular' processing methods. The data sets acquired with a commercial microscope can be processed with the same acquisition data class, but the 'autoCalibrateCCF' method is used for calibrating the scan from the log file (Cell 2), and the 'constructSpec2DCCF' method can construct intensity- and spectral images (Cell 3), which can be colour-coded and displayed in napari (Cell 4). Individual spectra from the data set can also be extracted from defined positions using the 'getSingleSpectrumCCF' method (Cell 5). Lastly, batch peak fitting was also implemented for the commercial confocal microscope case with

'fitSpectraToFilesCCF' (Cell 6). The resulting data format from this fit is identical to the version for the home-built microscope, ensuring compatibility with further data processing workflows.

A.2 Extended Data

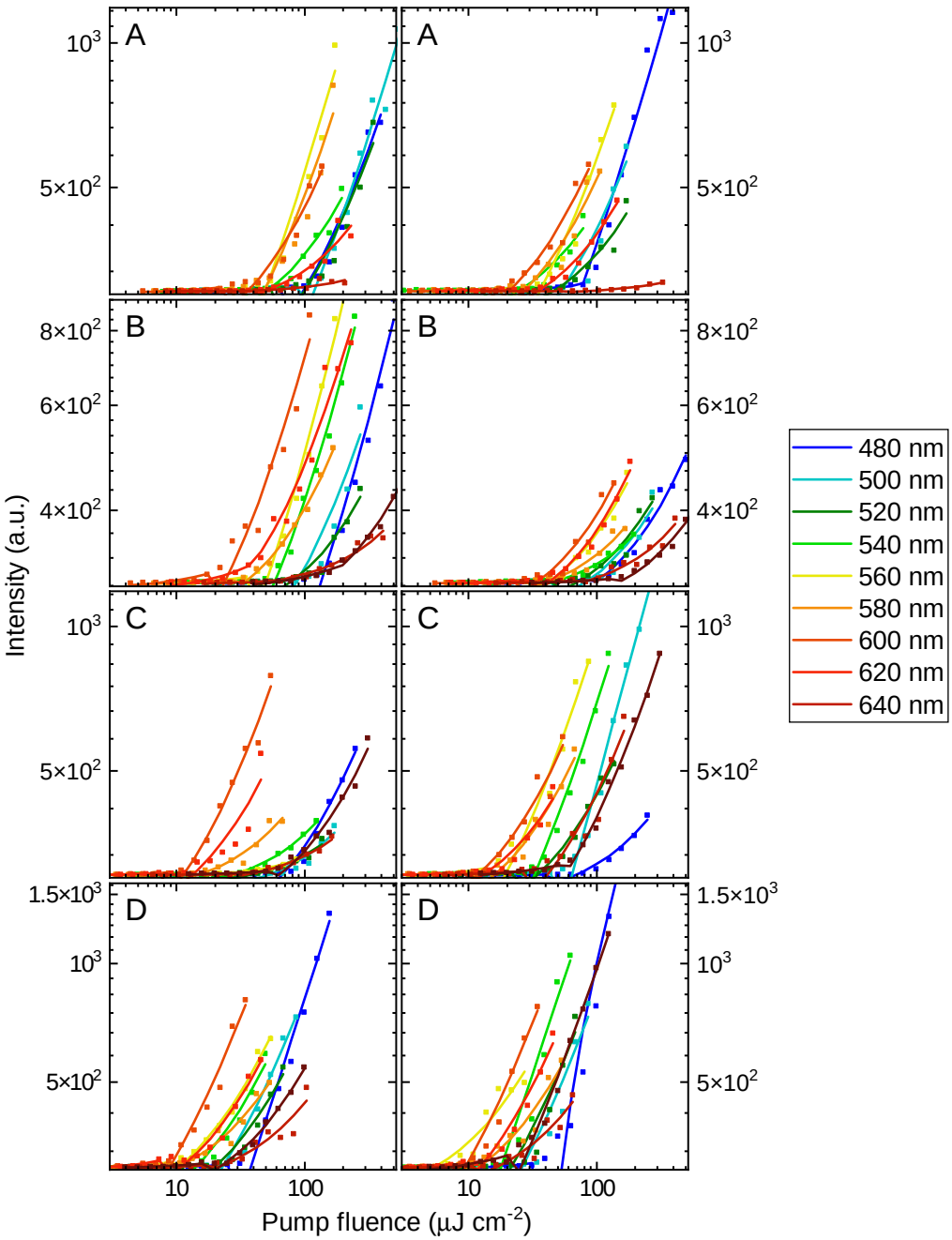

Fig. A.1. Wavelength-dependent lasing thresholds for each wafer composition used for calculations in Figure 3.4. Shown are the input-output curves for two nanolasers from each wafer, colour-coded for 10 different pump wavelengths from 480 nm (blue) to 660 nm (maroon). A double linear fit (solid lines in corresponding colours) was applied to each curve to calculate the lasing threshold. This method was applied because the microlasers were not excited far enough above threshold to allow reliable fitting with the rate equation model. Reproduced from [1].

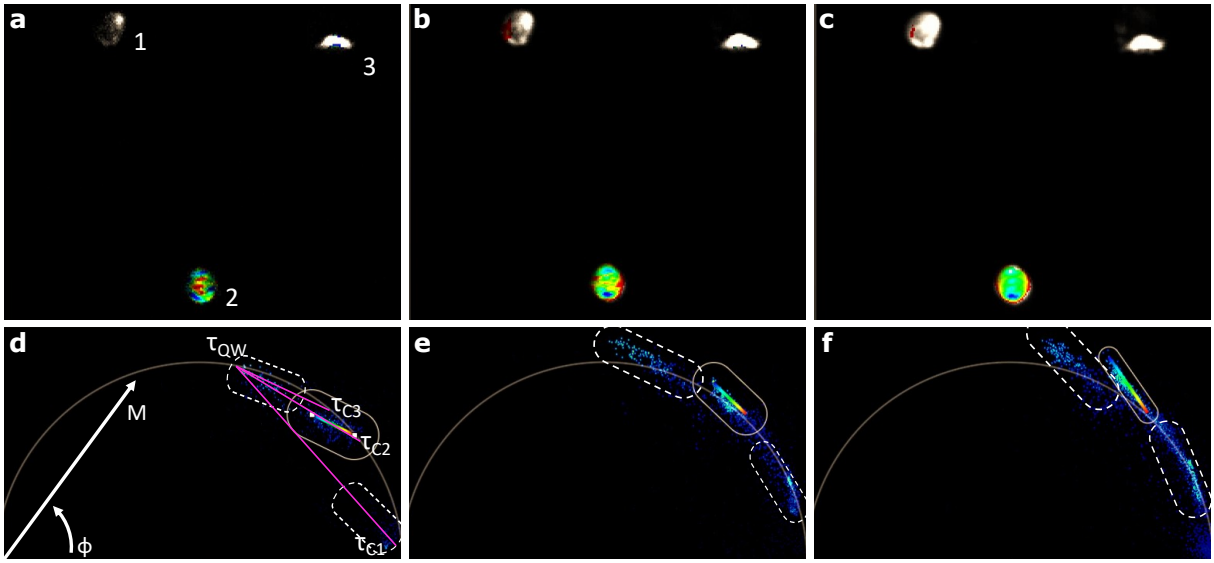

Fig. A.2. Fluorescent lifetime analysis of lasing process. Fluorescent data from 3.7 with excitation energies of 0.2% (a,d), 0.5% (b,e), and 1% (c,f). Here, all the nanolasers are shown in panels a-c. Additionally, the interpretation of the phasor plot for the sub-threshold sample (d) is superimposed. The lifetime populations of each device follow a bi-exponential decay with contributions from the excited state lifetime in the QW (τ_{QW}) and the cavity lifetime (τ_C). Bi-exponential decay in the phasor plot is characterised by lifetimes laying on a straight line connecting the two positions on the unit circle corresponding to the individual lifetimes (magenta lines). The cavity lifetime measured here is different for each nanolaser, but all lifetimes were shorter than τ_{QW}, which can be explained by Purcell shortening[149].

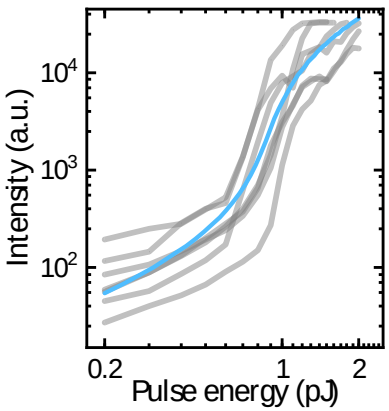

Fig. A.3. Lasing thresholds of semiconductor nanolasers in DIW, showing an average lasing threshold of 0.90 ± 0.12 pJ.

Label	Part	Part number mount	Part number optics
FC1	Corner mirror for excitation	DFM1B	DFM1-M-P01
FC2	Beamsplitter, brightfield	DFM1B, DFM1T3	BSX10R
FC3	Dichroic mirror	DFM1B, DFM1T3	DMLP567R
L1	Scan lens	SM2A33	LSM03-VIS
L2	Confocal tube lens	LCP08-M	TTL200-A
L3	Brightfield tube lens	CP36-M	AC254-075-A-ML
L4	Fibre coupling lens	SM1Z, SM1A6	AC127-019-A-ML
L5	Lens 1, spectrometer relay	CP36-M	AC254-040-A-ML
L6	Lens 2, spectrometer relay	SM1Z	AC254-050-A-ML
LP1	Longpass filter, brightfield	CP36-M	FELH550
LP2	Longpass filter, confocal	CP36-M	FELH550
FIB	optical fibre	ST1XY-D-M, SM1SMA (confocal side); CXY1A, SM1SMA (spectrometer side)	M96L02 (‘open pinhole’ fibre) or M65L02 (‘closed pinhole’ fibre)
GM	Galvo mirrors	GCM102/M	GVSM002EC/M
CAM1	Brightfield camera	-	DCC1545M
KM1-7	Kinematic mirror	KCB1C	BB111-E02
STAGE	Motorised stage	-	MP100-MLSH
LED	Brightfield illumination LED driver Aspheric condensor lens	CP36-M - SM1L10	M730L5 LEDD1B ACL2520U-A)
FW	Filter wheels	FW1A (x2)	NDK01
L7	Collimation lens	SM1M10, custom adapter	AC254-100-A
L8	Coupling lens	SM1Z	
SP	Short-pass filter	SM1L03	FESH0750
FIB	fibre mount comm.	ST1XY-S/M, SM1SMA	-

Table A.2. Part list for the custom-built CHSI setup and for the Leica commercial extension, Thorlabs parts.

Part	Manufacturer	Part number
Piezoelectric objective scanner	Physik Instrumente	ND72Z2LAQ
Threading adapter	Physik Instrumente	P-721.11Q, 1
DAQ	National Instruments	PCIe-6323
BNC breakout cable	National Instruments	BNC-2110
Line-scan camera	Teledyne e2v	EV71YO1CCL2210 - BB3
Line-scan trigger cable terminal	Teledyne e2v	OR-YXCC-27BE2M1
Frame grabber	Teledyne DALSA	Xtium-CL MX4
CCD camera	Andor	Newton DU940P-BV
Spectrometer, two outputs	Andor	SR500
532-nm excitation laser	Coherent	Helios 532-4-125
642-nm excitation laser	Omicron	Quixx 642-140 PS
1030-nm excitation laser	NKT Photonics	Origami XP
4× Plan apochromat	Nikon	MRD70040
10× Plan apochromat	Nikon	MRD70170
25×C Sil CFI Plan apochromat	Nikon	MRD73250

Table A.3. List of additional parts for the custom-built CHSI setup.

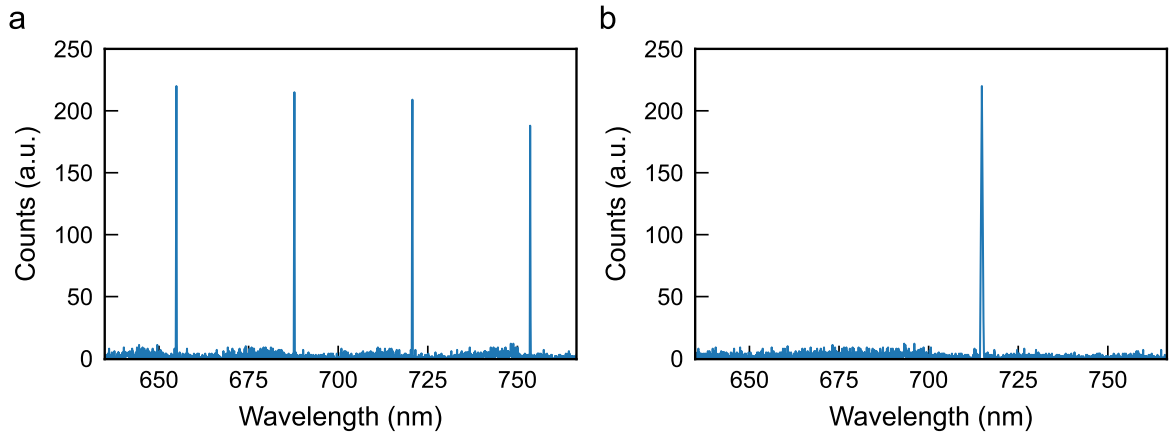

Fig. A.4. Structure of the spectra. a, Raw single-mode lasing spectrum, showing an interleaving of the 4 communication channels of the line-scan camera. The first channel contains every 4^{th} pixel, starting with the first pixel, the second channel every 4^{th} pixel starting with the second pixel, etc. **b,** Correct spectrum, recovered using the function 'utils.reshape' from [3].

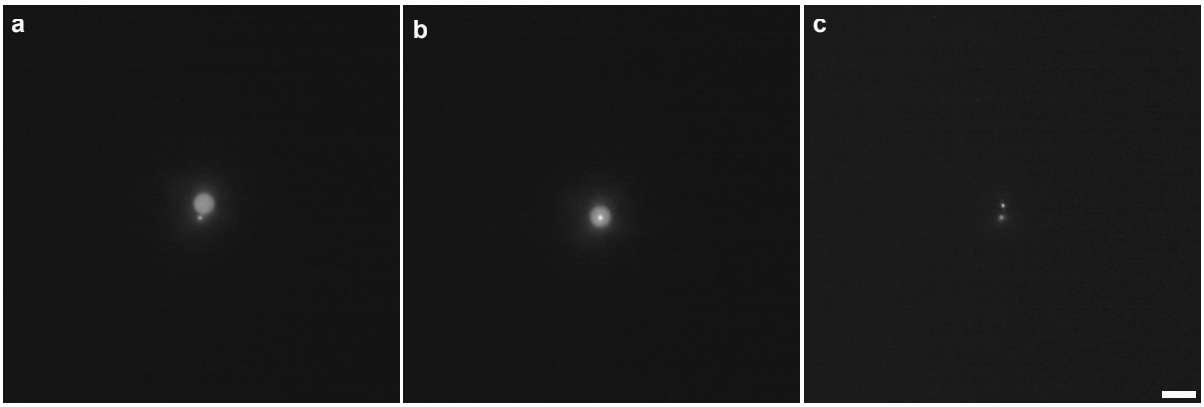

Fig. A.5. Alignment of the pinhole fibres. a, Misaligned 'open pinhole' fibre, showing the excitation beam (smaller spot) and the visualisation of the collection (large spot). **b,** Correctly aligned 'open pinhole' fibre, as seen by the two spots being concentric. **c,** Misaligned 'closed pinhole' fibre. The spot sizes of excitation and collection are now comparable.

Grating	λ_0(nm)	peak 1	peak 2	peak 3	a ($10^{-2}\frac{\text{nm}}{\text{p}}$)	b (nm)
300 $\frac{\text{l}}{\text{mm}}$	600	$p = 1857$	$p = 1377$	$p = 1344$	-6.430	665.50
		$\lambda = 546.07$nm	$\lambda = 576.96$nm	$\lambda = 579.07$nm		
1200 $\frac{\text{l}}{\text{mm}}$	700	$p = 525$	$p = 1285$	$p = 1716$	-1.344	713.79
		$\lambda = 706.72$nm	$\lambda = 696.54$nm	$\lambda = 690.7$nm		

Table A.4. Measured peaks and fit parameters for the spectral calibration. The grating was set to λ_0 during the measurement, and the fit returned slope a and intercept b of the linear calibration function.

Objective	Voltage (V)	FOV size (mm)	Mag (V/mm)
4×	±5	4.28266	2.3350
10×	±5	1.73385	5.7675
25×	±5	0.661116	15.125

Table A.5. Spatial calibration values for three objectives regularly used in this work.

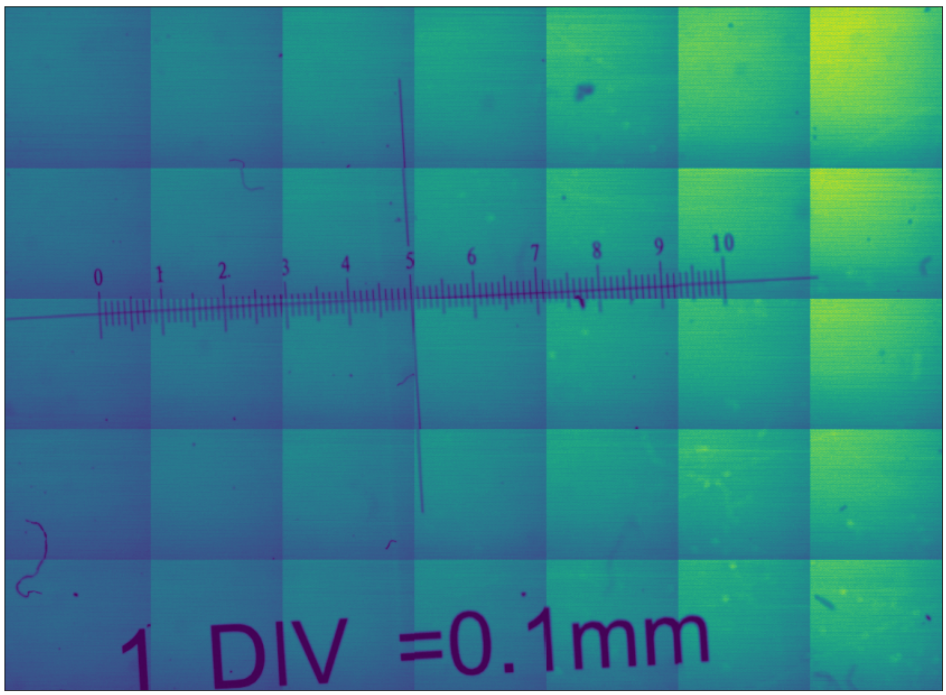

Fig. A.6. Image of the calibration slide, using a 4× objective and automated FOV stitching with the motorised stage.

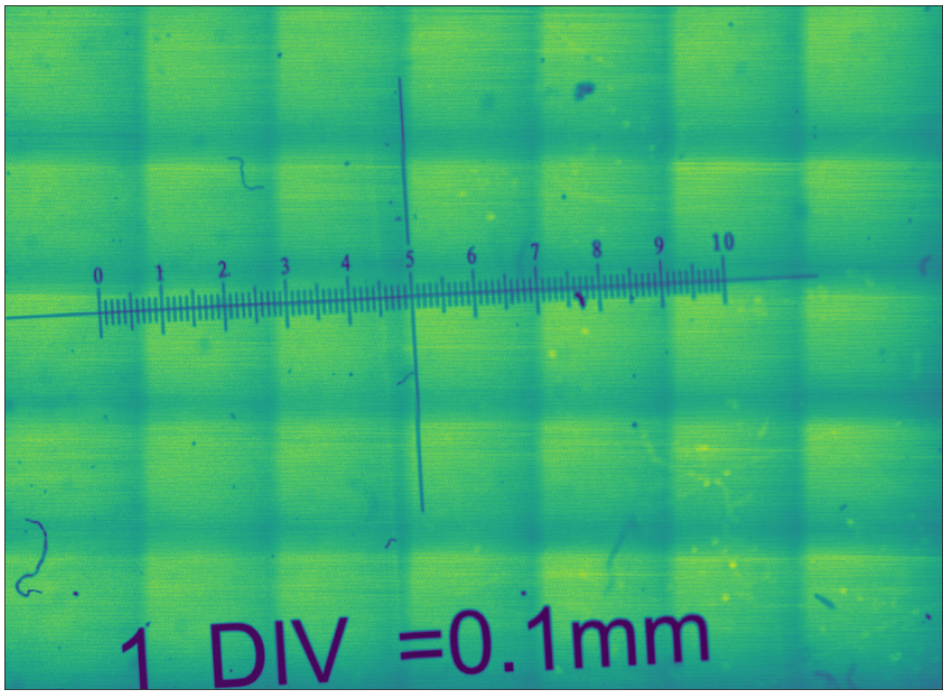

Fig. A.7. Stitched image from Figure A.6, post-processed to remove the intensity gradient and to smooth edges between adjacent tiles.

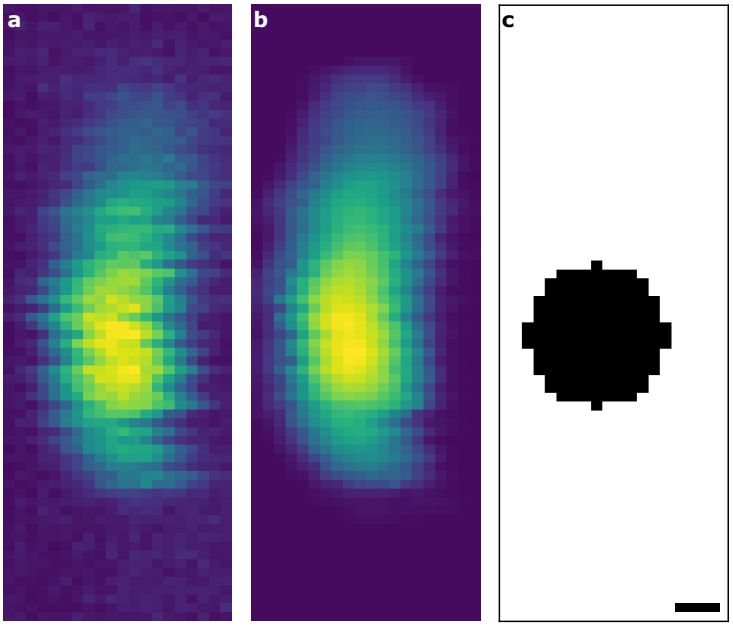

Fig. A.8. Spatial Resolution Data used for the deconvolution. **a,** Measured $x-z$ cross-section from a central position in the confocal stack of the 1.61 µm-diameter bead, **b,** Smoothed image from **a**, which was used for the deconvolution. **c,** Ground-truth assumption of the object. Scale bar, 500 nm.

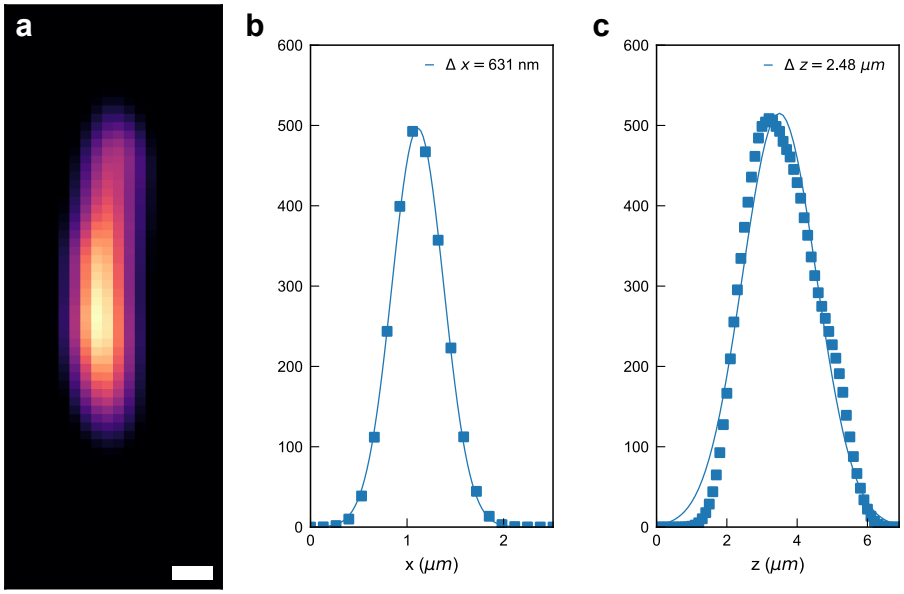

Fig. A.9. Results from the PSF deconvolution. **a,** PSF obtained from the deconvolution. **b,** Profile through the centre of the PSF in the lateral direction (symbols), showing a FWHM of 631 nm from a Gaussian fit (line). **c,** Axial profile of the PSF (symbols) with a Gaussian fit (line) with FWHM of 2.48 µm.

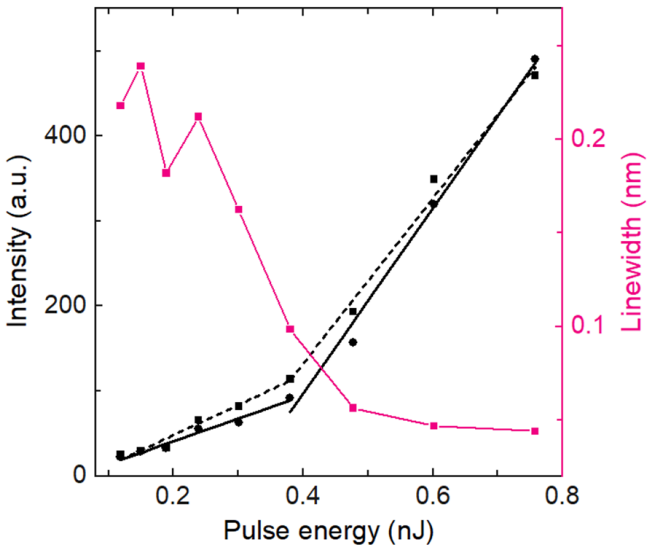

Fig. A.10. Lasing threshold of FluoRed PS microbead laser, showing the characteristic linewidth narrowing (magenta) and a lasing threshold (black symbols), where a lasing threshold value of 0.4 nJ was obtained by fitting high- and low-energy values with a double linear fit (black line). The circles and the solid line were obtained by measuring the output at energies in increasing order, while squares and the dashed line correspond to data with decreasing pulse energies.

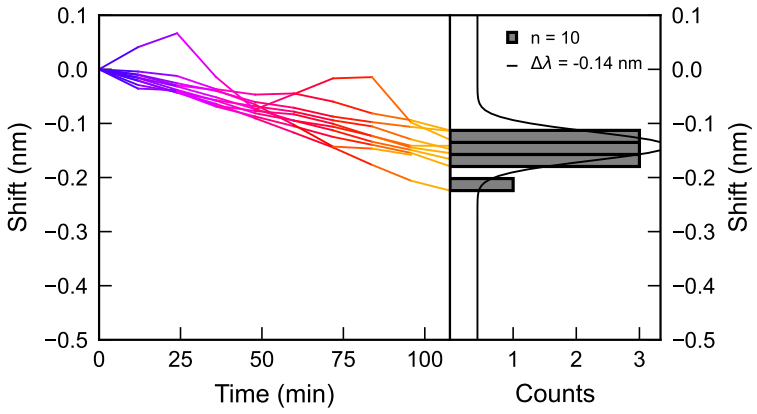

Fig. A.11. Nanolaser stability measurement at an excitation pulse energy of 2.5 pJ and a pulse repetition rate of 0.5 MHz. Left: Shift in peak emission wavelength over time. Negative values refer to a blue-shift. Right: Histogram of shift at the end of the experiment for all $n = 10$ lasers investigated (bars) and Gaussian fit to the data (line), indicating a mean blue-shift of 0.14 nm.

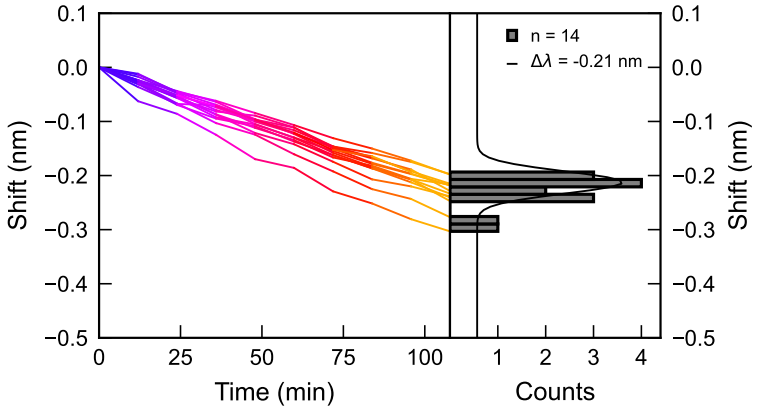

Fig. A.12. Nanolaser stability measurement at an excitation pulse energy of 5 pJ and a pulse repetition rate of 0.5 MHz. Shown are the measured shifts over time (left), and a histogram for $n = 14$ lasers with an average total blue-shift of 0.21 nm (right).

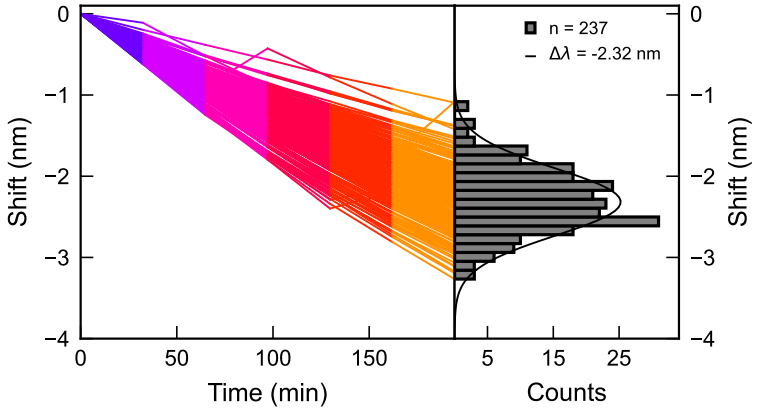

Fig. A.13. Nanolaser stability measurement at an excitation pulse energy of 9.9 pJ and a pulse repetition rate of 1 MHz. Right: measured shifts over time ($n = 237$), with statistics on the total shifts shown again on the left with an average blue-shift of 2.32 nm.

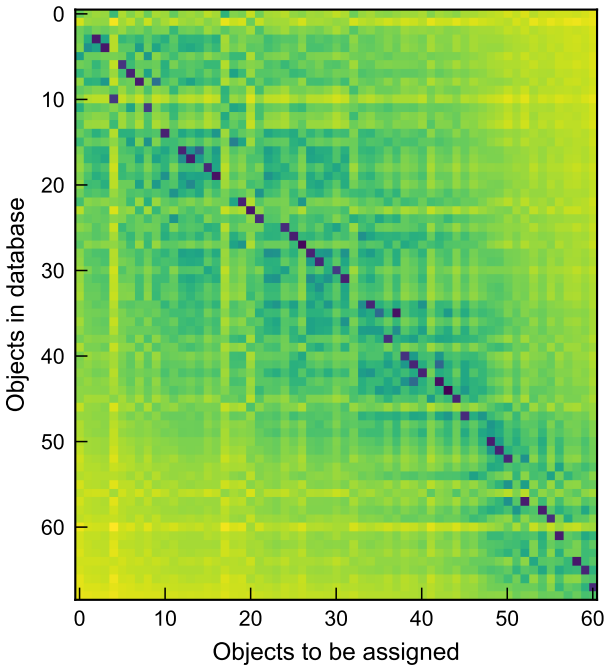

Fig. A.14. Cost table for the tracking algorithm, here used for data from the nanolaser stability measurements. Dark blue values are associated with low cost. A rectangular table, i.e. more objects in the data base than in the current frame, vice versa, is permitted for the case where objects move in and out of the FOV.